

2011-01-04

Slow Slip Beneath the Nicoya Peninsula, Costa Rica and Its Effect on the Interseismic Cycle

Kimberly C. Outerbridge

University of Miami, kouterbridge@rsmas.miami.edu

Follow this and additional works at: https://scholarlyrepository.miami.edu/oa_dissertations

Recommended Citation

Outerbridge, Kimberly C., "Slow Slip Beneath the Nicoya Peninsula, Costa Rica and Its Effect on the Interseismic Cycle" (2011). *Open Access Dissertations*. 511.

https://scholarlyrepository.miami.edu/oa_dissertations/511

This Open access is brought to you for free and open access by the Electronic Theses and Dissertations at Scholarly Repository. It has been accepted for inclusion in Open Access Dissertations by an authorized administrator of Scholarly Repository. For more information, please contact repository.library@miami.edu.

UNIVERSITY OF MIAMI

SLOW SLIP BENEATH THE NICOYA PENINSULA, COSTA RICA AND ITS
EFFECT ON THE INTERSEISMIC CYCLE

By

Kimberly C. Outerbridge

A DISSERTATION

Submitted to the Faculty
of the University of Miami
in partial fulfillment of the requirements for
the degree of Doctor of Philosophy

Coral Gables, Florida

December 2010

©2010
Kimberly C. Outerbridge
All Rights Reserved

UNIVERSITY OF MIAMI

A dissertation submitted in partial fulfillment of
the requirements for the degree of
Doctor of Philosophy

SLOW SLIP BENEATH THE NICOYA PENINSULA, COSTA RICA AND ITS
EFFECT ON THE INTERSEISMIC CYCLE

Kimberly C. Outerbridge

Approved:

Timothy H. Dixon, Ph.D.
Professor of Geology and Geophysics

Terri A. Scandura, Ph.D.
Dean of the Graduate School

Christopher C.G. Harrison, Ph.D.
Professor of Geology and Geophysics

Shimon Wdowinski, Ph.D.
Professor of Geology and Geophysics

Peter C. LaFemina, Ph.D.
Professor of Geology
Pennsylvania State University

OUTERBRIDGE, KIMBERLY C. (Ph.D., Marine Geology and Geophysics)
Slow Slip Beneath the Nicoya Peninsula, Costa Rica (December 2010)
and Its Effect on the Interseismic Cycle

Abstract of a dissertation at the University of Miami.

Dissertation supervised by Professor Timothy H. Dixon.
No. of pages in text. (162)

The close proximity of the Nicoya Peninsula to the Cocos-Caribbean Subduction zone plate boundary makes it a prime location to use GPS to study episodic tremor and slip. Nicoya Peninsula currently has operating networks of both continuous GPS (CGPS) and seismic stations designed to identify and characterize the pattern of episodic tremor and slip (ETS) events along the seismogenic zone under Costa Rica's Pacific Margin. The occurrence of slow slip events has been previously postulated in this region based on correlated fluid flow and seismic tremor events recorded near the margin wedge in 2000 and from sparse GPS observations in 2003. Paucity of data prevented details of these events from being resolved. In May 2007 a slow slip event was recorded on our densified GPS network. This slow slip event was also accompanied by seismic tremor, worked up by colleagues at the University of California – San Diego. I will present the GPS time series, correlated with the seismic tremor for the event in May 2007. I will also present the inferred pattern of slip on the plate interface from elastic half space inversion modeling compared with the tremor and Low Frequency Earthquake (LFE) locations. The geodetic slip and seismic tremor co-locate temporally very well. Spatially the

seismic tremor and LFE locations are offset but not independent of both the up dip and down dip patches of geodetic slip.

The identification of these slow slip events enhances our understanding of the nuances of the interseismic period. Previous studies of the interseismic strain accumulation patterns in the region of the Nicoya Peninsula have not accounted for the occurrence of slow slip, thus underestimating the magnitude of locking on the fault plane. My study resolves this bias by using our CGPS network to estimate the interseismic surface velocity field, accounting for the May 2007 slow slip event. I will present the results of this velocity field estimation and the results of inversions for locking patterns on the fault plane. My study has also elucidated a potential temporal variability in the locking pattern on the fault plane beneath Nicoya.

This dissertation is dedicated to my mother

ACKNOWLEDGEMENTS

There are so many people without whom this dissertation would not have been possible. First and foremost I thank my family for their unyielding love and support, mentally, emotionally and financially. My mom Sandy, my grandfather Duane and my stepfather Jack have all been integral to my success and the person that I have become. My fiancé Bryan and my dogs Niki and Eva have certainly helped me maintain my sanity.

I would also like to thank my committee, Tim Dixon, Chris Harrison, Shimon Wdowinski and Pete LaFemina. Both Tim and Jackie Dixon have been wonderful role models and have been like family to me during my eight-plus years in Miami. Chris and Shimon have always challenged me to be a better scientist, and for that I am grateful. Pete LaFemina has helped show me the way as a T.A., lab mate, committee member and member of the geodetic community. His advice and guidance have been invaluable.

Thank you to my past lab mates, Gina Schmalzle and Juliet Biggs for showing me the ways of the world. I would also like to thank Batu Osmonoglu, Scott Baker and Yan Jiang for their technical support of both me, and the Geodesy Lab as a whole, despite having their own projects to complete.

This project would not have been possible without the field support of Marino Protti and Victor Gonzalez. I will miss them dearly. Jake Walter, Susan Schwartz from UCSD and all of the UNAVCO engineers on this project have made my field experiences completely unforgettable.

Lastly, my MGG family, Emily Bowlin, Kelly Jackson, Lyanne Yurco, Kelly Gibson, Brooke Gintert, Melany McFadden, Maaike Petrie, have always been there for

me no matter what. I can only hope that I have been half the friend to them that they have been to me. You will all be missed and I hope that we can all be together again someday.

Since I also completed my undergraduate degree in the Geology Department at the University of Miami, I would like to thank all of the Geology faculty for providing me with a challenging, interesting and comprehensive education that has prepared me for a career in geoscience. I would particularly like to thank Hal Wanless for opening my eyes to Geology and the future it could hold for me during my completion of the UM Summer Scholars Program when I was a senior in high school. His continued support of my education and my science has meant so much to me over the years.

TABLE OF CONTENTS

	Page
LIST OF FIGURES	ix
LIST OF TABLES	xiii
 Chapter	
1 Introduction	1
1.1 Geologic Background	1
1.2 Episodic Tremor and Slip	2
1.3 Costa Rica: Regional Tectonics	4
1.3.1 Nicoya Peninsula, Costa Rica	9
1.3.2 Nicoya Peninsula Rupture History and Coupling	11
1.3.3 Interseismic Coupling	13
1.3.4 Thesis Development	14
 2 Methodology: The Global Positioning System (GPS) and Tectonic Modeling	 16
2.1 The Global Positioning System	16
2.1.1 The Space Segment	17
2.1.2 The Control Segment	20
2.1.3 The User Segment	20
2.1.4 Sources of Uncertainty	24
2.1.4.1 Clock Uncertainties	25
2.1.4.2 Ephemeris and Orbit Uncertainties	26
2.1.4.3 Propagation Delays: Ionosphere, Troposphere, and Stratosphere	27
2.1.4.3.1 The Ionosphere	28
2.1.4.3.2 Neutral Atmosphere	30
2.1.4.4 Multipath Uncertainties	32
2.1.4.5 User Errors	33
2.1.5 Field Methods	33
2.1.5.1 Network Geometry	34
2.1.5.2 Continuous GPS Sites	34
2.1.5.3 Campaign GPS Sites	36
2.1.6 GPS Data Processing	37
2.1.6.1 Preprocessing GPS Data	38
2.1.6.2 Processing With GIPSY-OASIS 2.2	39
2.1.6.3 Ambiguity Resolution	40
2.1.6.4 Network Baseline Calculation	41
2.1.6.5 Post-processing of GPS Data	42
2.2 Modeling.....	43
2.2.1 Inverse Theory	43

2.2.2 <i>Dislocation Modeling</i>	45
2.2.2.1 <i>Slipinv</i>	46
2.2.2.2 <i>Back Slip Modeling</i>	49
2.2.2.3 <i>Block Modeling: DEFNODE</i>	50
3 A Tremor and Slip Event on the Cocos-Caribbean Subduction zone as measured by a GPS and Seismic Network on the Nicoya Peninsula, Costa Rica	55
3.1 <i>Overview</i>	55
3.2 <i>Geologic Background</i>	59
3.3 <i>GPS and Seismic Network</i>	60
3.4 <i>Data and Analysis</i>	62
3.4.1 <i>GPS Analysis</i>	62
3.4.2 <i>Slow Slip Event Analysis</i>	62
3.4.3 <i>Seismic Tremor</i>	69
3.5 <i>Inversion Results</i>	74
3.6 <i>Discussion</i>	81
3.6.1 <i>Previous Observations of Slow Slip Events</i>	81
3.6.2 <i>2007 Event Slow Slip Distribution</i>	83
3.6.3 <i>Correlation of Slow Slip and Tremor</i>	86
3.6.4 <i>Strain Accumulation and Seismic Hazard</i>	88
3.7 <i>Conclusions</i>	91
4 Improved Interseismic Velocity Field and Locking Pattern Studies for the Nicoya Peninsula, Costa Rica	94
4.1 <i>Overview</i>	94
4.2 <i>Geologic Background</i>	96
4.3 <i>Previous Work on Temporal and Spatial Variability</i>	99
4.4 <i>Improved Surface Velocity Fields</i>	103
4.4.1 <i>IGS Straight Line Interseismic Estimation</i>	103
4.4.2 <i>Baseline Straight Line Interseismic Estimation</i>	106
4.4.3 <i>Baseline Hyperbolic Tangent Interseismic Estimation</i>	108
4.5 <i>Locking Pattern Results</i>	111
4.6 <i>Discussion</i>	114
4.6.1 <i>Comparison to Other Interseismic Locking Studies</i>	114
4.6.2 <i>Comparison to Recent Earthquakes</i>	119
4.6.3 <i>Comparison to Slow Slip Distribution</i>	121
4.7 <i>Conclusions</i>	122
Appendix A	125
A.1 <i>CGPS Network</i>	125
A.2 <i>Station Optimization vs. Network Optimization</i>	129
A.2.1 <i>Displacement Fields</i>	129
A.2.2 <i>Inversions</i>	130
A.3 <i>Sensitivity Tests</i>	136

Appendix B	147
B.1 Results of Comparison Velocity Field Down Sampling.....	147
B.2 Results of Velocity Field Magnitude Adjustments	149
References	152

LIST OF FIGURES

	Page
Figure 1.1 a) Tectonic and Plate distribution map of the Central America region. b) Inset of Nicaragua, Costa Rica and Panama with seafloor morphology.....	4
Figure 1.2 Schematic diagram of forearc sliver transport from Stein and Wysession [2003]	6
Figure 1.3 Historic earthquake locations and rupture patterns for the Nicoya Peninsula, Costa Rica region.....	10
Figure 2.1 Cartoon representing multipath interaction of GPS satellites signals with other objects before reaching the GPS antenna.	32
Figure 2.2 Representative pictures from a GPS campaign showing the monument pin and a spike mount set up with a Zephyr Geodetic antenna with ground plane.....	37
Figure 2.3 Superposition model of strain accumulation at a subduction zone from [Savage, 1983]. The asthenosphere is indicated by shading. A locked (no slip) condition at an interface is indicated by short horizontal bars crossing the interface	51
Figure 3.1 Regional map of Central America. Black box outlines study area. Map shows variation in oceanic crust origin and topographic relief. MAT is Middle America Trench. EPR is East Pacific Rise crust. CNS is Cocos-Nazca Spreading Center crust. CR is the Cocos Ridge.....	57
Figure 3.2 a) Configuration of CGPS (black triangles). Note SAJU was installed after the 2007 TSE. b) Configuration of seismometers; blue squares indicate 100m borehole seismic vaults, red circles indicate shallow (2-8m) surface seismic vaults. Note SAJU and ACHA were installed after the 2007 TSE.....	58
Figure 3.3 North component of displacement at station QSEC compared to a histogram of cumulative tremor duration per day. The onset and duration of the geodetically determined slow slip correlates well with peaks in the tremor time series.	58
Figure 3.4 Order and timing of CGPS station installation with respect to potential 2003 SSE and 2007 TSE and data availability.....	61
Figure 3.5 Stations are organized in three groups by longitude and within each group by latitude. All fits use station optimized timing parameters a) Time series for the North component of the CGPS stations. b) Time series for the East component of the CGPS stations.....	63

Figure 3.6 North component of station HATI with best-fit model, annotated with model parameters. Although station has relatively poor signal to noise ratio (table 3.2a), the offset U is still clearly defined.....	65
Figure 3.7 Adjusted interseismic velocity vectors relative to stable Caribbean plate (black vectors); and the best fitting surface displacements for the 2007 TSE (red vectors). Iterative velocity fits using station optimized model fits.....	65
Figure 3.8 One hour of seismic tremor, filtered from 2-6 Hz, recorded on the east component at short period borehole (ELVI, PALO, SANL, ARAD), broadband deep vault (ARDO), broadband (CABA, INDI, PNCB, SAR0) and short-period (PNEG, MASP, PUJE, LEPA) surface stations for two different time periods during the 2007 tremor and slip event: a) JD 137 hr 1 and b) JD 141 hr 4. Tremor traces are normalized but the tremor episodes on JD 141 are 2-3 times larger on all stations.....	72
Figure 3.9 Locations of tremor episodes and low frequency earthquakes (LFEs) compared with slow slip distribution.....	73
Figure 3.10 Cross section of fault geometry used for slip inversion from Norabuena et al. [2004].	75
Figure 3.11 Plot of inversion model roughness to wrms, moment and magnitude of maximum displacement for weighted inversion of station-optimized fits. Bold axis indicate the range of models discussed in text. (wrms=8.2 and wrms=4.5).....	77
Figure 3.12 Predicted vs. observed offsets for end member models shown in Figure 3.11. a) Station-optimized timing parameters, weighted inversion, wrms=4.5 mm. b) Station-optimized timing parameters, wrms=8.2 mm. White areas within modeled fault plane indicate negligible or no slip.....	79
Figure 3.13 Along strike and down dip model resolution results, showing minimum resolvable patch size in km.....	80
Figure 3.14 The updated Continuous GPS network configuration since the 2007 TSE	81
Figure 3.15 Interseismic velocity fields from this study (white vectors) and from Norabuena et al. [2004] (blue vectors)	89
Figure 3.16 Interseismic locking pattern from LaFemina et al. [2009] model 3 (left) compared to the inversion results from the preferred model of this study (right).....	90

Figure 3.17 Comparison of the preferred slip mode for the 2007 event, rupture area of the 1950 $M_w=7.7$ earthquake (grey ellipse), the 1978 $M_w=7.0$ earthquake (black dotted ellipse) and the 1990 $M_w=7.0$ earthquake as defined by the 1000 minute aftershocks of Protti et al. [1995] (black ellipse) and locked patch previously identified by Norabuena et al. [2004] (black dashed ellipse). a) Station-optimized timing parameters, weighted inversion, wrms=4.5 mm. b) Station-optimized timing parameters, weighted inversion, wrms=8.2 mm	93
Figure 4.1 Map of Central America with an inset of the Nicoya Peninsula and the Continuous GPS network	95
Figure 4.2 Interseismic velocity field estimated from IGSb-00 time series and a simple straight line fit for the time period between slow slip events. Error ellipses indicate 95% confidence intervals	106
Figure 4.3 Interseismic velocity field estimated from MANA baseline time series and a simple straight line fit for the time period between slow slip events. Error ellipses indicate 95% confidence intervals	108
Figure 4.4 Interseismic velocity field estimated from MANA baseline time series and a hyperbolic tangent fit. Error ellipses indicate 95% confidence intervals.....	110
Figure 4.5 Interseismic velocity field estimated from all three methods; MANA baseline time series and a hyperbolic tangent fit (white), MANA baseline time series and a straight line fit (red), and IGSb-00 time series and a straight line fit (black).....	111
Figure 4.6 a) Best fitting inversion results for the ITRF based straight line fit velocity field (wrms = 5.89 mm). b) Best fitting inversion results for the baseline based hyperbolic tangent fit velocity field (wrms = 2.58 mm). c) Best fitting inversion results for the baseline based straight line fit velocity field (wrms = 4.94 mm).....	113
Figure 4.7 Along strike and down dip model resolution results, showing minimum resolvable patch size in km.....	114
Figure 4.8 Comparison of the model consistent inversions from (b) Norabuena et al. [2004] (c) LaFemina et al. [2009] model 3 (d) this study MANA baseline hyperbolic tangent fit inversion results (e) this study IGSb-00 straight line fit inversion results. This comparison indicates the pattern of migrating area of maximum slip through time...	117
Figure 4.9 Best fitting inversion results overlain by earthquakes occurring in the Nicoya region since 1950. a) Best fitting inversion results for the ITRF based straight line fit velocity field (wrms = 5.89 mm). b) Best fitting inversion results for the baseline based hyperbolic tangent fit velocity field (wrms = 2.58 mm). c) Best fitting inversion results for the baseline based straight line fit velocity field (wrms = 4.94 mm).....	120

Figure 4.10 Comparison of slow slip distribution of Outerbridge et al. [2010] and chapter 3 to the interseismic locking distribution found in this study. a) Slow slip distribution from Outerbridge et al., [2010] and chapter 3. b) Interseismic locking distribution from the velocity field determined by a straight line fit to ITRF time series. c) Interseismic locking distribution from the velocity field determined by a hyperbolic tangent fit to baseline time series. d) Interseismic locking distribution from the velocity field determined by a straight line fit to baseline time series..... 121

LIST OF TABLES

	Page
Table 2.1 Summary of NAVSTAR satellite launch schedule and specifications.....	18
Table 3.1 Nicoya CGPS station specifications.	61
Table 3.2a Station-optimized hyperbolic tangent model fits.....	68
Table 3.2b Network-optimized hyperbolic tangent model fits.....	69
Table 3.3 Results of weighted inversion, iteratively eliminating one station.....	80
Table 4.1 Velocity field from ITRF velocity straight line fit. Rotated to stable Caribbean plate reference frame.	105
Table 4.2 Velocity field from baseline to MANA time series using a straight line fit. Rotated to stable Caribbean plate reference frame.	107
Table 4.3 Velocity field from baseline to MANA time series using hyperbolic tangent fit. Rotated to stable Caribbean plate reference frame.	110

Chapter 1

Introduction

1.1 Geologic Background

Surface deformation observations near active plate boundaries can provide a wealth of information about the processes that control and influence tectonic interactions and seismic energy release. This is true of all styles of plate boundaries: convergent, divergent, and transform, and also holds true on smaller fault scale thrust, normal and strike-slip faults. Surface deformation data combined with a priori information (e.g. fault geometry, rock properties, heat flow, friction... etc.) can be used to construct and test plausible models about driving forces, and the spatial and temporal variability of key parameters such as long term slip rates, coupling between plates or blocks, and poles of rotation between rigid plates or blocks.

Subduction zone plate boundaries have produced some of the largest and most destructive earthquakes in history. The forearc, the area between the subduction trench and arc volcanoes, is the region with the highest seismic hazard and the most complex tectonics. Given the right geography relative to the locus of deformation, there is a lot to be learned about the seismic cycle from subduction zone observations.

The process of building and releasing strain on a fault is the Earthquake Cycle. It is composed of three main parts: coseismic rupture, post-seismic relaxation and interseismic strain accumulation. However, transient slow slip events or continuous creep also occurs. Understanding these processes helps us to understand the earthquake process.

This dissertation will focus on the Cocos-Caribbean plate boundary, using Global Positioning System (GPS) data to study the subduction earthquake process by comparing data to geologically reasonable and self-consistent models. For the Cocos-Caribbean convergent plate boundary, the focus will be on the categorization of energy release mechanisms and their influence on the seismic pattern of the Nicoya Peninsula of Costa Rica, positioned over the Middle America Trench.

1.2 Episodic Tremor and Slip

Episodic Tremor and Slip (ETS) events are repeated, slow dislocations on the subduction zone fault interface that are accompanied by seismic tremor. Seismic tremor is a long lasting vibration that differs from tectonic earthquake recordings in its very long duration, lack of impulsive seismic arrivals and low dominant frequencies. ETS events may reflect processes in the transition zone between locked and aseismically slipping portions of the subducting slab interface [*Ito et al.*, 2007; *Kato*, 2003; *Schwartz and Rokosky*, 2007]. The slip direction of the upper plate is opposite to plate motion, as in standard earthquakes, recovering strain accumulated since the last slip event, but the rate of slip is orders of magnitude slower than standard earthquakes. ETS events were first observed in the Cascadia subduction zone [*Brudzinski and Allen*, 2007; *Dragert et al.*, 2001; *Melbourne et al.*, 2005] and have since been identified in several other subduction zones including Japan [*Hirose et al.*, 1999; *Hirose and Obara*, 2005; 2006; *Igarashi et al.*, 2003; *Ito et al.*, 2007; *Ozawa et al.*, 2001; *Ozawa et al.*, 2002; *Ozawa et al.*, 2003; *Ozawa et al.*, 2004; *Ozawa et al.*, 2007], and Mexico [*Brudzinski et al.*, 2007; *Franco et al.*, 2005; *Kostoglodov et al.*, 2003; *Larson et al.*, 2004; *Larson et al.*, 2007; *Lowry et al.*,

2001]. Other subduction zones, such as New Zealand, have identified deviations of this slow strain release process, where slip can occur on the up-dip portion of the fault plane, and seismic tremor is absent [Douglas *et al.*, 2005; McCaffrey *et al.*, 2008]. Duration of the slip events can last for days or weeks, e.g. 6-15 days along the Cascadia subduction zone [Dragert *et al.*, 2001] or 2-5 days on the Nankai subduction zone in Japan [Ito *et al.*, 2007]. Despite the fact that these events are aseismic, they are accompanied by tremor-like seismic signals that originate from the same, or nearby regions [Igarashi *et al.*, 2003; Ito *et al.*, 2007; Kao *et al.*, 2005; Rogers and Dragert, 2003; Shelly *et al.*, 2006]. There is some evidence that these events also have a recurrence interval that may vary from one region to another [Brudzinski and Allen, 2007; Dragert, 2007; Igarashi *et al.*, 2003; Miller *et al.*, 2002; Shelly *et al.*, 2006]. Repeat times range from 14 months in central Cascadia [Szeliga *et al.*, 2008] to 6 years in the Bungo Channel Japan [Ozawa *et al.*, 2004; Ozawa *et al.*, 2007], and may in fact be random in some locations.

ETS events increase stress up-dip from the locus of maximum slip; this up-dip region is often the rupture zone for megathrust earthquakes [Ito *et al.*, 2007]. In addition, these events may have important cause and effect relationships with other processes occurring within the subduction zone. The physical mechanism for ETS events is still debated but tremor and slip generation has been related to high pore-fluid pressures created by dehydration reactions in subducted oceanic crust and sedimentary cover [Ito *et al.*, 2007; Shelly *et al.*, 2006] as well as temperature influences [Dragert *et al.*, 2001; Peacock and Wang, 1999; Peacock *et al.*, 2002]. The temperature profiles of the well studied relatively warm Japan and Cascadia subduction zones are in sharp contrast to the cooler Costa Rican system.

1.3 Costa Rica: Regional Tectonics

The Middle America Trench is evidence of a convergent margin that extends from Sonora Mexico to Panama. Deformation in this region involves the interaction of six plates, the North American, Rivera, Caribbean, Cocos, Nazca and South American plates (Figure 1.1). The Pacific coast of Costa Rica lies along the Middle America Trench, where, subduction occurs between the Cocos and Caribbean plates. Due to its complex tectonic history, characteristics of Cocos-Caribbean subduction are highly variable from north to south. For example, the Cocos and Caribbean plates are undergoing varying high rates and obliquity of convergence ranging from 9.1 cm/year and truly orthogonal in southern Costa Rica to 7.6 cm/yr and 25° counter-clockwise of orthogonal off shore Nicaragua [DeMets, 2001]. Oblique subduction has been cited as a contributing factor to the complex tectonics observed in Costa Rica, including along the Nicoya Peninsula.

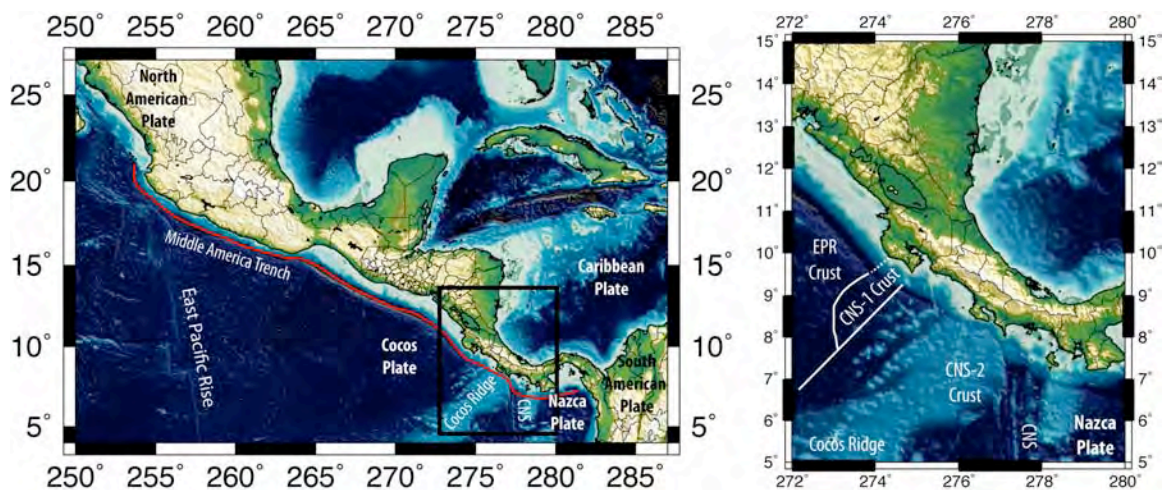


Figure 1.1. a) Tectonic and Plate distribution map of the Central America region. b) Inset of Nicaragua, Costa Rica and Panama with sea floor morphology.

Forearc Sliver Transport was first described by Fitch [1972]. It occurs in areas where coupling between the over riding continental and down going oceanic plates is strong and the convergence direction is oblique. This style of strain partitioning is

postulated to be present in at least 50% of modern subduction zones [Jarrard, 1986]. Since its initial description forearc sliver transport has been identified and investigated in several subduction zones such as Sumatra [McCaffrey, 1992; McCaffrey *et al.*, 2000], the paleo-Andes (e.g. Chile, Peru, Ecuador) [Beck, 1998; Jarrard, 1986], Southwest Japan [Fitch, 1972; Kaneko, 1966; Okada, 1971] and Central America [LaFemina *et al.*, 2009; LaFemina *et al.*, 2002; Lundgren *et al.*, 1999; McCaffrey, 2002; Norabuena *et al.*, 2004; Turner *et al.*, 2007]. The trench parallel motion can be accommodated in several different ways such as motion along distinct strike slip, trench parallel faults (i.e. Sumatra [Corti *et al.*, 2005; McCaffrey, 1992; McCaffrey *et al.*, 2000]), motion on sets of conjugate faults, as in southern Costa Rica [Marshall *et al.*, 2000], bookshelf faulting, as in Nicaragua [LaFemina *et al.*, 2002; McCaffrey, 1992; 1996] or by some other combination of strike slip fault trends. Fitch [1972] stipulates that these mechanisms may be facilitated by weakness due to high heat flow along arc volcanoes, and allow lateral translation of the forearc sliver, bounded by the strike-slip faults and the subduction trench, in the direction of obliquity (Figure 1.2).

The origin of the Cocos Plate influences the complexity currently observed. The Cocos Plate became a discrete entity 22.7 Ma with the breakup of the Farallon Plate [Barekhausen *et al.*, 2001]. New oceanic crust continued to be formed at two spreading centers. The East Pacific Rise (EPR) to the west (Figure 1.1), a fast spreading center, has produced smooth oceanic crust [Hey, 1977]. The Cocos-Nazca spreading center (CNS) to the south (Figure 1.1) began as a fast spreading center, producing smooth oceanic crust (CNS-1). At 19 Ma the ridge jumped, transferring the CNS-1 crust from the Nazca Plate to the Cocos Plate and rotating the spreading center 22° to the East. This jump

transitioned the spreading center to a slower spreading rate, creating a more topographic crust (CNS-2) [Meschede *et al.*, 1998]. The Cocos-Nazca spreading center continues to execute small southward jumps, forcing counterclockwise rotation of the Cocos Plate [Barckhausen *et al.*, 2001]. This series of ridge jumps and variation in topography of the erupted oceanic crust has a large impact on Cocos-Caribbean subduction, including friction due to asperities on the slab interface, heat flow and temperature profiles of the down going slab and subduction fluid migration.

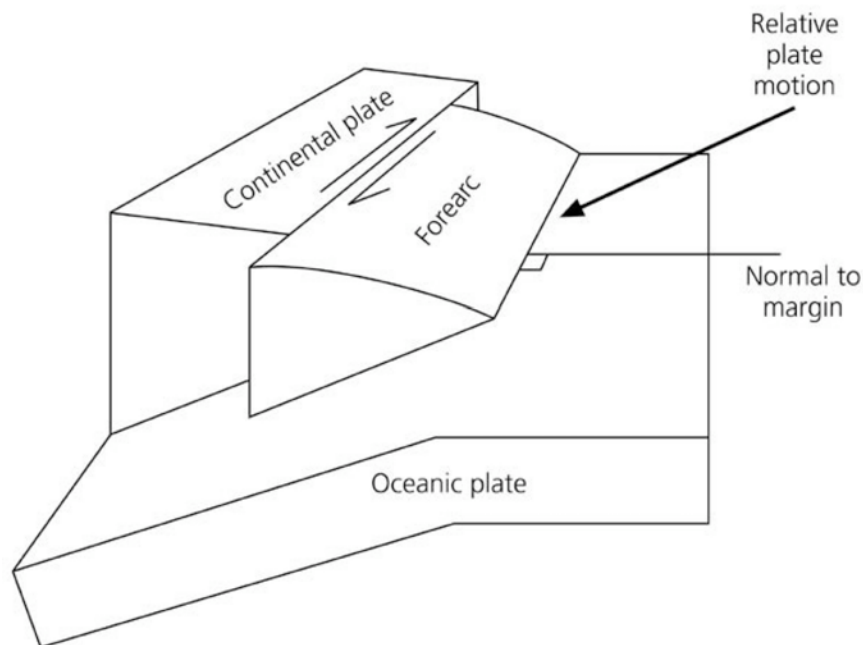


Figure 1.2. Schematic diagram of forearc sliver transport from Stein and Wysession [2003]

Even over the relatively small portion of the Middle America Trench that is occupied by Costa Rica, there is a large variation in the morphology of the sea floor of the down going Cocos plate. Western Costa Rica has two peninsulas, Nicoya to the north and Osa in the south, elongated in the northwest-southeast direction, parallel to the Cocos-Caribbean plate boundary. Off the southern coast the Cocos Ridge stands ≥ 2 km

above the surrounding ocean floor [Walther, 2003] and is interacting with the Osa Peninsula. To the north of the Cocos Ridge is an area 40% covered with seamounts, including the Quepos Plateau and the Fisher Seamount which transitions to a smooth down going slab beneath the Nicoya Peninsula [Hinz *et al.*, 1996; von Huene *et al.*, 1995]. The delineation between rough and smooth ocean bottom topography corresponds to the boundary between CNS-1 crust and CNS-2 crust, which is overprinted by Galapagos hot spot volcanism. The CNS-1/CNS-2 boundary intersects the Central American isthmus near the southern tip of the Nicoya Peninsula and is demarcated by the location of the Fisher Seamount [Barckhausen *et al.*, 2001; Hinz *et al.*, 1996; Von Huene *et al.*, 2000]. The morphology of the down going slab has an impact on the upper plate tectonics [Fisher *et al.*, 1998; Fisher *et al.*, 2004; Gardner *et al.*, 1992; Gardner *et al.*, 2001; Sak *et al.*, 2004; Von Huene *et al.*, 2000] and may impact the nature of earthquake rupture along the margin [Bilek *et al.*, 2003].

In southern Costa Rica and northern Panama, the interaction of the Cocos and Caribbean Plates is not as straightforward as simple subduction. The Panama Block is defined to the north by the central Costa Rican Deformed Belt and the CNS-1/CNS-2 boundary off shore [Marshall *et al.*, 2000] and to the south by the Azuero Peninsula, Panama [Mann and Corrigan, 1990; Silver *et al.*, 1990]. Its overall motion is to the ENE with respect to the Caribbean Plate [Lundgren *et al.*, 1999].

This ENE motion is driven not only by oblique convergence but also by interaction with the Cocos Ridge. Offshore of the Osa peninsula the buoyant aseismic Cocos Ridge is intersecting the Central American Isthmus. The crust here has become thickened (in places exceeding 20 km thick [Walther, 2003]) by interaction with the

Galapagos hot spot; consequently the plate is buoyant and difficult to subduct. The Cocos Ridge collision with the Osa Peninsula causes uplift and upper plate deformation [LaFemina *et al.*, 2009]. The Fila Costeña fold and thrust belt accommodates shortening from the collision tectonics at rates of 10-40 mm/yr and as much as 15km of total shortening [Fisher *et al.*, 2004; LaFemina *et al.*, 2009; Marshall *et al.*, 2000; Sitchler *et al.*, 2007]. The Cordillera de Talamanca stands at ~4 km height and serves as a backstop to motion and provides evidence for rapid uplift. The collision has moved mass laterally against the mountain range, causing tectonic escape to the NW and SE. The component of this escape that is directed NW, has been cited as a possible additional driving force to the forearc sliver transport occurring from central Costa Rica through El Salvador [Corti *et al.*, 2005; Dixon, 1993; LaFemina *et al.*, 2009; LaFemina *et al.*, 2002; Trenkamp *et al.*, 2002; Turner *et al.*, 2007].

There is an appreciable change in the slab dip, age and thermal structure, also related the genetic history of the Cocos Plate. The dip variability beneath Nicaragua and Costa Rica can be shown by seismically illuminating the Wadati-Benioff zone [Protti *et al.*, 1995a] and by imaging depth to top of basement [Protti *et al.*, 1995a; Von Huene *et al.*, 2000]. The dip of the Wadati-Benioff zone shallows from north to south, with a distinct bend at the Nicaragua-Costa Rican boarder, from 84° to 60°. There is also evidence of a tear, the Quesada Sharp Contortion, inboard of the Southern tip of the Nicoya Peninsula at a depth >70km; the tear is revealed by offset surface projection of the slab depth contours by ~15 km [Protti *et al.*, 1995a]. This tear lies very close to, if not on, the extension of the demarcation between CNS-1 and CNS-2 crust and the rough-smooth bathymetry boundary. This offset in the down going slab may be related to the

age and or smoothness of the slab [Protti *et al.*, 1995a]. CNS-2 crust to the SE is younger (18-19 Ma), more buoyant and more topographic than the CNS-1 crust to the NW (21-23 Ma) [Barckhausen *et al.*, 2001; Hey, 1977; Von Huene *et al.*, 2000]. There is no evidence of the Wadati-Benioff zone beneath the Osa Peninsula below 50 km [Husen *et al.*, 2002; Protti *et al.*, 1995a]. The age of the down going slab is between 15 and 16 Ma [Barckhausen *et al.*, 2001], most likely related to Cocos Ridge collision.

Oceanic crust cools as it ages and moves away from the ridge crest, resulting in a heat flow distribution that is proportional to the square root of the age of the crust. It follows that if the age of the down going CNS-1 crust (21-23 Ma [Barckhausen *et al.*, 2001; Hey, 1977]) is younger than the down going EPR crust (24-25 Ma [Barckhausen *et al.*, 2001]), the heat flow of the CNS-1 crust is expected to be higher than that of the EPR crust. Spinelli *et al.* [2006] demonstrate that not only is the heat flow of the CNS-1 crust higher at 105 mW/m^2 , but also that the modeled isotherms in the over riding plate in southern Nicoya, have a steeper gradient than those in the northern Nicoya Peninsula where the EPR crustal heat flow values are only 20 mW/m^2 . Hutnak *et al.* [2007] attributes lower heat flow in the EPR crust to higher incidence of hydrothermal cooling through seamounts and other outcrops seaward of the trench, which are more common on EPR generated crust than CNS-1 crust which has no identified seamounts.

1.3.1 Nicoya Peninsula, Costa Rica

The Nicoya Peninsula in northern Costa Rica is located between 9° N and 11° N , and will be the focus of this dissertation (Figure 1.3). Along the Nicoya region the convergence direction is $\sim 10^\circ$ counter-clockwise from the trench-normal direction [Argus

and Gordon, 1991; DeMets *et al.*, 1994; DeMets, 2001]. Along this segment of the Middle America Trench, between the North America-Cocos-Caribbean triple junction [Guzman-Speziale, 2001] and the central Costa Rican deformed belt [Marshall *et al.*, 2000], convergence is partitioned, perhaps due to the obliquity of convergence. Strain is partitioned in such a way that subduction close to the trench-normal direction occurs at a rate of $74-84 \pm 5$ mm/yr, while northwest-directed arc-parallel shear occurs at rates that between about 14 ± 4 mm/yr [DeMets, 2001] and 8 ± 3 mm/yr [Inuma *et al.*, 2004; LaFemina *et al.*, 2009; Norabuena *et al.*, 2004], associated with northwest motion of a fore-arc “sliver block”, which includes the Nicoya Peninsula.

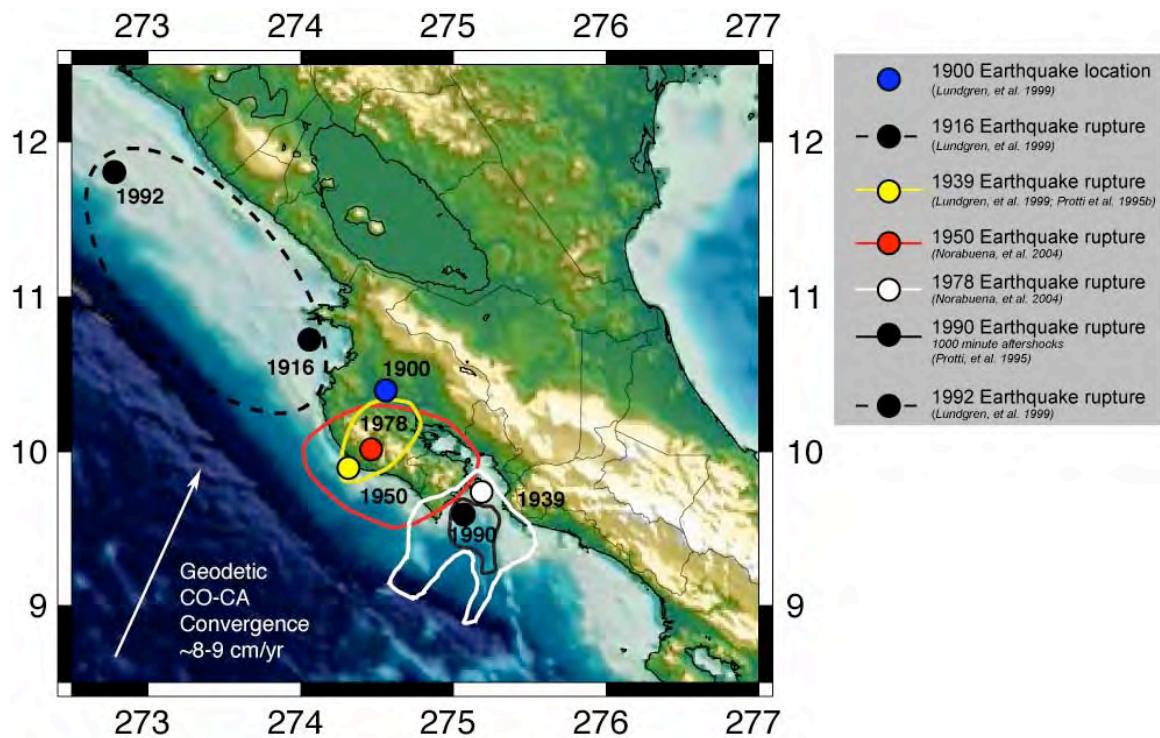


Figure 1.3. Historic earthquake locations and rupture patterns for the Nicoya Peninsula, Costa Rica region.

The close proximity of the Nicoya Peninsula to the trench (~ 50 km), and its position directly over the seismogenic zone [DeShon *et al.*, 2003; DeShon *et al.*, 2006;

Newman et al., 2002; *Norabuena et al.*, 2004], allows geodetic and seismic instrumentation to be placed close to the focus of strain accumulation and release, making it a prime location to study seismic processes on a subduction zone plate boundary.

1.3.2 Nicoya Peninsula rupture history and coupling

It is important to understand the first order seismic cycle of a region as well as its uncertainties in order to be able to study effectively the second and third order perturbations to this cycle. Furthermore, understanding the seismic hazard for the Nicoya Peninsula is crucial to saving lives, property and for making well-informed policy decisions. The Nicoya Peninsula has a history of large ($M > 7$) earthquakes. June 21, 1900 saw an $M_s = 7.2$, and on April 24, 1916 there was an $M_s = 7.4$ just north of the Nicoya Peninsula (Figure 1.3) [*Nishenko*, 1991]. On October 5, 1950 a potentially more complex $M_w = 7.7$ occurred on the seismogenic zone directly below the Nicoya peninsula [*Nishenko*, 1991]. This was the last large earthquake to fully rupture the seismogenic zone under the Nicoya peninsula. This earthquake resulted in $>1\text{m}$ of coseismic uplift along the coast of the Nicoya Peninsula [*Marshall*, 2007]. It is clear from the continued subsidence along the Pacific coast of the peninsula that subsequent earthquakes with smaller rupture areas (Figure 1.3) have not released all of the strain that has accumulated since this great earthquake. For example, the August 23, 1978, $M_w = 6.9$, ($M_s = 7.0$) event ruptured off shore of the Nicoya peninsula, in the area of the 1950 event. However the rupture geometry of this event was significantly smaller and did not rupture the entire region (Figure 1.3). This area has been identified by *Nishenko* [1991] as a seismic gap with a calculated a 98% chance of an $M 7.3$ or larger earthquake before 2009 in the

region of the 1950 rupture area. This information was presented after the 1978 earthquake and suggests a 22 ± 2 year recurrence. It has been suggested that the 1950 event represents a unique and complex process [Nishenko, 1991] that based on the cumulative slip deficit could rupture an $M_w \geq 7.5$ earthquake [Linuma *et al.*, 2004]. Analysis of second order processes may help to shed light a complex system.

Further south, on March 25, 1990 there was an $M_w = 7.0$ earthquake at the mouth of the Gulf of Nicoya (Figure 1.3). Husen *et al.* [2002] show that the likely cause of this earthquake was an asperity from a subducted seamount. From Protti *et al.* [1995b], it is clear that the rupture area of this earthquake abuts but does not infringe upon the Nicoya seismic gap as described by Nishenko [1991], with a SE directed rupture, away from the Nicoya seismic gap. A similar $M_s = 7.1$ earthquake in this region in 1939 [Pacheco and Sykes, 1992] is believed to have similar rupture area to the 1990 Gulf of Nicoya earthquake (Figure 1.3). This suggests a 50-year earthquake cycle in this region. In September 1992 there was an $M_w = 7.6$ ($M_s = 7.2$) tsunamigenic earthquake that also had a SE directed rupture pattern, that terminated at the NW extent of the Nicoya seismic gap [Ihmle, 1996; Kanamori and Kikuchi, 1993; Piatanesi *et al.*, 1996; Protti *et al.*, 1995b] (Figure 1.3). This all seems to indicate loading of the seismogenic zone beneath the Nicoya Peninsula.

By looking at these large earthquakes ($M > 7$) as well as prevailing micro-seismicity it is possible to identify the local seismogenic zone. Consistent with the offset of Wadati-Benioff zone, which is deeper to the south [Protti *et al.*, 1995a], and the shift from EPR and CNS-1 crusts, both Newman *et al.* [2002] and DeShon *et al.* [2006] find variation in the up dip limit of seismicity under the Nicoya peninsula. Newman *et al.*

[2002] find that to the north the seismogenic zone ranges from 20-30 km vertical depth, with diffuse, intraplate seismicity occurring to ~60km, and to the south that the seismogenic zone ranges from 10-30 km vertical depth. *DeShon et al.* [2006] similarly find by micro-seismicity that beneath the northern Nicoya peninsula the seismogenic zone ranges from 17 to 28 km vertical depth and beneath the southern Nicoya peninsula, from 12 to 26 km vertical depth. It has been offered by *Spinelli and Saffer* [2004] that this offset in up dip limit of seismicity is due to the dissipation of fluid overpressures which alters the frictional conditions on the fault plane.

1.3.3 Interseismic Coupling

It is also useful to analyze the pattern and extent of coupling on the subduction zone interface during the interseismic period. There have been several studies investigating the pattern of coupling on the interface beneath the Nicoya Peninsula. *Lundgren et al.* [1999] estimated from inversion of GPS data that there was heterogeneous locking under the Nicoya peninsula reaching a maximum of 80% locked in the central and southeast region of the peninsula.

Norabuena et al. [2004] used geodetic data from 15 campaign GPS sites to invert for the locking pattern on the plate interface under the Nicoya Peninsula. These authors used campaign GPS to estimate an interseismic velocity field, and a backslip model [*Savage, 1983*] to define locked patches centered at 14 ± 2 km depth, locked at ~65% of the convergence rate, and at 39 ± 6 km, locked at ~50% of the convergence rate. The two patches straddle the up dip and down dip limits of the seismogenic zone presented by *DeShon et al.* [2006].

LaFemina et al. [2009] present a study that models a GPS velocity field from El Salvador to Northern Panama for percent of interseismic coupling. They use both continuous and campaign GPS measurements to invert for coupling using DEFNODE modeling code [*McCaffrey*, 2006]. DEFNODE is a block model that uses both horizontal and vertical components of the GPS data, allows variation of constraints on block boundaries as well as locking and simultaneously inverts for coupling and block motions. *LaFemina et al.* [2009] present four flavors of models, varying from highly constrained coupling input parameters to unconstrained coupling input parameters as well as two different types of block boundaries. All four presented models indicate heterogeneous coupling beneath and off shore of the Nicoya Peninsula, with the highest coupling values concentrated in the Northeast region of the peninsula but is on average 50% coupled [*LaFemina et al.*, 2009].

1.3.4 Thesis Development

None of the GPS studies described above account for the presence of slow slip or Episodic Tremor and Slip events, which may periodically and/or aseismically change the amount and pattern of strain. The measurements in these studies would in effect average over this signal and should therefore be considered minimum estimates of coupling. In 2003 a possible slow slip event was identified by a transect of three GPS stations on the Nicoya Peninsula [*Protti et al.*, 2004]. Due to the limited data, characterization of the event was difficult. This event prompted the installation of a larger continuous GPS (CGPS) and seismic networks with more comprehensive coverage. These networks captured a second event in 2007 both in the geodetic and seismic datasets. Chapter 3 and

Outerbridge et al., [2010] describe this event as well as inversion results for slip on the fault plane during the Tremor and Slip Event (TSE). Specifically, I characterize the Tremor and Slip Event that occurred in 2007 and answer the following questions:

- 1) What is the slip pattern of the 2007 TSE?
- 2) What is the relationship of the distribution of slip during the TSE to the pattern of rupture in historic earthquakes?
- 3) What does the event slip pattern indicate for future earthquake rupture patterns and magnitudes?

The appearance of a slow slip event in the geodetic data leads to new estimates of interseismic velocity. This revised velocity field remedies the temporal aliasing of [*LaFemina et al.*, 2009; *Lundgren et al.*, 1999; *Norabuena et al.*, 2004]. Chapter 4 presents this new velocity field as well as inversions for locking on the fault plane between Tremor and Slip Events and a comparison between two different inversion codes in an effort to answer the following questions:

- 1) How does the pattern and magnitude of locking change when inverting with GPS velocities that have been adjusted for the occurrence of a TSE?
- 2) How does the pattern of locking during the interseismic compare to the pattern of strain release during TSE's and Earthquakes?
- 3) What effect, if any, does the addition of vertical data and the modeling block boundary interactions have on the distribution and magnitude of interseismic locking?

Together these studies present an internally consistent analysis of interseismic strain and an Episodic Tremor and Slip event.

CHAPTER 2

Methodology: The Global Positioning System (GPS) and Tectonic Modeling

GPS geodesy utilizes a satellite constellation to resolve three-dimensional position. Precise clocks on board each satellite and ground receiver allows position estimation and subsequent calculation of displacement and velocity. These data can be used to solve geologic problems relating to the kinematics of earth surface processes. GPS time series provide a four-dimensional record of the location of point on the earth's surface. By analyzing groups of site velocities it is possible to study the motion of faults, plate boundaries, blocks and plates, as well as their relationships to each other. When GPS measurements are coupled with two and three-dimensional modeling techniques they can provide insight into the details of kinematic and dynamic processes.

The studies in this thesis are primarily based on data from GPS and the application of theoretical geologic models to these data. In order to understand why these data are appropriate for studies of this nature, it is useful to understand how GPS works. The first part of this chapter summarizes how GPS works, and its application to geodesy and plate tectonics. The latter part of this chapter will discuss the fundamentals of modeling techniques, with a focus on elastic half space and block modeling.

2.1 The Global Positioning System

The information contained in this section is primarily a summary of information found in *Dixon* [1991], *Parkinson and Spilker* [1996a; b] and *Wdowinski*, [personal communication] and on the following websites unless otherwise noted.

www.astronautix.com/project/navstar.htm

www.faa.gov

http://www.spaceandtech.com/spacedata/constellations/navstar-gps_consum.shtml

www.unavco.org

The GPS system is partitioned into three segments:

1. The Space Segment
2. The Control Segment
3. The User Segment

2.1.1 The Space Segment

The Space Segment is made up of the Navigation Signal Timing and Ranging (NAVSTAR) satellite constellation, commissioned by a Department of Defense joint program, formed in 1973. The plan they devised was a synthesis of several previous projects, including the Naval Navigation Satellite System, which used radio transmitted satellite position data (ephemeris data) and Doppler information to locate Navy vessels. The addition of very precise atomic clocks (accurate to a nanosecond) to the Naval Timing Satellites, in the early 1970s, allowed for autonomous and more accurate prediction of satellite orbit locations. Air Force Project 621B, in 1972, employed pseudorandom noise (PRN) to modulate and transmit information along the satellite ranging signal. PRN is a code that repeats on a sufficiently long interval that it appears random to those with no prior knowledge of the pattern of modulation code. NAVSTAR satellites began launching in February 1978, and continue today. Satellites were launched in phases summarized in Table 2.1.

Table 2.1. Summary of NAVSTAR satellite launch schedule and specifications.

Phase	Year Launched	Number of Satellites	Carrier Bands	Modulations
Block 1	1978-1985	11 All retired	L1, L2, S	C/A, P
Block 2	1989-1990	9 All retired	L1, L2	C/A, P
Block 2A	1990-1993	18 (11 remaining)	L1, L2	C/A, P
Block 2R	1997-2007	17 (12 remaining)	L1, L2,	C/A, P
Block 2R-M	2007-	6 (2 remaining)	L1, L2	C/A, P, M, L2C
Block 2F	2009-	6	L1, L2, L5	C/A, P, M, L2C
Block 3	2014	TBD	L1, L2, L5, S	C/A, P, M, L2C, L1C

The purpose of Block I was to test the ability and accuracy of GPS technologies and applications. These satellites are in Medium Earth Orbits at 20,200 km, spaced at right ascension and inclined 63° above the equator. Blocks 2 and 2A were designed as replacements for the Block I satellites. Current NAVSTAR Satellites operate in Medium Earth Orbit at an inclination of 55° relative to the equator and have an orbital period of one half of a sidereal day (11 hours 58 minutes). There are a total of six circular orbital planes that are evenly spaced at 60° from each other. Each plane has four functional and one spare satellite. The most significant improvements with consecutive satellite blocks were the life of the satellite and the length of time that each be autonomous, without communicating with the control segment ground station (described in section 2.1.2). In 1997, the Department of Defense began replacing Block 2 and 2A satellites with Block 2R and 2R-M. These satellites have reprogrammable processors that allow them to be redirected in flight when linked to the ground control station.

Each satellite sends out two carrier frequencies, L1 at 1575.42 MHz and L2 at 1227.6 MHz. The carrier frequencies are created by an atomic clock, which operates as a stable oscillator on board the satellite. The carrier frequencies each have radio signal modulations imprinted on them. All modulations are pseudorandom noise codes, considered to be square waves with a value of ± 1 . L1 (19 cm wavelength) carries two modulations simultaneously, the Course/Acquisition Code (C/A) and the Precise Code (P1). The C/A-code is sent at 1.023 MHz, and is used to acquire the P-code. Access to the C/A-code is for civilian users and is only available on L1. L2 (24.4 cm wavelength) has only a P2-code modulated on it. The P(Y)-code is an encrypted code that is broadcast at 10.23 MHz (known as the Y code in its encrypted state). The higher bandwidth of this modulation reduces noise in the data. There is a final modulation (D) on both carrier waves that communicates the satellites position (ephemeris parameters), other relative satellite positions, as well as health of the satellite, information for atomic clock corrections (so that they may all be synchronized and/or bias corrected), and the information for the C/A-code to unlock the P-code when possible. Geodetic grade GPS receivers have access to all carrier waves and modulations.

Blocks 2R, 2R-M, and 2F have a C modulation added to them, L2C, a modulation that will allow civilian use of the L2 band. Signals from block 2R-M satellites contain an additional M modulation, on both L1 and L2 carrier frequencies, which is readable only by military receivers. The M-code is an improvement over the Y-code, providing better anti-jamming capabilities. Satellites on Blocks 2F and 3 have a third carrier frequency, the L5, at 1176.45 MHz; this band is only available for protected aeronautical use. Finally, Block 3 satellites are projected to have an L1C civilian code modulation as well

that will allow incorporation of NAVSTAR signals with the European Galileo system and the Japanese Quazi-Zenith Satellite system.

2.1.2 The Control Segment

The 50th Space Wing of the U.S. Air Force Space Command oversees operations of the Control Segment, which consists of nine components. The GPS Master Control Station is located at Schriever Air Force Base in Colorado Springs, Colorado. There are five monitoring stations located in Colorado, Hawaii, Ascension Island, Diego Garcia and Kwajalein Atoll. Ascension Island, Diego Garcia and Kwajalein Atoll each also have a ground antenna associated with the monitoring station.

The role of the control segment is to ensure that the orbit and atomic clock of the satellite remain within acceptable limits and do not drift too far from predictable values. The job of the master control station is to calculate the position, velocity, right ascension and declination parameters for periodic upload to the satellite. The monitoring stations are responsible for predicting the behavior of the satellites between downlink times. This information is transmitted to the user segment along with the true position data of the satellite. Any calculated variation between true and predicted values in position of the satellite or atomic time is transmitted to the user segment, which can calculate necessary corrections.

2.1.3 The User Segment

The User Segment is comprised of the GPS receiver and antenna. The goal of the user segment is to calculate the latitude, longitude, altitude, and time for a specific

location occupied by a receiver/antenna pair. In order to complete these calculations a minimum of four satellites need to be in view of the antenna. The antenna locks on to the satellites when it comes into view, acquires the signal sent by the satellite and transmits it to the receiver to be stored and deciphered. With the full 24 satellite constellation, all places on earth have a minimum of 4 satellites in view at all times, and on average 6-8 are visible above the horizon.

The receiver has been preprogrammed with knowledge of the signal patterns transmitted by the satellites. The receiver runs a cross-correlation comparison of the signal acquired by the antenna and when there is a match, the antenna is considered locked on that satellite.

There are three types of receivers that can be used with the GPS satellites, those that use code correlation, codeless correlation, and combined code and codeless correlation. Code correlating receivers calculate pseudoranges by comparing the C/A and P codes transmitted by the satellite to a predicted P code generated by the receiver clock using *a priori* information.

In a general sense, the receiver calculates its position based on a comparison between the time and position information contained in the radio signal transmitted by the satellite, and information contained in the receiver itself. The satellite transmits its location (x_s, y_s, z_s) and the time that it sent the signal (t_s). The receiver works in conjunction with the satellite to create a template wave and then calculates the shift in the wave form and compares the time it received the signal from the satellite (t_r) to the time that point was generated by the receiver (which in a perfect world would be equal to the time sent by the satellite). The difference between these two times (t_d) provides the

pseudorange (ρ), or distance from the satellite to the receiver when t_d is multiplied by the speed of light (c).

$$t_d = t_r - t_s \quad 2.1$$

$$\rho = c(t_d) \quad 2.2$$

Thus the GPS receiver is located on a sphere with a radius D around the satellite. If D is calculated for three different satellites, the three resultant spheres will intersect to give the location (x_r, y_r, z_r) for the GPS receiver on the surface of the earth. The motion of the satellite and other noise sources complicates these simple equations.

Equations 2.1 and 2.2 assume that the satellite and receiver clocks are perfectly synchronized. Since this is hardly ever the case, time on the receiver clock is considered to have a bias (b_r) and the time on the receiver (t'_r) is composed of the true time (t_r) and this bias.

$$t'_r = t_r + b_r \quad 2.3$$

This relationship holds true for the satellite clock as well. It is because this bias is present that the calculated distance between the satellite and the receiver is a pseudorange (ρ).

$$\rho_t = c(t_r - t_s) + c(b_r) \quad 2.4$$

ρ_t is the true pseudorange to a given satellite. However, as before, this equation and the actual measured pseudorange (ρ_m) is complicated by noise sources, which will be discussed in section 2.1.5.

The accuracy of code-correlating receivers is tens to hundreds of meters, depending on the number of satellites in view. The accuracy of the position estimates are limited by the wavelength of the modulation used to calculate the pseudorange, and are approximately equal to one half the wavelength of that modulation. The C/A modulation

has a wavelength of ~300m, and the P code has a wavelength of ~30m, yielding an accuracy of tens to hundreds of meters depending on the number of satellites in view and access to the P code. Using GPS for Navigation is an example of an application where code-correlating receivers would be used.

Codeless receivers have no preprogrammed knowledge of the satellite carrier signal. Therefore, they can use the C/A code to extract the received phase of the L1 and L2 carrier signal. This phase is cross-correlated with transmitted phase to find the phase difference. This particular method reduces the signal to noise, but has a shorter wavelength, which improves position estimates to meter or sub-meter accuracy.

A combined code and codeless correlating receiver uses a combination of the two previous techniques. The receiver generates a carrier frequency from the transmitted P-code and D modulation and cross-correlates the phase of the generated signal with the transmitted signal of both L1 and L2. The receiver has internal knowledge of the modulation codes, providing better signal to noise and allowing for sub-centimeter accuracy using these receivers. In this way the receiver calculates the pseudorange. This is the style of receiver used for geodetic GPS measurements.

As stated, it is possible to use the phase of the carrier signal to obtain change of distance information.

$$\delta = n\lambda + \phi\lambda \quad 2.5$$

$$= (v_\phi/f) (n + \phi) \quad 2.6$$

where (δ) is the change of distance, n is the integer number of carrier wavelengths (an unknown), ϕ is the phase, λ is the wavelength, f is the frequency, and v_ϕ is the phase velocity. Due to sampling rate restrictions, the carrier signal is sampled and mixed with a

signal created by the receiver's internal clock and previous knowledge of the transmitted signal, low pass filtered, and then resampled. This approach is useful because the wavelength of the carrier signal (L1 or L2) is much shorter than the code modulations.

With the information provided by the raw GPS (pseudorange estimations and phase information), it is possible to process the data in such a way that n can be solved for, along with other parameters, which can increase the accuracy of the position estimates to sub centimeter. This process is required for geodetic GPS and will now be explored further.

2.1.4 Sources of Uncertainty

Using GPS, it is possible to locate the precise position of a point on the earth's surface with sub-centimeter precision, known as precise point positioning. There are several obstacles to reaching this level of precision and accuracy but with proper understanding of GPS structure and sophisticated data processing, it is attainable.

The first barrier to high precision GPS was the controlling agency. The United States government has the capability to restrict the accuracy of GPS for security purposes. Selective Availability (SA) is an error that can be imposed by the Department of Defense that limits the accuracy of the signal. This "scrambling" of the signal degrades the accuracy of the L1 C/A to 100m by altering the satellite clock and broadcasting less accurate ephemeris parameters (one nanosecond of deviance on the atomic clock yields $> 1,000$ km of uncertainty in the satellite orbital position). Selective Availability was discontinued in May 2000.

There are six major categories for sources of ranging errors in GPS:

- 1) Satellite ephemeris
- 2) Satellite clock
- 3) Ionospheric delay
- 4) Tropospheric delay
- 5) Multipath
- 6) Receiver/user errors

As mentioned in the previous section the measured pseudorange (ρ_m) is the sum of the true range (ρ_T) and the above noise sources.

$$\rho_m = \rho_T + \Delta D_i - c \Delta b_i + c (\Delta T_i + \Delta I_i + v_i + \Delta v_i) \quad (7)$$

Where for the i th satellite ΔD is the satellite position error; v is the receiver measurement noise; ΔI is the ionospheric delay; ΔT is the tropospheric delay; and Δv is the relativistic time correction. The relativistic time correction is used to account for satellite motion, user motion, as well as Earth's rotation and gravitational field.

2.1.4.1 Clock Uncertainties

The position of a GPS receiver in three-dimensional space requires the calculation of the range to three different satellites. In order to correctly locate that calculated position in the fourth time dimension, the use of a fourth satellite is required. As discussed in section 2.1.3, both the satellite clock and the receiver clock contain biases. These clock uncertainties can be canceled between satellites. Given that b_r is the receiver clock bias (deviation from actual time) and b_s is the satellite clock bias the first order time correction $b_r - b_s$ can be applied, leaving only other noise sources to be corrected for.

Another way to approach receiver and satellite clock errors is by single and double differencing. When two receivers (1, 2) are in view of two satellites (i, j) the measured pseudorange (ρ_m) equation for receiver 1 becomes:

$$\rho_{m1}^i = \rho_T^i + c(b_{r1} - b_s^i + \Sigma_1^i) \quad 2.8$$

Where Σ indicates the sum of all other noise sources. Similarly for receiver 2:

$$\rho_{m2}^i = \rho_T^i + c(b_{r2} - b_s^i + \Sigma_2^i) \quad 2.9$$

If these two equations are subtracted, the result is the single difference measured pseudorange, with only receiver clock biases.

$$\rho_m^i = \rho_T^i + c(b_{r1} - b_{r2} + \Sigma^i) \quad 2.10$$

Primed variables denote those that have been differenced. This principle holds true for the second satellite (j) as well.

$$\rho_m^j = \rho_T^j + c(b_{r1} - b_{r2} + \Sigma^j) \quad 2.11$$

Equations 2.10 and 2.11 can then be differenced to eliminate receiver clock biases.

$$\rho_m'' = \rho_T'' + c(\Sigma'') \quad 2.12$$

Thus this double differencing procedure eliminates clock errors and leaves only other sources of uncertainty (listed above).

2.1.4.2 Ephemeris and Orbit Uncertainties

Satellite orbit errors can be accounted for in much the same way when the satellites are relatively close (\ll satellite altitude). The broadcast ephemeris data are uploaded from the Control Segment to each satellite, and then transmitted to user's receiver. Broadcast ephemeris files are accurate to ~ 30 m. However, for geodetic GPS with millimeter accuracy, meter precision in satellite positions is required. More precise orbits are calculated by NASA and the Jet Propulsion Laboratory (JPL) in California and can be obtained for use during processing to replace the corresponding ephemeris parameters. All studies in this thesis use orbits calculated by JPL.

Despite the use of more precise satellite position estimates, these are still merely estimates of where the satellite should be based on previous behavior, and its projected path along its orbit. For geodetic GPS studies it is imperative to know within meters, where the satellite was a precisely the time it sent the signal acquired by the GPS receiver. The location of the satellite in orbit can be described by six parameters at any given time. These six Keplerian elements include the semi major axis a , the eccentricity e of the satellite orbit, f the “true anomaly” which describes the location of the satellite within that orbit, the inclination i that describes the position and orientation of the orbital plane. Of these parameters, only the anomaly is time dependent. Even though the eccentricity of a circular orbit approximates to zero, it is necessary to use more precise values for the precision of geodetic GPS.

One way to approach the precision desired is to begin with estimated values for the six parameters and integrate equations of motion using accurate models for the forces that perturb the circular orbit. These forces include gravitational effects and solar radiation pressure, which applies stress to solar panels with large surface area. Variations in the alignment of these solar panels as well as thermal radiation can also have an effect on the path and speed of these satellites orbits.

2.1.4.3 Propagation Delays: Ionosphere, Troposphere, and Stratosphere

One of the most important sources of uncertainty to account for is propagation delay. This is when the signal transmitted from the satellite is slowed or bent due to interaction with particles in the ionosphere (50-500 km altitude) and troposphere (0-10 km altitude). The magnitude of these delays is small but not negligible and depends

directly on the elevation angle of the propagating signal and the specific atmospheric conditions in which the receiver is located. Specific effects that must be accounted for include ionospheric group delay and scintillation, group delay from wet atmosphere, group delay from dry atmosphere, and atmospheric attenuation in the troposphere and stratosphere.

2.1.4.3.1 The Ionosphere

The ionosphere is a frequency dispersive medium that causes two main effects on the transmitted signal, (1) group delay and carrier phase advance and (2) scintillation. Frequency dispersion causes the group velocity to differ from the carrier phase velocity. The magnitudes of the group delay and phase advance are the same, except that they are opposite in sign. Group delay is caused by interaction with free electrons in the ionosphere as the electromagnetic signals transmitted from the satellite propagate. Free electrons are caused by solar radiation exciting the outer electrons of atmospheric particles. Thus, the amount of interaction with free electrons is dependent on the time of day, solar activity, the elevation angle of the observation, and latitude. Group propagation delays can be represented analytically by the equation below.

$$\tau = \frac{\rho}{c} + \frac{A}{f^2} + \frac{B}{f^3} + \dots \quad 2.13$$

Where τ is the travel time, ρ is the pseudorange, c is the speed of light, A is a constant, B is proportionate to the average magnetic field strength, and f is the frequency of the propagating signal (e.g. L1 or L2 at 1575.4 MHz and 1227.6 MHz respectively). Most of the ionospheric delay is represented in the second order term A/f^2 and is negligible after the third order term B/f^3 . Having both the L1 and the L2 carrier

frequency allows for accurate calculation of the ionosphere delay based on the difference in arrival times of the L1 and L2 frequency waves. Restricting attention to the first and second order terms, we can difference the group delay ($\Delta\tau$) for L1 (f_1) and L2 (f_2) in the following way (where subscripts correspond to the associated carrier phase, L1 or L2).

$$\Delta\tau \approx A\left(\frac{1}{f_2^2} - \frac{1}{f_1^2}\right) \quad 2.14$$

$$\Delta\tau = \frac{A}{f_1^2} \left(\frac{f_1^2}{f_2^2} - 1\right) \quad 2.15$$

$$\Delta\tau = \tau_1 \left[\left(\frac{f_1}{f_2}\right)^2 - 1\right] \quad 2.16$$

Equations 2.13 through 2.16 describe the process for eliminating the majority of the ionospheric delay for the carrier frequency. This can be similarly applied to the carrier phase observables.

Scintillation causes the received signal phase and amplitude to fluctuate rapidly as it is received. These fluctuations are due to variations in the composition of the atmosphere causing refraction and diffraction of the signal. This can make it difficult for receiver to track and keep a lock on a satellite signal. Scintillation is more prominent at low latitudes, and from one hour after sunset to midnight local time. These effects are minimized from April to August in equatorial Americas, Africa and India, and from September to March they are minimized in the equatorial Pacific. When completing a campaign occupation of a GPS network, these effects should be considered.

2.1.4.3.2 Neutral Atmosphere

The neutral atmosphere is comprised of the troposphere, tropopause, and mesosphere, and is a non-dispersive medium. The troposphere alone accounts for approximately seventy-five percent of the delay, because it is the only place that water vapor exists; thus this will be the focus of this section.

When a signal propagates through the troposphere, the ray path is bent. This causes deviation from the predicted travel time (based on travel time in a vacuum). The total atmospheric delay (τ_{atm}) is described mathematically as the difference between the actual travel time and the estimated travel time in a vacuum (whose value is 1). This gives:

$$\tau_{atm} = \int_{atm} n(s)ds - \int_{vac} ds \quad 2.17$$

Where $n(s)$ is the index of refraction at a point s along the ray path. In order to predict this index of refraction at any point s , it is necessary to have an atmospheric model. Path delay effects are different for a wet and dry atmosphere. In a dry atmosphere, where all molecules are in hydrostatic equilibrium, at sea level, the zenith (elevation angle, $\theta = 90^\circ$) delay is 200-230 cm. For wet atmosphere, where water vapor exists, the delay is ~3-30cm. For decreasing elevation angle the delay increases based on $1/\sin(\theta)$.

It is very difficult to predict the distribution of water in the atmosphere. It would be much like trying to pinpoint a cloud from a windowless room. Aside from the amount of water vapor in the atmosphere, estimating the total tropospheric delay $p(\theta)$ must also takes into account the height of the atmosphere, the vertical distribution of particles, Earth curvature and ray bending. The culmination of this can be written as:

$$P(\theta) = p_d^0 M_d(\theta) + p_w^0 M_w(\theta) \quad 2.18$$

Where p^0 is the path delay at zenith, d and w denote dry and wet atmosphere respectively, and $M(\theta)$ is a mapping function that take all additional components of the delay into account at the given elevation angle.

The dry zenith delay p_d^0 can be estimated in two ways. The first, and most accurate approach is to measure surface pressure at the station during data collection. If this information is not available, it is possible to make a first order approximation of the surface pressure (P) using the estimated (or measured) elevation of the GPS site h and a scaling factor H (usually 7 km).

$$P = 1.013e^{-h/H} \quad 2.19$$

The wet zenith delay, p_w^0 , can be estimated in at least three ways:

1. Measurement of surface temperature and relative humidity applied to a simple atmospheric model.
2. Using a water vapor radiometer to measure atmospheric black body radiation in the microwave region, exploiting the rotational molecular transition of water near 22.2 GHz.
3. Stochastic estimation techniques, utilizing the strength of the GPS data and the accepted elevation angle dependence of the wet path delay.

Despite these estimation techniques, the wet atmosphere delay plays a large part in the uncertainty of position solutions. These uncertainties most largely impact stations in the tropics where water vapor content is high and quite variable, and is most prominent in the vertical component of the position estimate.

It is also possible to estimate the wet and dry delay simultaneously given that above $10\text{-}15^\circ$ the mapping function for wet and dry atmosphere are markedly similar. Since users usually use an elevation mask of $10\text{-}15^\circ$ to reduce the effects of multipath (described in the next section), this seems to be an applicable approximation.

2.1.4.4 Multipath Uncertainties

Multipath occurs when the signal transmitted by the GPS satellite interacts with another surface before reaching the GPS receiver antenna (Figure 2.1). Signal interaction not only causes the travel time of the ray path to be longer than predicted, but also alters the phase and pseudorange observables with time dependent sinusoidal signals based on the reflection geometry of the interaction. The magnitude of the multipath uncertainty is, to a first order, proportional to the wavelength of the signal. Consequently, multipath uncertainty will be greater for P-code estimated pseudoranges than for carrier phase estimated pseudoranges.

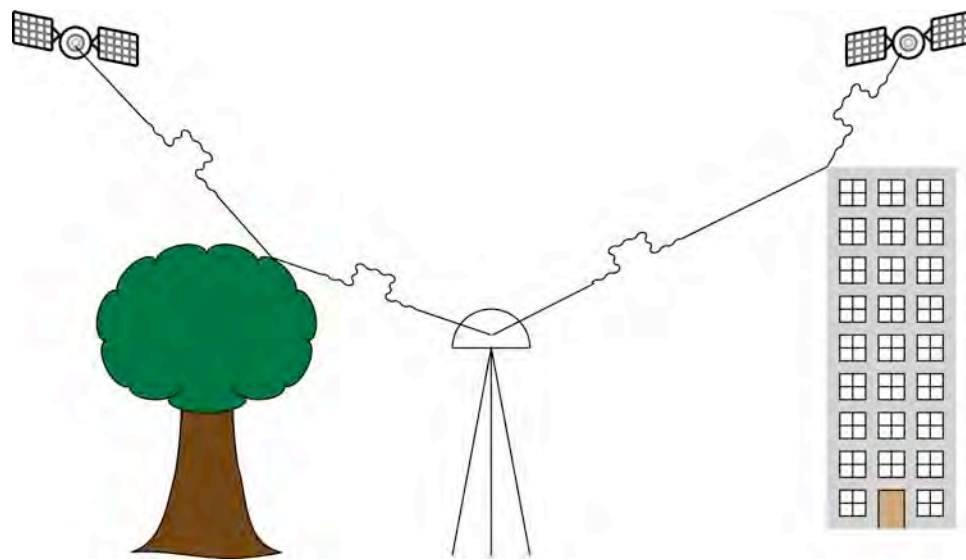


Figure 2.1. Cartoon representing multipath interaction of GPS satellites signals with other objects before reaching the GPS antenna

Due to the geometry of the omni-directional antennas used in geodetic GPS studies, it is necessary to mitigate these effects. Omni-directional antennas do not need to be pointed; they have the ability to receive signals from many satellites in any unobstructed direction all at once.

One way that multipath effects can be avoided is to set the mask of the antenna to at least 15° based on the angle of the horizon as seen by the antenna. The mask essentially blinds the antenna to any signal coming from below (bouncing off the ground) or interacting first with any other object on the ground (e.g. trees, fences, monument reinforcements) before reaching the antenna. In addition, this cutoff angle minimizes those 3rd and higher order terms in the atmospheric uncertainty (equation 2.13).

2.1.4.5 User Errors

There are several ways that the user can limit the accuracy of a GPS station position. Being unfamiliar with the setup procedure of the receiver antenna pair can cause processing difficulties later or the necessary input requirements of the given GPS receiver. Errors of this nature can be remedied by improved field methods, discussed in section 2.1.5 or in the preprocessing stages once the data has been downloaded from the receiver, discussed in section 2.1.6

2.1.5 Field Methods

The geometry of the GPS receiver network and the engineering of the monument itself can help in reducing noise sources for optimal position estimates. This section will explain the standard operating procedures for GPS networks and monuments installed by

the Geodesy Lab at the University of Miami – RSMAS and for the practical purposes of the data presented in this thesis.

2.1.5.1 Network Geometry

A sufficiently dense network will allow for the reduction of carrier phase ambiguities. To optimize ambiguity resolution, it is recommended that the minimum distance between stations is not larger than 100 km.

2.1.5.2 Continuous GPS Sites

There are two major types of GPS monument, continuous and campaign. Continuous GPS (CGPS) sites are built and remain in place for up to 10-15 years, continuously occupied by an antenna and receiver pair. There are several facets of a permanent monument that are required for optimum precision. The first of these is an anchoring mechanism for the antenna to maintain stability of the point whose position is being estimated. The most effective way to do this is to drill into bedrock, sink a threaded pole into the hole and fasten it to the bedrock so that it is coupled to earth motions. Anchoring a monument to bedrock is also important to minimize random walk noise due to phenomenon such as fluctuating soil moisture. In some cases where there is no access to bedrock, tops of small buildings or vaults can be used, preferably corners for increased stability. Other stable platforms can be conceived of as well.

Choosing a location with good sky visibility, away from terrestrial noise sources such as cars and pedestrian traffic is also important. It is imperative to install a GPS station in an area with minimal amount of horizon obstructions so that the antenna can

have view of as many satellites as possible. Also, installation close to its mounting surface and far from any reflective surfaces (e.g. cars, houses) or vertical protrusions (e.g. poles, power lines, telephone poles, trees) will minimize multipath uncertainties. Power for the receiver can either be pulled directly from an AC/DC outlet (if there is a power source near by), or from car batteries set up in serial. Increased longevity can be attained if solar panels are installed to recharge the batteries periodically.

Protection for these power sources as well as the receiver its self is very important. This can be in the form an in-ground vault or in an above ground metal enclosure with a door that locks. The important features for the enclosure are that wires can pass in and out of it (preferably through buried conduit), that it be relatively water, wind, sun and lightening proof. If the vault is below ground, it is better to have the walls of the vault lined with plastic or cement to keep soil moisture away from electronic components.

The last thing that is imperative for a good CGPS station is easy access for data collection, to prevent data loss. This can be achieved by locating the station in a place that is easily accessed in person, by car and/or short hike, or by installing a telemetry system to transmit the data to the user periodically or continuously.

Once the monument is built and the antenna and receiver are installed, the user must measure the precise height of the antenna, as this will be necessary for processing of the data. Specific configurations of the CGPS network stations on the Nicoya Peninsula, Costa Rica used for this thesis will be explained in section 3.3 and Appendix A.

2.1.5.3 Campaign GPS Sites

In some areas permanent stations are not a plausible option due to cost of equipment, availability of resources, data collection capabilities, battery life, etc. In this case, campaign GPS (cGPS) monuments are used. The components of a cGPS site are not much different than those of the CGPS station. Coupling to bedrock, stability of station, power for the receiver, distance from anthropogenic noise, good visibility of the sky and access are all still very important for campaign stations. The only difference is that the user only occupies a cGPS station for a matter of days, once every year to two. Therefore, the longevity of the monument itself (the point that is coupled to the bedrock) is very important, but the station supporting the antenna and receiver must be portable yet stable.

For these purposes the UM Geodesy lab has engineered a system for building a cGPS station. When bedrock is found a hole is drilled, filled with epoxy and a 9/16" stainless steel pin is inserted in the hole. Each pin is denoted by a number that is recorded, along with the precise latitude, longitude and elevation of the point. A small dimple is machined into the top of the pin to ensure that the same point is occupied on every return visit.

During an occupation a spike mount is assembled above the pin. Spike mounts are a tripod configuration with a center rod to be inserted into the dimple in the monument pin (Figure 2.2). A plumb bob tip is screwed into the base of the center rod to create a sharp intersection between the spike mount and dimple in the monument pin. The top of the center rod is equipped with threads to be screwed directly into the base of the antenna. Currently, any campaign occupation done by the UM geodesy lab uses

Zephyr Geodetic antennas. The center rod is machined to be exactly .500m from tip to threads.



Figure 2.2. Representative pictures from a GPS campaign showing the monument pin and a spike mount set up with a Zephyr Geodetic antenna with ground plane.

There are fine and course adjustment knobs on each leg of the spike mount as well as a plate that is machined flat for proper leveling. Once the entire system is level, weights are placed on the horizontal arms and the legs are epoxied into place for stability. With minimal amount of preparation, these stations can be converted to CGPS stations, given the proper availability of receivers and antennas.

2.1.6 GPS Data Processing

All data processing done by the University of Miami RSMAS Geodesy lab uses the GPS-Inferred Positioning System and Orbit Analysis Simulation Version 4.04 (GIPSY-OASIS) software package, hereafter referred to as GIPSY, using the precise point positioning method. The methods specifically employed by the geodesy lab and this software will be the focus of this section.

2.1.6.1 Preprocessing GPS Data

Most data being downloaded directly from a geodetic GPS receiver, termed raw data, are not compatible with the input format required by GIPSY. In addition they may have user error embedded in the data file caused by imprudent set up procedures (such as files created every hour instead of every day). Fortunately there are computing scripts publically available to deal with this incompatibility from UNAVCO and the National Geodetic Survey. UNAVCO is a not for profit organization that archives GPS data, loans equipment and man power to universities and investigators who are members of the organization, and provides processing and editing computer scripts for data processing. More information can be found at: <http://facility.unavco.org>.

GPS receivers output data in a binary form, while GIPSY reads in data in the Receiver Independent Exchange (RINEX) format, which is an ASCII conversion of the binary data. This can be done with a single computing command and if receiver and user information is known, this can be imbedded into the conversion for more accurate results. The final RINEX file contains a header that records user information including the name of the person and organization that occupied the station, the type of receiver, the type of antenna, the initial position estimate of the monument, the start and end time of observations for that file, and the sampling interval (which is defined by the user).

There are certain aspects of a RINEX file that must be formatted correctly in order for GIPSY to properly process the data. Most deviations from this form can be amended using a program called Translate Edit Quality Control (TEQC). GIPSY requires that the RINEX file be no more than 24 hours long. This 24 hour window is based on 00:00 to 23:59 Greenwich Mean Time (GMT). If the file contains more than 24

hours of data, TEQC will splice the file. The file fragment can then be concatenated to the beginning or end of the proper days file. Conversely the concatenation commands can also piece together more than one file for the same day if they exist. Other amendments that can be made by TEQC include ensuring that the proper day of year is recorded in the header file for the day that the data was collected. The +qc (quality check) command provides diagnostics of the receiver including clock drift information.

2.1.6.2 Processing with GIPSY-OASIS 2.2

Once the RINEX files have been quality checked and edited for compatibility they are pared down to include only the data used by GIPSY so that only signals from L1, L2, P1, P2 and C/A1 remain. The first code run by GIPSY is “clock prep”, which fixes any clock biases as described in sections 2.1.3 and 2.1.4.1. Subsequently, “ninja” reads in the RINEX file, edits and decimates it. This is outputted to a Quick Measurement file, denoted by a .qm file extension. Corrections for outliers, cycle slips, clock instability and troposphere conditions are done using TurboEdit [Blewitt, 1990]. Further troposphere corrections are implemented using Ambizap [Blewitt, 2008]. More on the mechanism of these corrections is explained in section 2.1.6.3.

Raw GPS positions are calculated relative to the center of mass of the earth. A reference network of at least three stations is required for point positioning. The University of Miami operates and processes data for 100 stations globally that are used as a reference network. All calculated positions are calculated relative to this network. At this stage of processing each station now has a calculated position for each day that the

site was occupied. These positions are divided into North, East and Vertical components and plotted against time, giving a time series of positions for each GPS station.

2.1.6.3 Ambiguity Resolution

The use of the L1 and L2 phase data to calculate pseudorange has inherent ambiguities associated with it, particularly ambiguity in the number of carrier phase cycle ambiguities. However, there are computing routines that can resolve these ambiguities. Geoff Blewitt has done extensive research on this subject to create optimal processing routines; this section will be a summary of his work (e.g. [Blewitt, 1989; 2008]).

Due to the north-south ground path of the GPS satellites, carrier phase biases in the east component of the GPS position calculation are greater than those in the north component. Some of the bias associated with phase data can be corrected by processing the phase data together with pseudorange data, however, uncertainties still exist that can be improved upon. After initial double differencing, explained above, carrier phase cycle ambiguities are biased by an integer number of cycles. There are several ways to resolve these integer ambiguities.

1. Simultaneously solve parameters for stations in close proximity to each other.

If two GPS receivers are operating within several hundred kilometers of each other (though <100km is optimal for millimeter precision of geodetic GPS), at the same time, many of the errors inherent in the GPS position estimate are common to both locations (e.g. satellite clock time errors, some satellite ephemeris parameters, ionospheric delays, etc.). These are known as common mode errors. A correction for

common mode errors is done as a processing step, once the precise point positions are calculated for each station, allowing the use of all data points for a given receiver without eliminating outliers or unpaired data between receivers when differencing.

2. Use the ionospheric group delay of the P code, which is equal and opposite to the phase delay, given that the correct number of cycles is related to the phase measurement.

The most effective way to resolve carrier phase includes the use of both L1 and L2 carrier phase data as well as the P1 and P2 carrier wave modulations and is independent of *a priori* ionosphere corrections.

3. Solve ambiguities using “wide lane” ambiguities, where

$$\lambda_w = c/(f_1 - f_2) \approx 86.2 \text{ cm.}$$

Wide lane ambiguities are calculated by differencing the phase bias between two receivers. This bias can then be solved by double differencing linear combination of the carrier phase data and the linear combination of the pseudorange data. Resolution of these cycle ambiguities is most important when calculating baselines and an automated method can exploit varying baseline lengths in a network to resolve these ambiguities.

2.1.6.4 Network Baseline Calculation

In some cases where all network stations are within 150 km of each other, it is possible that not all common mode errors have been sufficiently reduced after ambiguity resolution has been applied as described above. In this case it is sometimes useful to calculate baselines from each network station to another reference station some 100 – 500 km away from the entire network. This baseline calculation is done as a post-processing

step after positions have been calculated and averaged to daily solutions. Essentially a daily position from the network station is subtracted from the daily position of the reference station and regional common mode errors are reduced. The output time series are then reporting positions relative to this reference station instead of the 100 site global network.

2.1.6.5 Post-processing of GPS Data

Once time series have been created for each station the path of motion must be analyzed by fitting data to model. The simplest model first assumes uniform motion and applies a linear fit to the GPS data. The slope of this line is the rate of motion of the site and is calculated for each component (north, east and vertical) independently. The weighted root mean squared error (wrms) is then calculated to determine the deviation of the data from this straight line. Deviations from uniform motion can either be due to geologic processes such as earthquakes, volcanic activity, landslides or other transient events, or from human activity, such as antenna changes or ground water withdrawal. If any antenna changes are present during the time of the occupation, this is accounted for, as well as any earthquake offsets, by applying an offset to the linear fit at the time of the event. Processes that cause deviations from uniform motion can be the signal that the investigator is attempting to understand. The method used to fit models to these types of signals will be described as applicable in subsequent chapters.

2.2 Modeling

One goal of geodetic studies is to understand the “what, when and how” of geologic deformation processes. The processed data tells us when and how much deformation occurred. Once the data has been processed, site velocities or displacements have been calculated, and the motion of the network stations has been described, it is necessary to build and test geologically realistic models to better understand the geologic process. This section is dedicated to a description of geologic models relevant to the studies developed in this thesis.

2.2.1 Inverse Theory

To a first approximation an inverse model assumes that you know something about the process that is behind the deformation observed in a given data set and how to mathematically represent it. Specific parameters defining that process can be determined (e.g. there was an earthquake on a fault plane but you do not know where the fault plane ruptured or by how much). Inverse modeling programs use data to search for the parameters of that model that are most consistent with the data. The most general form of the inverse equation is given by:

$$d=A(m) \quad 2.20$$

where a vector of model parameters m is acted upon by an operator A that is a set of mathematical function representing the physical process that has occurred. The interaction of these two gives rise to the observable d . Modeling is an iterative technique where the data predicted d_p by the starting model m^0 are compared to the data observed d_o . Changes are made to the model parameters (Δm) in a systematic way defined by the

user, to find the model parameters that provide the best fit to the data. The equations that govern these processes are as follows:

$$m = m^0 + \Delta m \quad 2.21$$

After making the problem linear, equation 2.20 becomes:

$$\Delta d = A \Delta m \quad 2.22$$

where Δd is the difference between the observed and predicted data and A , also known as the data kernel, represents a partial derivative matrix:

$$A = \frac{\partial d}{\partial m} \quad 2.23$$

The objective of an inverse model is to find the appropriate Δm such that when multiplied by the partial derivative matrix, returns the required Δd . This is considered to be the “best fitting model” and is defined by the model parameters producing a predicted data set with the lowest misfit to the observed data (minimizing Δd).

Inversion techniques are useful for several reasons, not the least of which is that many parameters can be solved for at once. This can become very cumbersome in a forward model since large numbers of parameter combinations have to be tried to find the best fit. One problem with inverse modeling is that there is often no “unique” solution due to uncertainties in the data. This is why it is important to have the most accurate GPS data, reducing as much ambiguity as possible. The governing equation of a model (A) is a mathematical simplification of a real condition and thus no model will exactly match the data. Furthermore it is possible that there will be several models that fit the data equally well. Thus, it is important to have a grasp of the geologic system being modeled and *a priori* information to determine which of the best-fit models is preferred.

There are many types of inverse models. This section will focus on two specific types of inverse models that were used to support the studies of this thesis, Dislocation Models and Block Models.

2.2.2 Dislocation Modeling

Beginning in the late 1950's, earthquakes have been modeled as a rupture on a rectangular dislocation plane in an isotropic, semi-infinite, elastic medium [*Rongved and Frasier, 1958; Steketee, 1958*]. These models have become known as Elastic Half-Space Dislocation Models. Slow slip events, like earthquakes, are mechanisms of strain release for the area of the fault plane on which they rupture, with motion in the opposite direction of interseismic strain accumulation. It follows that the modeling methods used for earthquakes can be used for slow slip events. Despite the fact that there is a time component to slow slip events that does not exist for earthquakes, dislocation models are an appropriate approximation for events with durations on the order of weeks. As more and higher quality data are acquired, it will be appropriate to investigate more sophisticated variable slip models.

Elastic Half-Space Models begin with the definition of the isotropic, semi-infinite medium. The modeled space begins at the earth's surface and continues downward to infinity. The material composition of the medium is defined by lamé parameters λ and μ . These parameters describe the elastic behavior of the medium being modeled under compression, tension and shear. Steketee (1958) show that when a finite rectangular plane Σ is defined within this medium and a dislocation $\Delta u_f(\xi_1, \xi_2, \xi_3)$ is applied, the displacement field $u_f(x_1, x_2, x_3)$ can be calculated by solving the following integral.

$$u_i = \frac{1}{F} \int \int_{\Sigma} \Delta u_j \left[\lambda \delta_{jk} \frac{\partial u_i^n}{\partial \xi_n} + \mu \left(\frac{\partial u_i^j}{\partial \xi_k} + \frac{\partial u_i^k}{\partial \xi_j} \right) \right] v_k d\Sigma \quad 2.24$$

Okada [1985] outlines the formulas that govern elastic half-space dislocation models as applied to each type of faulting (strike slip, normal, and thrust) to predict resulting surface displacements.

2.2.2.1 Slipinv

The general principles of dislocation modeling described above are applied in the *slipinv* inversion code written in MATLAB by Gareth Funning [*Funning et al.*, 2005]. This code applies the formulas defined by *Okada* [1985], using inverse theory to produce a model which provides acceptable solutions for a variety of tectonic problems. This program is compatible with many different types of deformation data, including GPS and InSAR.

Slipinv has the ability to either solve for, or use constraints for, any given parameter. Fault parameters such as strike, dip, rake, length and depth are non-linearly related to the dislocation field [*Okada*, 1985]. It is possible to complete a non-linear inversion that solves for the most probable fault geometry. Using a non-linear inversion would quickly increase the number of free parameters, which must be low relative to the number of data points to produce a robust solution. If *a priori* information is available concerning the fault parameters, it is also possible to fix these values in the model. This is beneficial for faults with complex geometries where additional information is available. Faults with strike or dip changes are modeled using multiple rectangular dislocations that are treated as conjoining planes.

Strain release events may not rupture the entire fault plane, nor do they break the entire rupture area uniformly [Dmowska *et al.*, 1996; Ji *et al.*, 2002; Kanamori and Kikuchi, 1993; Subarya *et al.*, 2006; Thatcher, 1990; Yamanaka and Kikuchi, 2004]. In cases with a broad enough data distribution and a large enough rupture area, this non-uniform slip distribution can be identified. This is modeled using distributed slip by dividing the dislocation plane into smaller pixels defined by the user.

Unlike other fault parameters, slip on the fault plane is linearly related to the dislocation field, which allows a more straightforward linear inversion following equation 2.22. In this formulation, a forward model initially forms matrix A where 1 m of slip is imposed on each fault pixel using Okada's [1985] equations. Matrix A is used to create a series of Green's functions that provide a starting point for the model, and describe the relationship between slip on the fault plane and the surface displacement field, for a given starting model parameters, m^0 . The vector m is adjusted by Δm based on the comparison between calculated and observed surface displacement and is ultimately determined by non-negative least squares methods. The least squares method relies on finding estimated model parameters (m^{est}) that minimizes the Euclidean distance L , or the difference between the $d^{observed}$ and the $d^{predicted}$.

$$m^{est} = [A^T A]^{-1} A^T d \quad 2.25$$

Slipinv uses a root mean square (rms) formulation to estimate the $d^{observed} - d^{predicted}$.

$$L_{rms} = \sqrt{\frac{1}{N} \sum (d^{observed} - d^{predicted})^2} \quad 2.26$$

In distributed slip models with a relatively large number of free parameters, model instabilities are common. This implies unrealistic, high strain gradients between

pixels [Funning, 2005]. To ensure that physically plausible solutions are reached, smoothing can be applied, constraining the amount of variation in slip between dislocation pixels. Laplacian smoothing is one method used by *slipinv*, utilizing the second spatial derivative (gradient) for each pixel, minimizing the sum of its value over the dislocations, thus minimizing the gradient between pixels.

$$\nabla^2 m \cong Sm \quad 2.27$$

where S is a matrix composed of smoothing vectors for each pixel and ∇^2 is the Laplacian operator.

There is a scaling factor k that is imposed on this relationship to align the model with physical probability and *a priori* information. The appropriate value of k is chosen using *a priori* information of the physical properties of the system, and to balance the L_{rms} with the ‘solution roughness’ ρ [Jonsson *et al.*, 2002]. The final matrix representation of these calculations is described by Biggs [2007].

$$\begin{pmatrix} A \\ k\nabla^2 \end{pmatrix} (m) = \begin{pmatrix} d \\ 0 \end{pmatrix} \quad 2.28$$

There is a trade off between resolution and stability of the model. At a minimum, resolution of the model cannot exceed the spatial density of data points. For example if a network of GPS stations are never less than 25 km apart, we cannot detect motion or deformation in the model at spatial wavelengths shorter than 25 km. Resolution tests are done to confirm if the data and model geometry are able to robustly determine a given result. These resolution results are unique to a specific value of k , and can be calculated for each pixel in the down dip and along strike direction independently. I calculate model resolution for *slipinv* models following Biggs [2007], where 1 m of slip is imposed on a single pixel, for which the surface displacements are calculated at each observation point.

These estimated surface displacement are then inverted to determine the inferred pattern of slip, which is compared to the known input of 1 m of slip on one pixel. This process is repeated for each pixel and summed. The resolution length scale for each pixel is then defined as the total dimensions of the pixels in the horizontal and vertical directions for which the value in the resolution matrix is greater than $1/e$ of the maximum [Biggs, 2007]. It may be possible to resolve a slip distribution with more detail than is realistic, therefore *a priori* information is an important tool.

The elastic half-space inversion code [Funning *et al.*, 2005] based on the formulation of Okada [1985] accounts for complex fault geometry. There can either be positive dislocations (where there is slip) or “negative” dislocations with back slip, to simulate locking [Savage, 1983], making it a good choice for modeling the Costa Rican subduction zone. This modeling will include both coseismic and interseismic motions.

2.2.2.2 Back Slip Modeling

There are two end members of tectonic motion, stick-slip motion and creep. Creep is the continuous movement between two plates or blocks. Stick-slip motion is the type of motion that produces earthquakes. In this case there is sufficient friction to fuse the two sides of a fault together, resulting in strain accumulation, until friction is overcome, causing them to break apart during an earthquake. It is possible that both of these processes can occur on different parts of one fault at the same time. In a subduction zone, the upper fault zone is locked between earthquakes, during the interseismic, while the lower fault zone is freely slipping, presumably at full plate convergence rate. This produces strain accumulation that is measurable by GPS. Modeling of the interseismic

portion of the seismic cycle requires simultaneously representing both of these processes to find the resulting deformation pattern.

Savage [1983] describes the theory behind back slip modeling, one approach to modeling strain accumulation on subduction zones. Stick-slip motion is considered to be a perturbation of steady state sliding, or creep, over the entire fault plane. It follows that this would be the starting model (Figure 2.3, top panel) to which perturbations are applied. When modeling interseismic strain accumulation, we are only interested in the signal resulting from the “sticking” of the fault plane. This can be simulated by applying back slip, or opposite sense of motion to the upper fault zone. As stated, slip on a fault plane is linearly related to the deformation pattern at the surface. Thus, multiple slip processes can be combined by simple addition. When these two processes are added together, the result is locking on the upper fault plane (e.g. thrust motion + equal normal motion = zero motion) and thrust motion on the lower fault plane (e.g. thrust motion + zero motion = thrust motion). The predicted surface deformation field can then be calculated. A graphic description is shown in Figure 2.3.

2.2.2.3 Block Modeling: DEFNODE

Block modeling is a three-dimensional approach, approximating the size and shape of tectonic plates, blocks and micro-plates, and inverting for rotation poles and the strain accumulation between neighboring plates or blocks. The model is a boundary element type, built from the ground up using node placement much like a finite element model with the exception that the mesh is limited to the outlines of the blocks and faults

and by definition does not include interior deformation parameters other than elastic strain. Motion or coupling is calculated or imposed on the fault nodes to drive the model.

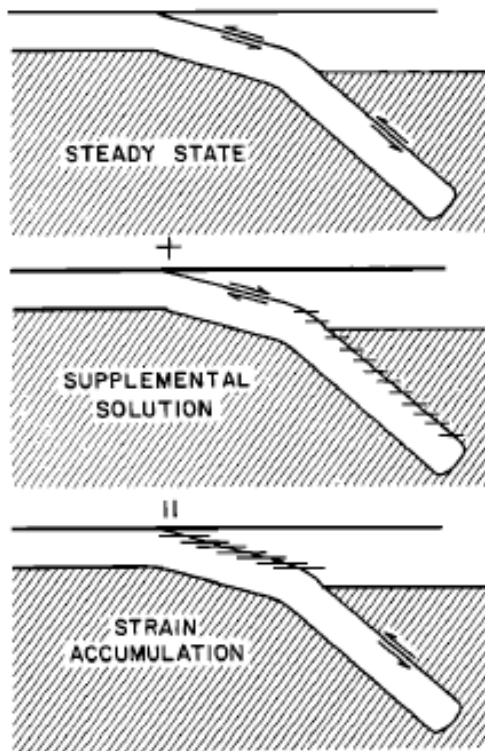


Figure 2.3. Superposition model of strain accumulation at a subduction zone from [Savage, 1983]. The asthenosphere is indicated by shading. A locked (no slip) condition at an interface is indicated by short horizontal bars crossing the interface.

The particular block modeling program used here is DEFNODE [McCaffrey, 2002; 2006]. This program models not only lithospheric block rotations and strains but also, interseismic locking or coseismic slip on block-bounding faults. Models are run in a Cartesian coordinate system but can convert to and from a spherical coordinate system (latitude and longitude) as needed.

Like *slipinv*, DEFNODE uses the formulas of Okada [1985] to calculate the displacement field resulting from a dislocation in an elastic half-space. In this case the dislocation is integrated over a finite space between nodes. The program employs

simultaneous inversion for block rotation and strain accumulation and uses a simulated annealing algorithm over multiple iterations to arrive at the best-fit solution.

Simulated annealing is a term borrowed from metallurgy, where the heating and controlled cooling processes are repeated to work out any impurities in the metal. The same concept is applied to the modeling field to find the global minimum, or model and parameter set with the lowest misfit to the data. This requires an iterative modeling routine, where, when a solution is found, the model is run again with different starting parameters close to the solution parameters. The model runs, stepping downward in the parameter space, looking for the best fit based on those starting parameters. This process is repeated until a satisfactory solution is reached, determined by successive best fitting models that are no longer statistically different from each other. The advantage of this method is that it avoids solutions that are merely local minima and not a global best fitting model. This process was originally described in detail by *Kirkpatrick et al.* [1983] and *Cerny* [1985].

In addition to GPS data, DEFNODE can include earthquake slip vectors, geologic slip rates on faults, surface uplift data, spreading rates, rotation rates, transform azimuths, surface strain rates and surface tilt rates [*McCaffrey, 2006*]. Surface deformation from motion on the block bounding faults is calculated using Green's Functions based on the node geometry and input constraints of the model. This is done much the same way as described for the *slipinv* program. A forward model is run applying a unit velocity or offset at each node. The resulting surface deformation field is calculated. From the resulting surface deformation field, response functions are designed and used to govern the model communication between fault motion and surface deformation. The observed

GPS values are decomposed into V_x and V_y horizontal components. V_x and V_y are used to estimate the velocity gradient tensor G by weighted least squares methods. In terms of the observed velocity field G is equal to:

$$G = \begin{pmatrix} \partial V_x / \partial x & \partial V_x / \partial y \\ \partial V_y / \partial x & \partial V_y / \partial y \end{pmatrix} \quad 2.29$$

In addition the velocity gradient tensor is the sum of the strain rate $\dot{\epsilon}$ and the rotation rate vector θ :

$$G = \dot{\epsilon} + \theta \quad 2.30$$

The fit of data to model is calculated by a reduced Chi Square (χ_r^2) formula.

$$\chi_r^2 = \frac{1}{n-p} \sum_{i=1,n} \left(\frac{obs_i - pred_i}{\sigma_i} \right)^2 \quad 2.31$$

In this formula n is the number of observations, p is the number of free parameters and σ is the uncertainty of the i^{th} data point.

The amount and distribution of coupling between blocks can be an input constraint or estimated from the data. In either case this value ϕ is a measure of the fractional part of the fault plane involved in the stick-slip style of motion, that is “stuck” under the modeled stress conditions. Plate locking is then defined as $\phi_i V_i$ at node i where V is the convergence vector between two plates and is estimated by bilinear interpolation between the four enclosing nodes [McCaffrey *et al.*, 2000].

The first way to restrict coupling is to define areas to be fully coupled or freely slipping by setting $\phi=1$ or $\phi=0$ respectively, where it is geologically reasonable (e.g. where faults would be freely slipping at depths > 50 km). If the value of ϕ is an estimated parameter there are several ways to constrain the behavior of locking. It is also possible

to set groups of nodes that must behave in conjunction with each other (e.g. uniform locking from 0-10 km). In most subduction zone cases, it is accepted that locking decreases down dip. DEFNODE has means to describe this decrease and constrain it within the model in a couple different ways. The first approach to the coupling distribution is a linear decrease in coupling down dip. This forces the value of ϕ at any node to be less than or equal to the node directly up dip. Similarly, the coupling on the fault plane can be forced to obey a Gaussian distribution where the fault is freely slipping at the top and bottom and achieves maximum coupling in the middle. Lastly, it is also possible to allow the data and inversion to freely determine locking. A penalty function is applied to keep the value of ϕ between 0 and 1 and avoid reverse subduction or locking at rates higher than the plate convergence rate [McCaffrey, 2002].

The complexity and versatility of this modeling program allows for its use in large regions where a variety of data types are available and multiple outputs are desired (i.e. Euler vectors as well as strain accumulation on block bounding faults). DEFNODE also allows for oblique convergence in subduction zones by defining the motion of one block relative to a single reference block within the model, ideal for the Cocos-Caribbean case. Thus, if the Euler vector of the Cocos Plate relative to the Caribbean Plate is known, this is used as an input parameter to constrain the long-term motion and drive the model. For the purposes of this thesis, this model will be used to determine interseismic locking patterns, using a data set that accounts for the existence of TSEs.

CHAPTER 3

A Tremor and Slip Event on the Cocos-Caribbean Subduction zone as measured by a GPS and Seismic Network on the Nicoya Peninsula, Costa Rica

3.1 Overview

Episodic Tremor and Slip (ETS) events are repeated, slow movements on the subduction zone fault interface that are accompanied by seismic tremor. ETS events may reflect processes in the transition zone between locked and aseismically slipping portions of the subducting slab interface [Kato, 2003; Ito *et al.*, 2007; Schwartz and Rokosky, 2007]. The slip direction of the upper plate is opposite to plate motion, as in standard earthquakes (recovering strain accumulated since the last slip event) but the rate of slip is orders of magnitude slower than standard earthquakes. ETS events were first observed in the Cascadia subduction zone [Dragert *et al.*, 2001; Melbourne *et al.*, 2005; Brudzinski and Allen, 2007] and have since been identified in several other subduction zones including Japan [Hirose *et al.*, 1999; Ozawa *et al.*, 2001; Ozawa *et al.*, 2002; Igarashi *et al.*, 2003; Ozawa *et al.*, 2003; Ozawa *et al.*, 2004; Hirose and Obara, 2005; 2006; Ito *et al.*, 2007; Ozawa *et al.*, 2007], and Mexico [Lowry *et al.*, 2001; Kostoglodov *et al.*, 2003; Larson *et al.*, 2004; Franco *et al.*, 2005; Brudzinski *et al.*, 2007; Larson *et al.*, 2007;]. Other subduction zones, such as New Zealand, experience variations of this slow strain release process, where slip can occur on the up-dip portion of the fault plane, yet seismic tremor is absent [Douglas *et al.*, 2005; McCaffrey *et al.*, 2008].

Duration of the slip events can last for days or weeks, e.g. 6-15 days along the Cascadia subduction zone [Dragert *et al.*, 2001] or 2-5 days on the Nankai subduction zone in Japan [Ito *et al.*, 2007]. Despite the fact that these slip events are aseismic, they are accompanied by tremor-like seismic signals that originate from the same, or nearby

regions [*Kao et al.*, 2005; *Rogers and Dragert*, 2003; *Shelly et al.*, 2006; *Ito et al.*, 2007]. There is some evidence that these events also have a recurrence interval that may vary depending on region [*Miller et al.*, 2002; *Shelly et al.*, 2006; *Brudzinski and Allen*, 2007; *Dragert*, 2007]. Repeat times range from 14 months in central Cascadia [*Szeliga et al.*, 2008] to 6 years in the Bungo Channel Japan [*Ozawa et al.*, 2004; *Ozawa et al.*, 2007], and may in fact be random in some locations.

ETS events increase stress up-dip from the locus of maximum slip; this up-dip region is often the rupture zone for megathrust earthquakes [*Ito et al.*, 2007]. In addition, these events may have important cause and effect relationships with other processes occurring within the subduction zone. The physical mechanism for ETS events is still debated but tremor and slip generation may be related to high pore-fluid pressures created by dehydration reactions in subducted oceanic crust and sedimentary cover [*Shelly et al.*, 2006; *Ito et al.*, 2007], with possible temperature influences [*Peacock and Wang*, 1999; *Dragert et al.*, 2001; *Peacock et al.*, 2002]. The temperature profiles of the well studied relatively warm Japanese and Cascadian subduction zones contrast with the cooler Costa Rican system.

In this chapter, I describe a tremor and slip event detected in May 2007, the first well documented slow slip event along the Nicoya subduction zone, part of the Cocos-Caribbean plate boundary (Figure 3.1). This event was detected on a network of continuous GPS and seismic stations in northern Costa Rica, which were installed from 2005 – 2008 (Figure 3.2). At this point, it is not known if such events are episodic, though speculative evidence for such events has been presented by *Protti et al.* [2004] using three GPS stations and by *Brown et al.* [2005] using offshore fluid flow data.

Tremor did occur coincident with the geodetically observed 2007 slow slip event that I present here (Figure 3.3). For clarity, I refer to this as a tremor and slip event (TSE). I describe the available data constraints on location and duration of slip and tremor, and compare the locus of the 2007 TSE to past large plate boundary earthquakes in the region.

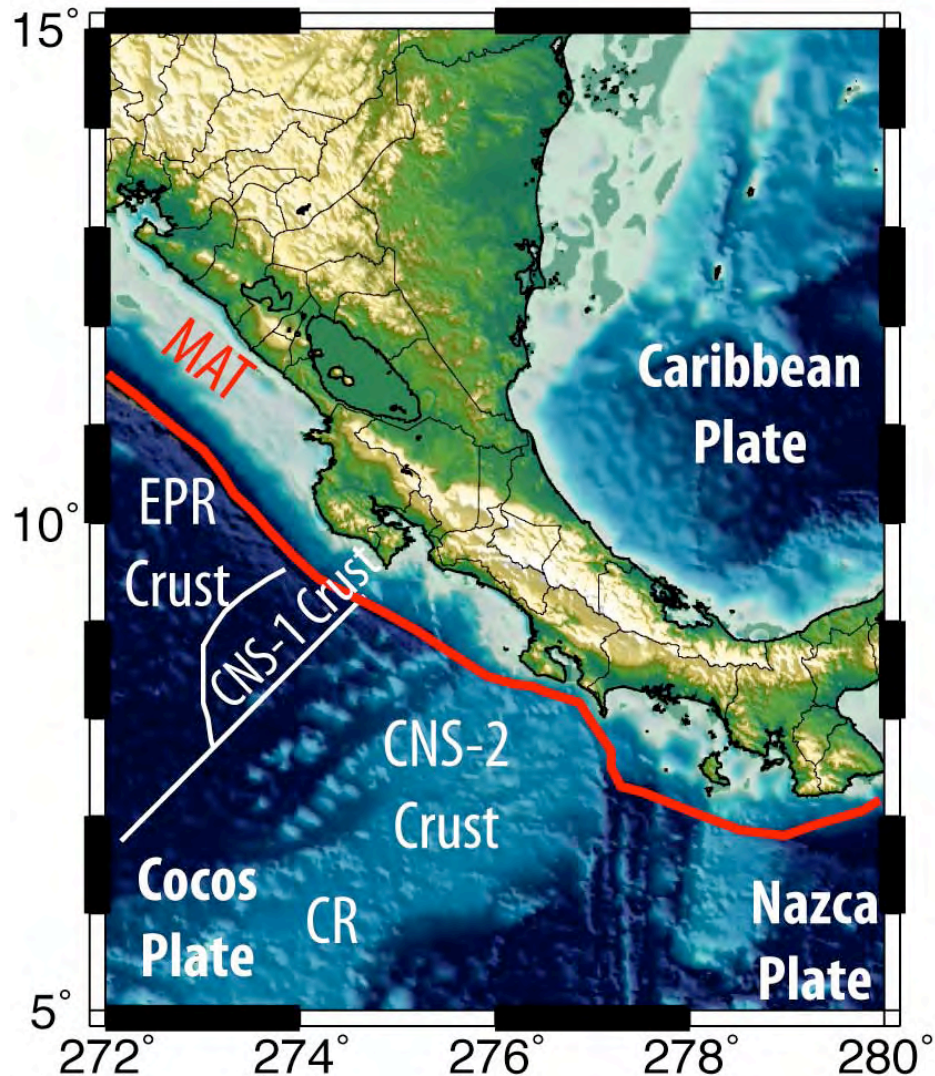


Figure 3.1. Regional map of Central America. Black box outlines study area. Map shows variation in oceanic crust origin and topographic relief. MAT is Middle America Trench. EPR is East Pacific Rise crust. CNS is Cocos-Nazca Spreading Center crust. CR is the Cocos Ridge.

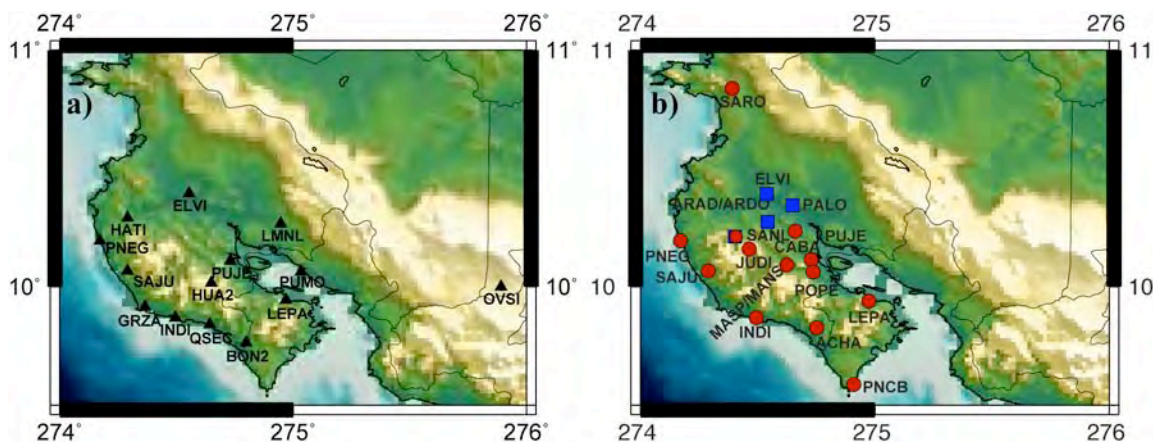


Figure 3.2. a) Configuration of CGPS (black triangles). Note SAJU was installed after the 2007 TSE. b) Configuration of seismometers; blue squares indicate 100m borehole seismic vaults, red circles indicate shallow (2-8m) surface seismic vaults. Note SAJU and ACHA were installed after the 2007 TSE.

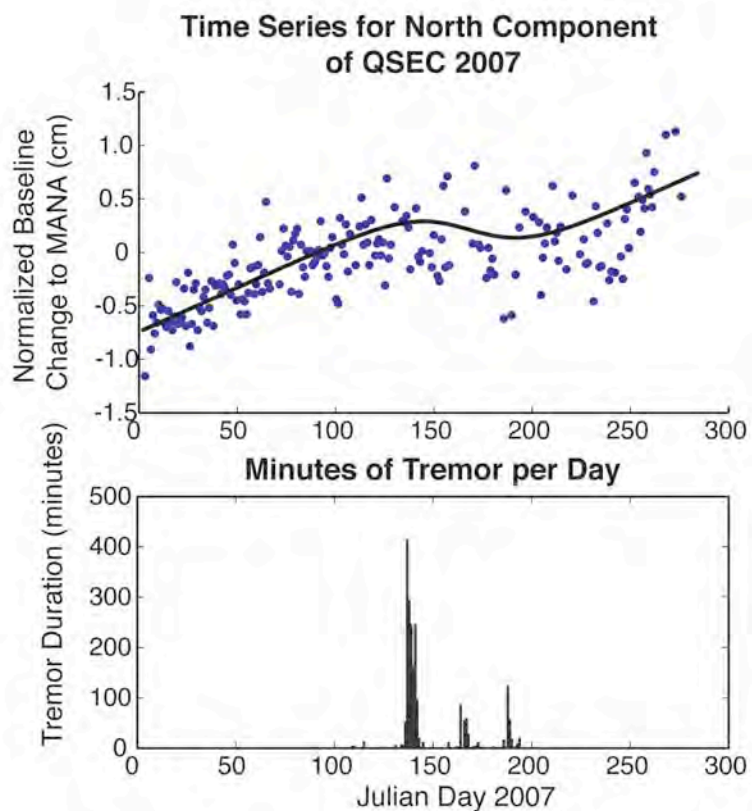


Figure 3.3. North component of displacement at station QSEC compared to a histogram of cumulative tremor duration per day. The onset and duration of the geodetically determined slow slip correlates well with peaks in the tremor time series.

3.2 Geologic Background

The Cocos and Caribbean plates are converging at high rates ($\sim 8\text{-}9$ cm/yr in Costa Rica) with varying amounts of obliquity [DeMets, 2001]. At the latitude of the Nicoya Peninsula (Figure 3.1), the convergence direction is $\sim 10^\circ$ counter-clockwise from the trench-normal direction [DeMets *et al.*, 1994; DeMets, 2001]. Along this segment of the Middle America Trench, between the North America-Cocos-Caribbean triple junction [Guzman-Speziale, 2001] and the central Costa Rican deformed belt [Marshall *et al.*, 2000], relative plate motion is partitioned. Subduction close to the trench-normal direction occurs at a rate of $74\text{-}84 \pm 5$ mm/yr, while northwest-directed arc-parallel shear occurs at rates between about 14 ± 4 mm/yr [DeMets, 2001] and 8 ± 3 mm/yr [Iinuma *et al.*, 2004; Norabuena *et al.*, 2004; LaFemina *et al.*, 2009], associated with northwest motion of a fore-arc “sliver block”, which includes the Nicoya Peninsula. The southeastern end of this block probably terminates in the central Costa Rica deformed belt [LaFemina *et al.*, 2009].

The Pacific coast of Costa Rica has two peninsulas, Nicoya to the north and Osa to the south, elongated in the northwest-southeast direction, parallel to the Cocos-Caribbean plate boundary. The close proximity of the Nicoya Peninsula to the trench, and its position directly over the seismogenic zone [Protti *et al.*, 2001; Newman *et al.*, 2002; DeShon *et al.*, 2003; Norabuena *et al.*, 2004; DeShon *et al.*, 2006], allows geodetic and seismic instrumentation to be placed close to the locus of strain accumulation and release making it a prime location to study seismic processes on a subduction zone plate boundary.

3.3 GPS and Seismic Network

Nicoya Peninsula currently has a network of 13 continuous GPS (CGPS) and 17 seismic stations designed to identify and characterize the pattern of TSE events along the seismogenic zone of northern Costa Rica's Pacific margin (Figure 3.2). The CGPS stations have varying equipment and communication capability, as summarized in Table 3.1. Pictures of the Monumentation styles can be found in Appendix A. Two sites are directly connected to the Internet through a router for direct access. These sites, LMNL, located in Limonal, and ELVI in Hacienda el Viejo, Filadelfia, are being monitored with Plate Boundary Observatory (PBO) network protocols by personnel at UNAVCO, with all of the quality and systems checks that this implies. These data are available in near real time. Five sites are equipped with SIM cards and modems for data download via cellular telephone. These data are generally available within a few days of data collection. Remaining sites are downloaded manually, typically every few months, weather permitting (heavy rainfall during the rainy season frequently precludes access to some of the more remote sites). The CGPS stations were installed in phases between 2002 and 2008 (Figure 3.4). Eight sites are equipped with NetRS receivers, which are currently partitioned to record both 5Hz and 15-second data. The 5 Hz data may record long period dynamic offsets associated with future large earthquakes.

The seismic network was deployed in stages between 2006 and 2008 and presently consists of 10 broadband and 7 short-period stations. Tremor signals are very low amplitude and difficult to study with surface instrumentation given typical noise levels at the Earth's surface. The most common source of 1-10 Hz seismic noise arises from human activity or wind coupling into the Earth. These noise sources attenuate with

depth resulting in significant noise reduction when locating seismometers below the surface. The present seismic network includes 4 short-period seismometers deployed in 100 m boreholes and 4 broadband sensors in 5 m deep vaults. Several of the seismic and GPS stations are co-located. However, due to the high seismic sample rates, these data are manually downloaded approximately once every six to eight weeks.

Table 3.1 Nicoya CGPS station specifications.

Site Name	Equipment	Communications	Monument Type
BON2	Trimble 5700	Manual Download	Concrete Pier ¹
ELVI	Trimble NetRS	Cell / Internet	Shallow Monument ²
GRZA	Trimble NetRS	Cell	Shallow Monument ²
HATI	Trimble NetRS	Manual Download	Shallow Monument ²
HUA2	Trimble 5700	Manual Download	Concrete Pier ¹
INDI	Trimble 5700	Manual Download	Concrete Pier ¹
LEPA	Trimble NetRS	Cell	Deep Monument ³
LMNL	Trimble NetRS	Cell / Internet	Shallow Monument ²
PNEG	Trimble 5700	Manual Download	Concrete Pier ¹
PUMO	Trimble NetRS	Manual Download	Shallow Monument ²
PUJE	Trimble 5700	Manual Download	Concrete Pier ¹
QSEC	Trimble NetRS	Cell	Deep Monument ³
SAJU	Trimble NetRS	Manual Download	Shallow Monument ²

¹Concrete pier monument: Rebar reinforced concrete pillar reaching depths of 4-5m

²Shallow PBO style monument: 4 legs (tripod and center pole) anchored at ~1.5m depth in the presence of bedrock

³Deep PBO style monument: 4 legs (tripod and center pole) anchored at 10-12 m in the absence of bedrock

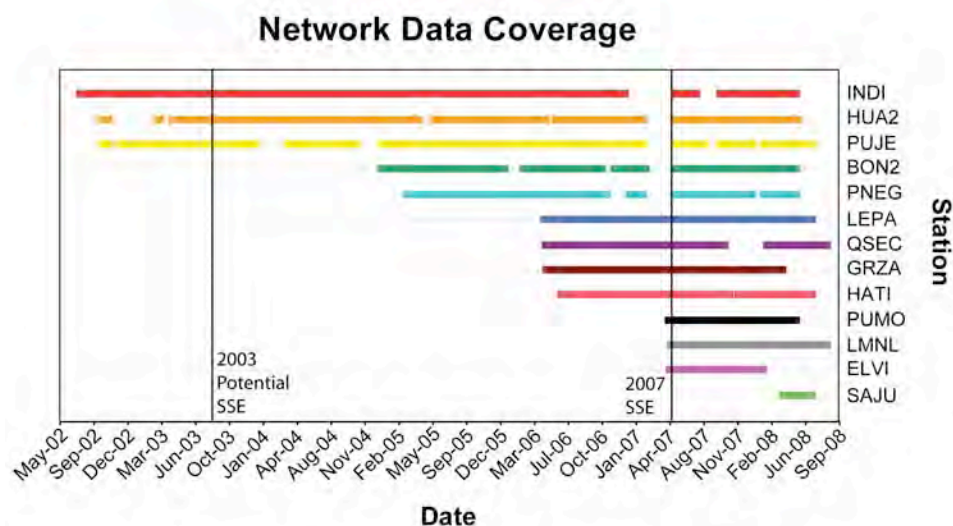


Figure 3.4 Order and timing of CGPS station installation with respect to potential 2003 SSE and 2007 TSE and data availability.

3.4 Data and Analysis

3.4.1 GPS Analysis

Data from all GPS stations were processed following *Dixon et al.* [1997] and *Sella et al.* [2002] using GYPSY version 4.04 precise point positioning software developed at JPL and using satellite and clock files from JPL [*Zumberge et al.*, 1997]. Phase ambiguity resolution was performed using the algorithm AmbiZAP [*Blewitt and Kreemer*, 2007]. Baselines from each station to site MANA in Managua, Nicaragua, approximately 250 km north of the Nicoya network, were calculated to reduce common mode errors (e.g. orbit related errors). Common mode errors can have signatures similar to the slip event of interest. MANA does introduce a certain amount of white noise in the solutions; however this should not bias the results in a systematic way. The resulting time series are shown in Figure 3.5. The time series are organized in three groups by distance from the coast (Coastal, Mid-Peninsula and Inland stations) and ordered within each group by latitude, from north to south. I did not include the vertical component in my models, as the vertical data are sufficiently noisy that no statistically significant offsets were observed.

3.4.2 Slow Slip Event Analysis

Characterization of the slow slip event in the GPS time series was done using the hyperbolic tangent model of *Larson et al.* [2004]. This is a five-parameter model that includes the initial position (x_0), the background site velocity (V), assumed to be constant before and after the event, the event offset (U), the midpoint time of the event (T), and duration half width (τ) (Figure 3.6):

$$X(t) = x_0 + Vt + \frac{U}{2} \left[\tanh \frac{t-T}{\tau} - 1 \right] \quad (3.1)$$

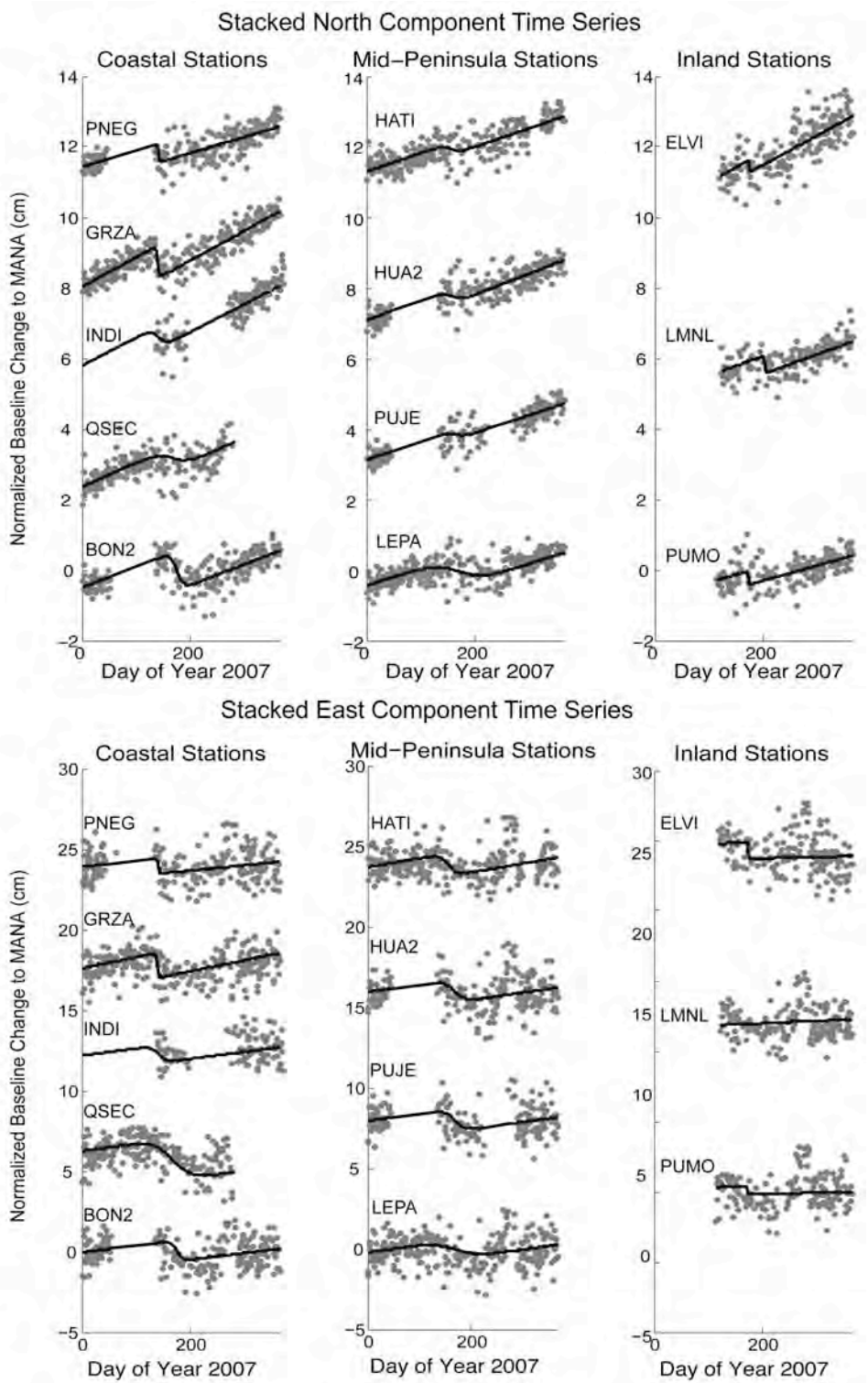


Figure 3.5 Stations are organized in three groups by longitude and within each group by latitude. All fits use station optimized timing parameters a) Time series for the North component of the CGPS stations. b) Time series for the East component of the CGPS stations.

The model is fit to the data by nonlinear regression and least squares techniques. Residuals and confidence intervals are also estimated during the least squares analysis.

Some of the time series are sufficiently noisy that simultaneous estimation of all five parameters is not possible (though detection of the offset is clear even in stations with low signal to noise ratios, e.g., HATI in Figure 3.6). For these time series, I estimated parameters in an iterative manner, as follows. In baseline time series with a high signal to noise ratio and a clear representation of the slip event, I first loosely defined the event timing (duration and event midpoint), then estimated the background velocity of the station and finally refined the estimates of the event timing.

The length of the time series used to determine background velocity was as long as possible, taking into account equipment installation, a possible Slow Slip Event in 2003 [Protti *et al.*, 2004], monument settling time and a conservative temporal window in which the 2007 TSE may have occurred. This is done separately for both the north and east components of motion at each station. This provides an adjusted interseismic velocity relative to the reference station (Figure 3.5) which can be rotated to define velocities relative to the stable Caribbean Plate [DeMets, 2001] (Figure 3.7). Deviation of these interseismic velocities from the plate convergence direction primarily reflects forearc sliver transport [Lundgren *et al.*, 1999; DeMets, 2001; Inuma *et al.*, 2004; Norabuena *et al.*, 2004; LaFemina *et al.*, 2009]. Uncertainties for the velocity estimates (Table 2) were calculated following the formulations in Dixon *et al.* [2000] and Mao *et al.* [1999].

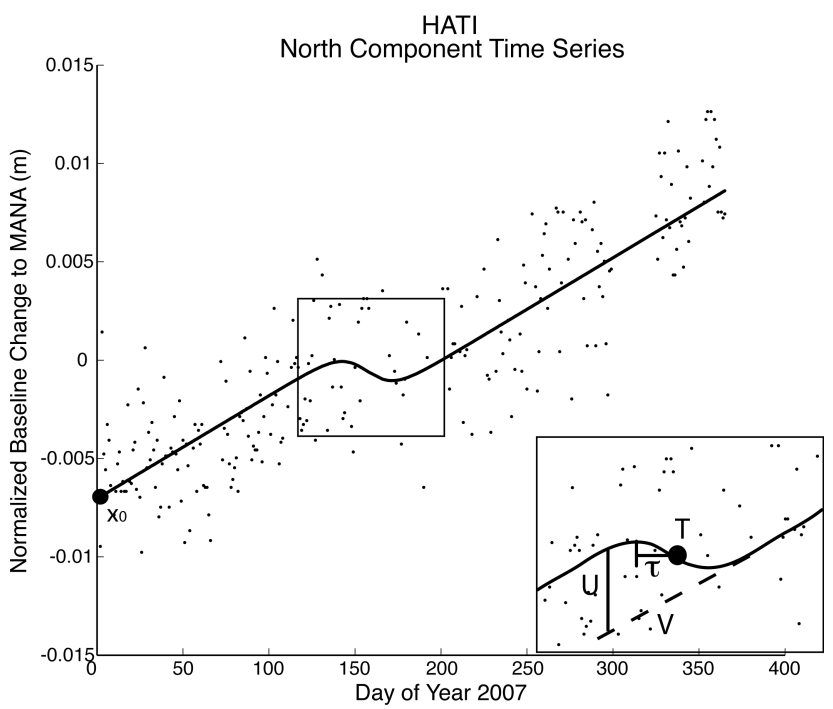


Figure 3.6 North component of station HATI with best-fit model, annotated with model parameters. Although station has relatively poor signal to noise ratio (table 3.2a), the offset U is still clearly defined.

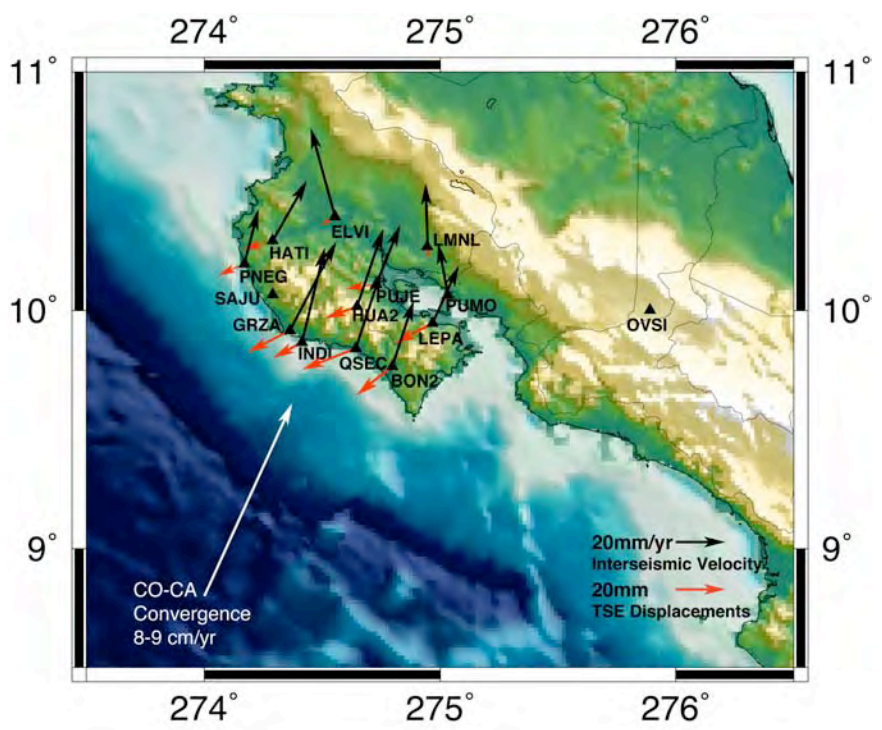


Figure 3.7 Adjusted interseismic velocity vectors relative to stable Caribbean plate (black vectors); and the best fitting surface displacements for the 2007 TSE (red vectors). Iterative velocity fits using station optimized model fits.

Once the interseismic velocity is established, this value is used in subsequent iterations to refine the estimates of T , τ and U . Two different approaches were used. In the first approach, best fit estimates for all parameters are obtained, requiring only the timing parameters (T and τ) are the same for both (N, E) horizontal components at each station. This allows timing parameters to vary between stations, e.g. to investigate possible migration of slip. The combined chi squared misfits of the north and east components were minimized to identify the best fitting parameters. These will be referred to as station-optimized fits and are shown in Table 3.2a.

One weakness of this approach is that event timing (T , τ) is poorly defined for some stations with poor signal to noise ratio and thus may affect the offset estimates. I therefore used a second approach, fixing the timing parameters, T and τ , to average values based on 7 stations where the event is well defined and the signal to noise ratio is high (2007 day of year 160 and 20 days respectively). These fits will be referred to as network-optimized fits and are shown in Table 3.2b. Displacement estimates from the two approaches (Table 3.2a, 3.2b) are very similar. A comparison of these two fits is presented in Appendix A.

In the case of high data noise, the timing parameters were constrained using the best-fit parameter from the least noisy component. In other words, at a given station I enforced the physically plausible assumption that event timing must be the same in the north and east components. This was done for HATI and ELVI in the east component;. For the station-optimized fits (Table 3.2a), timing parameters from one component were also used to fix the other component if the offset is sufficiently small to be masked by data scatter. This was the case for the north component of PUJE and the east component

of LMNL. For noisy time series where parameter fits were done iteratively, I checked that the offset estimates were not sensitive to the choice of initial conditions.

Fits to the GPS time series using the station-optimized approach are shown in Figure 3.5. Figure 3.7 shows the corresponding offsets and interseismic velocities in map view.

It is evident from Tables 2a and 2b that the offset (U) and velocity (V) parameters are better constrained than the duration (2τ) and mid point of the event (T). This can be understood in terms of a simple white noise model, whereby parameter uncertainty scales as $1/\sqrt{n}$, where n is the number of data. As the length of the time series increases, the estimates of V and U improve because the number of data points used to constrain these parameters increases. In general, stations installed in the first (2002) and second (2005) phases will have lower uncertainties in V and U compared to stations installed later. However, the duration of the event is limited compared to the total length of the time series. Hence, the parameters T and τ tend to have larger relative uncertainties, as the number of data available to constrain them (typically 20-40) is small. Thus, the uncertainties for T and τ will not depend on station installation time, and to a first approximation will not improve with increased observation time (improving the velocity uncertainty does have some effect on the uncertainties for T and τ , but the effect is small). In addition, for some stations there were data outages or the station came on-line very close to the beginning of the event (see Figure 3.4), therefore the duration estimates for these stations can be considered a minimum estimate.

Table 3.2a Station-optimized hyperbolic tangent model fits.

Site	N/E	V (mm/yr)	U (mm)	T 2007 DOY ^a	Start Day 2007 DOY ^a	Tau (days)	Duration (days)	WRMS ^b	Signal To Noise Ratio
BON2	N	21.4 ± 1.6	-11.2 ± 0.6	176 ± 1.5	165.0	11.0 ± 3.5	22	3.0	3.8
	E	15.2 ± 3.7	-14.4 ± 1.8	176 ± 13.0	165.0	11.0 ± 27.0	22	8.7	1.7
ELVI	N	30.5 ± 11.1	-3.5 ± 2.0	174 ± UC ^c	173.5	0.5 ± UC ^c	1	3.9	0.9
	E	-3.2 ± 15.3	-5.6 ± 9.1	174 (fixed)	173.5	0.5 (fixed)	1	12.8	0.4
GRZA	N	30.6 ± 3.3	-8.9 ± 0.7	140 ± 7.0	137.0	3.0 ± 12.0	6	2.6	3.4
	E	25.3 ± 8.6	-17.2 ± 2.3	140 ± 8.5	137.0	3.0 ± 13.0	6	8.6	2.0
HATI	N	19.1 ± 4.1	-3.5 ± 1.0	157 ± 23.5	141.0	16.0 ± 48.5	32	2.8	1.3
	E	20.4 ± 4.9	-12.4 ± 7.9	157 (fixed)	141.0	16.0 (fixed)	32	8.3	1.5
HUA2	N	21.9 ± 1.4	-4.8 ± 1.3	167 ± 19.5	147.0	20.0 ± 30.0	40	2.7	1.8
	E	17.2 ± 2.1	-13.0 ± 4.8	167 ± 13.5	147.0	20.0 ± 29.5	40	9.4	1.4
INDI	N	29.0 ± 1.5	-6.4 ± 1.1	143 ± 43.0	128.0	15.0 ± 111.5	30	2.9	2.2
	E	15.8 ± 2.2	-11.8 ± 2.9	143 ± 12.5	128.0	15.0 ± 27.0	30	9.1	1.3
LEPA	N	18.0 ± 3.3	-8.3 ± 0.9	171 ± 15.0	127.0	44.0 ± 24.2	88	3.8	2.2
	E	17.2 ± 8.4	-15.5 ± 2.6	171 ± 14.0	127.0	44.0 ± 29.5	88	9.3	1.7
LMNL	N	20.2 ± 3.2	-5.2 ± 1.5	204 ± 19.0	203.5	0.5 ± 19.0	1	2.9	1.8
	E	5.6 ± 10.4	0.2 ± 6.0	204 (fixed)	203.5	0.50 (fixed)	1	10.6	0.0
PNEG	N	16.7 ± 1.7	-4.6 ± 0.8	142 ± 11.5	140.0	2.0 ± 22.5	4	2.9	1.6
	E	12.1 ± 4.7	-10.6 ± 2.2	142 ± 12.0	140.0	2.0 ± 21.5	4	9.4	1.1
PUJE	N	18.6 ± 1.4	-1.8 ± 1.1	168 (fixed)	150.0	18.0 (fixed)	36	2.7	0.7
	E	16.2 ± 3.7	-12.1 ± 3.1	168 ± 22.0	150.0	18.0 ± 41.0	36	8.8	1.4
PUMO	N	15.7 ± 4.0	-4.2 ± 1.6	173 ± 9.5	172.5	0.5 ± 14.0	1	2.9	1.5
	E	2.5 ± 14.3	-3.3 ± 5.8	173 ± UC ^c	172.5	0.5 ± UC ^c	1	10.4	0.3
QSEC	N	25.5 ± 3.4	-8.5 ± 0.9	168 ± 15.0	136.0	32.0 ± 21.0	64	2.9	2.9
	E	16.6 ± 8.9	-21.6 ± 3.0	168 ± 14.0	136.0	32.0 ± 33.0	64	8.6	2.5

^aJulian Day^bWeighted Root Mean Square^cUnconstrained

Table 3.2b Network-optimized hyperbolic tangent model fits.

Site	N/E	V (mm/yr)	U (mm)	T 2007 DOY ^a (fixed)	Start Day 2007 DOY ^a (fixed)	Tau (days)	Duration (days)	WRMS ^b
BON2	N	21.4 ± 1.6	-11.1 ± 0.6	160.0	140.0	20.0	40.0	3.0
	E	15.2 ± 3.7	-14.6 ± 1.9	160.0	140.0	20.0	40.0	8.7
ELVI	N	30.5 ± 11.1	-4.4 ± 2.5	160.0	140.0	20.0	40.0	3.9
	E	-2.3 ± 15.3	-8.1 ± 14.0	160.0	140.0	20.0	40.0	12.7
GRZA	N	30.6 ± 3.3	-9.0 ± 0.7	160.0	140.0	20.0	40.0	2.8
	E	25.3 ± 8.6	-17.4 ± 2.4	160.0	140.0	20.0	40.0	8.6
HATI	N	19.1 ± 4.1	-5.5 ± 0.8	160.0	140.0	20.0	40.0	3.2
	E	5.0 ± 4.9	-5.4 ± 5.8	160.0	140.0	20.0	40.0	8.6
HUA2	N	21.9 ± 1.4	-4.7 ± 1.4	160.0	140.0	20.0	40.0	2.7
	E	17.2 ± 2.1	-13.8 ± 5.3	160.0	140.0	20.0	40.0	9.4
INDI	N	29.0 ± 1.5	-6.4 ± 1.0	160.0	140.0	20.0	40.0	3.0
	E	15.8 ± 2.2	-11.9 ± 2.9	160.0	140.0	20.0	40.0	9.1
LEPA	N	18.0 ± 3.3	-8.0 ± 0.9	160.0	140.0	20.0	40.0	3.8
	E	17.2 ± 8.4	-15.4 ± 2.5	160.0	140.0	20.0	40.0	9.2
LMNL	N	20.2 ± 3.2	-6.7 ± 2.4	160.0	140.0	20.0	40.0	3.0
	E	5.6 ± 10.4	-7.2 ± 9.3	160.0	140.0	20.0	40.0	10.4
PNEG	N	16.7 ± 1.7	-4.6 ± 0.7	160.0	140.0	20.0	40.0	2.9
	E	12.1 ± 4.7	-10.8 ± 2.2	160.0	140.0	20.0	40.0	9.4
PUJE	N	18.6 ± 1.4	-1.8 ± 1.1	160.0	140.0	20.0	40.0	2.7
	E	16.2 ± 3.7	-12.2 ± 3.1	160.0	140.0	20.0	40.0	8.8
PUMO	N	15.7 ± 4.0	-4.7 ± 1.9	160.0	140.0	20.0	40.0	2.9
	E	2.5 ± 14.3	-20.4 ± 7.5	160.0	140.0	20.0	40.0	10.6
QSEC	N	25.5 ± 3.4	-8.2 ± 0.9	160.0	140.0	20.0	40.0	2.9
	E	16.6 ± 8.9	-21.2 ± 2.9	160.0	140.0	20.0	40.0	8.7

^aJulian Day
^bWeighted Root Mean Square

3.4.3 Seismic Tremor

Colleagues at the University of California – Santa Cruz, did all work on the seismic tremor data and inversions. It is presented here for completeness and to show corroborating evidence for the tremor and slip event.

Tremor is a long lasting vibration differing from tectonic earthquake recordings in its very long duration, lack of impulsive seismic arrivals and low dominant frequencies (~2-6 Hz). These characteristics make tremor challenging to detect and locate. In southwest Japan and Cascadia, tremor has been identified by the coincidence of high

amplitude envelopes on several nearby stations (e.g., [*Obara, 2002; McClausland et al., 2005; Wech and Creager, 2008*]) and in Mexico by synchronous episodes of high spectral amplitude in the 1-8 Hz range lasting minutes to hours [*Payero et al., 2008*]. Higher amplitudes on horizontal components and particle motions indicate that S-waves dominate tremor energy. Tremor episodes are commonly located by cross-correlation of station envelopes to obtain relative delay times that are used as S-wave arrival times in standard earthquake location algorithms. Although locations obtained in this manner identify the source volume generating tremor (horizontal errors on the order of 10-20 km and depth errors 2-3 times larger) and can reveal general tremor migration patterns, they are usually not accurate enough to determine whether tremor activity is localized to the subducting plate interface or how tremor locations relate to frictional properties of the interface.

In southwest Japan, impulsive arrivals embedded in tremor have been cataloged by the Japan Meteorological Agency as low-frequency earthquakes (LFEs). *Shelly et al. [2007a; b]* used LFEs in this catalog as template events to systematically search tremor signals for matching waveforms and found that tremor consists of a sequence of LFEs. Using an autocorrelation method to identify LFEs when no catalog existed, *Brown et al. [2008; 2009]* established that tremor episodes accompanying slow slip in SW Japan, Cascadia and northern Costa Rica can all be explained by a nearly continuous sequence of LFEs occurring on or near the plate interface. Due to the identification of P and S phases, the location accuracy of LFEs is several orders of magnitude better than that obtained for tremor episodes from envelope cross-correlation. However, LFE identification and location is computationally intensive, making it impractical to apply to

months of seismic data.

For the Nicoya peninsula, tremor episodes were identified between April and July 2007 by visual inspection of tremor envelopes constructed from the EW component of ground motion filtered in the 2-6 Hz band. Location estimates for tremor episodes occurring over a one week period during the May 2007 slow slip event were determined and compared, to accurate LFE locations embedded within 3 hours of tremor recorded on May 17, 2007, during the most energetic tremor episode of the slow slip event. Figure 3.8 shows 2 different hours of tremor recorded at 3-4 borehole stations (ELVI, PALO, SANL and ARAD), one deep vault (ARDO) and several surface stations on May 17 hour 1 (Figure 3.8a) and May 21 hour 4 (Figure 3.8b) 2007, during the middle of the slow slip event. Coherent tremor bursts can be tracked at stations located over 50 km apart but are not always apparent at stations more distant from the center of the network (LEPA and PNCB to the southeast and SARO to the northwest). Figure 3.3 shows cumulative minutes of tremor per day versus day of year, compared to the time series of the north component of GPS station GRZA, for the year 2007, indicating a strong peak in tremor activity between May 17 and 22, roughly corresponding to the middle of the geodetic event.

Approximate locations of these tremor episodes were obtained by cross-correlating their envelopes with a reference station, using relative time differences as S wave arrival times in Hypoinverse-2000 [Klein, 2007]. Fifty-two tremor episodes, with horizontal location errors less than 10 km are shown in Figure 3.8. Also plotted on this figure are 232 LFEs that were detected and located during three hours of tremor on May 17, 2007 using a running network autocorrelation method [Brown *et al.*, 2009]. Tremor

and LFEs could not be located in the southeast portion of the Nicoya Peninsula due to the absence of adequate station coverage; ACHA was not installed until February 2008 and LEPA had a bad clock during this period. However, the general scarcity of tremor detections at LEPA and PNCB suggest that far fewer tremor sources originate in this region.

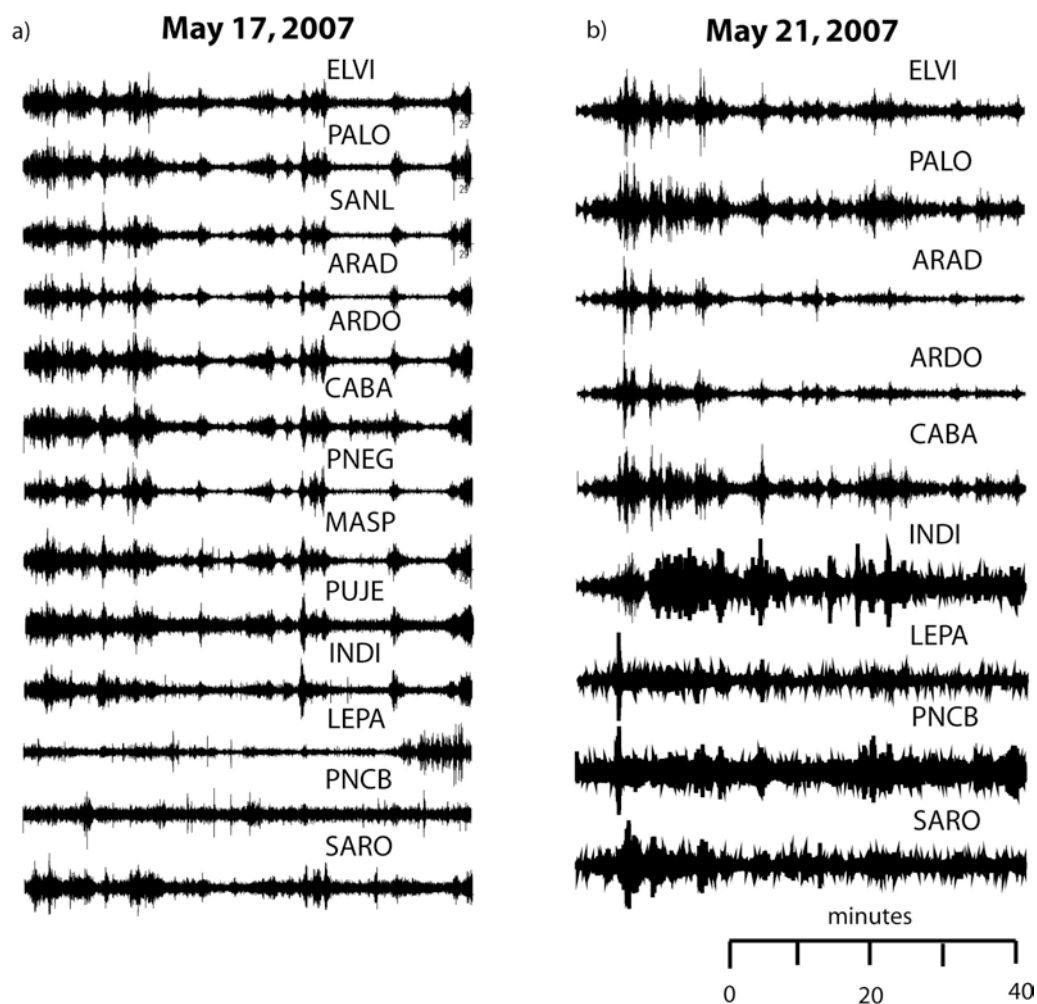


Figure 3.8. One hour of seismic tremor, filtered from 2-6 Hz, recorded on the east component at short period borehole (ELVI, PALO, SANL, ARAD), broadband deep vault (ARDO), broadband (CABA, INDI, PNCB, SARO) and short-period (PNEG, MASP, PUJE, LEPA) surface stations for two different time periods during the 2007 tremor and slip event: a) JD 137 hr 1 and b) JD 141 hr 4. Tremor traces are normalized but the tremor episodes on JD 141 are 2-3 times larger on all stations.

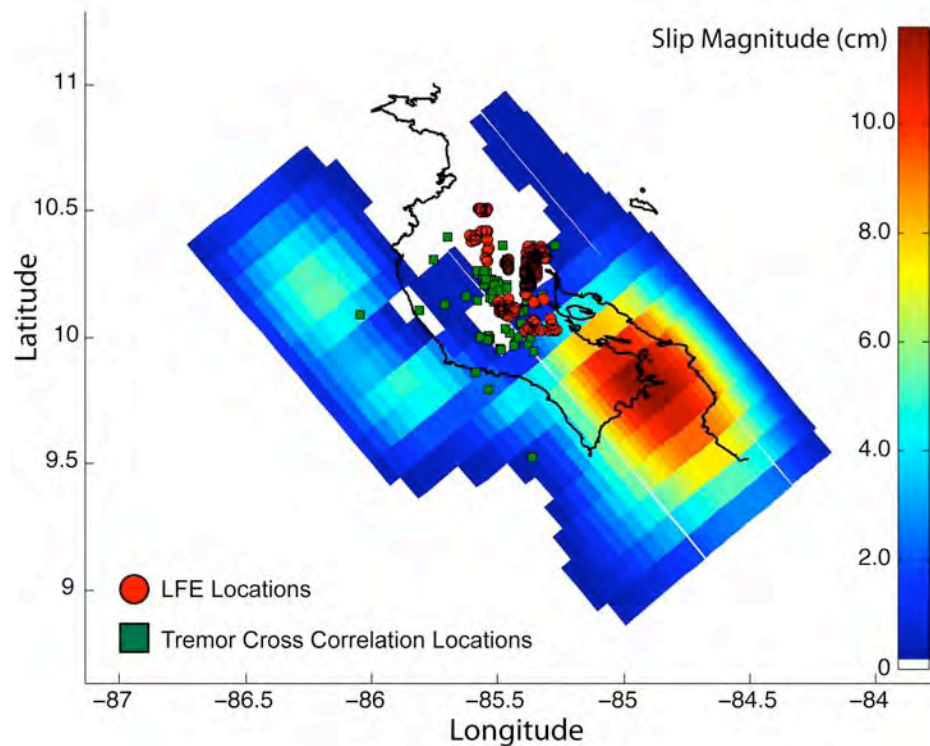


Figure 3.9. Locations of tremor episodes and low frequency earthquakes (LFEs) compared with slow slip distribution.

Approximate locations of tremor episodes recorded between May 17th and 22nd, were obtained by cross-correlating their envelopes with a reference station and using relative time differences as S wave arrival times in Hypoinverse-2000 [Klein, 2007]. Fifty-two tremor episodes, with horizontal location errors less than 10 km are shown in Figure 3.9. Also plotted on this figure are 232 LFEs that were detected and located during the first three hours of tremor on May 17, 2007 using a running network autocorrelation method [Brown *et al.*, 2009]. Tremor bursts and LFEs locate in roughly the same regions, given the large errors associated with the tremor envelope locations. This supports the contention of Brown *et al.* [2009] that tremor is composed of swarms of LFEs. The LFEs locate on the plate interface [Brown *et al.*, 2009], down-dip of the

locked seismogenic zone defined by microseismicity [DeShon *et al.*, 2006]. Tremor or LFEs could not be located in the southeast portion of the Nicoya Peninsula due to the absence of adequate station coverage: ACHA was not installed until February 2008, noise levels at the southeastern stations INDI and PNCB are 4 to 8 times greater than the northwestern stations, and LEPA had a bad clock during the time period of the 2007 TSE. However, it is believed likely that tremor sources extend farther to the southeast than indicated in Figure 3.9 based on the occurrence of tremor bursts that are visible only on records from the southeast most stations LEPA and PNCB (Figure 3.8b).

3.5 Inversion Results

A linear inversion [Funning *et al.*, 2005a] based on the formulation of Okada, [1985] was used to estimate the magnitude and distribution of slip on the fault plane, using the surface displacements in Tables 3.2a (station-optimized fits) and 3.2b (network-optimized fits). The inversion code creates Green's functions using a model for slip on a rectangular dislocation in an elastic half space.

The plate interface was modeled as three adjoining rectangular dislocation planes using the geometry described in Norabuena *et al.* [2004] (Figure 3.10). From the trench to 15 km depth, the interface dips at 10° ; from 15 km to 38 km depth, the interface dips at 25° ; and from 38 km to 60 km, the interface dips at 43° . The strike of the fault plane is defined by the average orientation of the trench offshore, 320° . The length of each fault segment extends a total of 250 km centered on the Nicoya Peninsula to minimize possible edge effects. In order to represent variable, distributed slip on a large fault plane, the

dislocations were meshed in 20 equal divisions along-strike and 15 equal divisions down-dip.

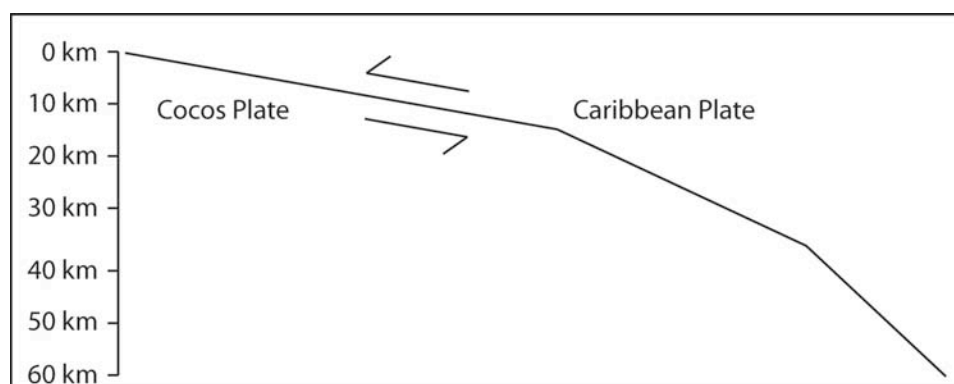


Figure 3.10 Cross section of fault geometry used for slip inversion from Norabuena et al., [2004].

I constrained slip direction in the model, testing several values. I first constrained the slip direction to be 10° counter-clockwise of trench normal (220°), similar to convergence direction (Figure 3.7). This constraint is supported by the a priori knowledge of the convergence direction [DeMets, 2001] and by the general knowledge that strain release events are generally anti-parallel to convergence direction. I also tested values of 238° and 244° , representing the average azimuth of the station-optimized fits and network-optimized fits respectively. Results of all three were very similar and for the remainder of the text I will restrict discussion to the results consistent with convergence direction (220°). Details of inversions using 238° and 244° can be found in Appendix A.

To avoid geologically unreasonable slip, Laplacian smoothing is imposed and the data are inverted using a fast non-negative least squares algorithm [Bro and De Jong, 1997; Funning et al., 2005a]. Inversion results for the two groups of estimated offsets (station-optimized, network-optimized) are virtually identical. Given this, and that ETS events have been shown to propagate in other regions of the world [Rogers and Dragert,

2003; Obara *et al.*, 2004; Kao *et al.*, 2005; Ito *et al.*, 2007], hereafter I restrict discussion to the station-optimized estimates, however the procedures have been duplicated for the network-optimized estimates for completeness. Network optimized inversion results can be found in Appendix A.

I weight the GPS data according to estimated uncertainties shown in Table 2a. I compare the results from both weighted and unweighted data to ensure that the results were not biased by error estimates, since a rigorous analysis of the offset uncertainties has not been done. Results of the weighted and unweighted inversions are remarkably similar. Hereafter I will restrict discussion to inversions using the weighted data set. I inverted the weighted offsets presented in Table 3.2a and Table 3.2b. As stated, only those results from the station-optimized fits (Table 3.2a) are presented. Details of the unweighted inversions can be found in Appendix A.

There is a well-known trade-off between the amount of smoothing applied and the wrms misfit of the model (Figure 3.11). This relationship holds true for all tested models. I show results for two end member smoothing values (1.6×10^6 and 1.0×10^8) corresponding to weighted root mean square (wrms) misfits of 4.5 mm and 8.2 mm respectively, close to the average data noise for the north and east components respectively and encompassing the range of slip models that I consider plausible. The maximum displacement differs by nearly a factor of five from 2.2 cm for the ‘smooth’, higher misfit, model to 11.8 cm for the ‘rough’, lower misfit model, but the geodetic moment (a product of slip and area) is better constrained. The maximum slip on the fault plane trades off with the size of the slip patches, and the geometry of the slip distribution. Low misfit models have slip separated into two patches while higher misfit models define

a continuous patch. Observed vs. modeled offsets at each CGPS site with associated fault plane slip solutions are shown in Figure 3.12. The geodetic moment differs by a maximum of 2.25×10^{19} Nm, ranging from 3.49×10^{19} Nm to 1.25×10^{19} Nm (close to a factor of 3) (Figure 3.11), equivalent to moment magnitudes of 6.7 for the ‘smooth’ model and 7.0 for the ‘rough’ model.

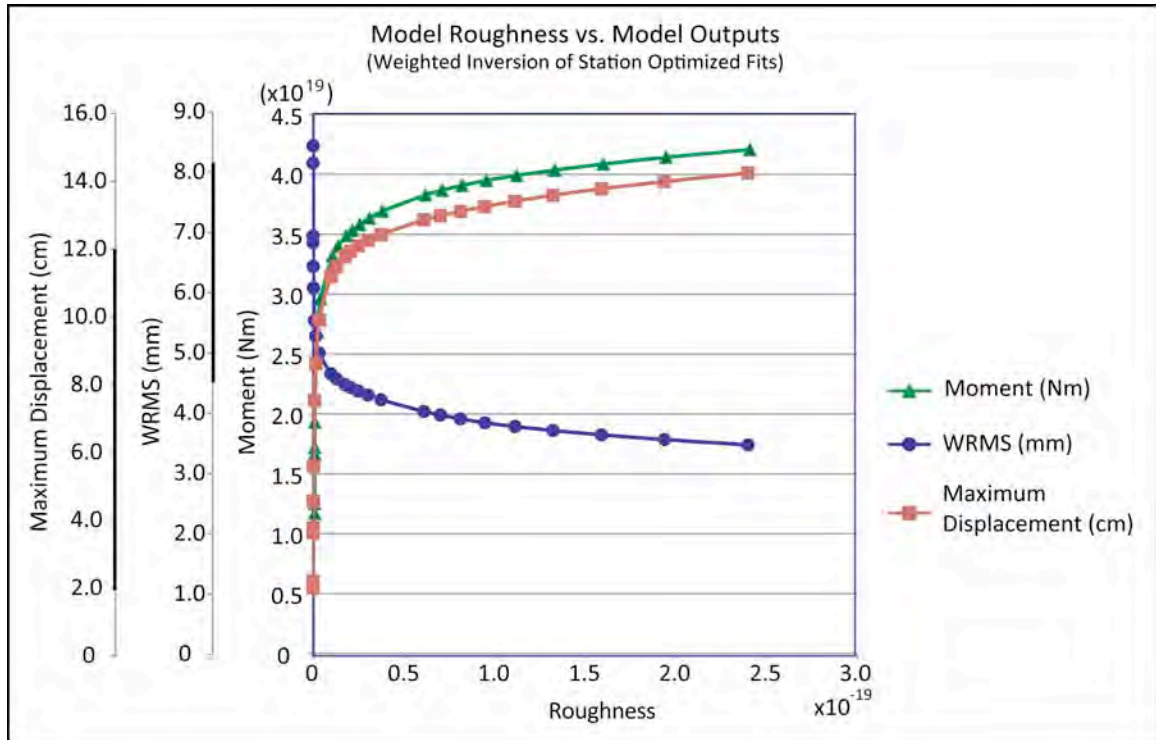


Figure 3.11 Plot of inversion model roughness to wrms, moment and magnitude of maximum displacement for weighted inversion of station-optimized fits. Bold axis indicate the range of models discussed in text. (wrms=8.2 and wrms=4.5).

The equivalent magnitude is calculated using the moment magnitude formula:

$$M_w = \frac{\log M_0}{1.5} - 10.73 \quad (3.2)$$

where M_w is the moment magnitude and M_0 is the seismic moment in Dyne-cm. The seismic moment is calculated by:

$$M_0 = \mu \bar{D} S \quad (3.3)$$

where D is the average slip on the fault plane and S is the rupture area for the earthquake. In this case μ is the rigidity of the medium and is assumed to be 34.3 GPa. The moment magnitude formula is the most beneficial for calculating the equivalent magnitude of a slow slip event because the formula has no dependence on the arrival times or speed of rupture, amplitude of an arrival wave, or distance from the source that is inherent in other formulas. Since the major difference between an earthquake and an ETS event is the speed of rupture and duration of the event, it is imperative to eliminate dependence these differences to do a quantitative comparison of the processes. The moment magnitude is also directly relatable to the physics that govern an earthquake, as well as to the M_s moment estimation, until the M_s reaches saturation.

To test whether I have the data density to identify patches of slip on the fault plane resolution tests were done following the methods of *Funning et al.* [2005b] and *Biggs et al.* [2006]. To do this, I imposed one meter of slip on one mesh segment and calculated the resulting surface displacements at each GPS station, as in a forward model. I then inverted the resulting surface vectors for slip on the fault plane to find the inferred slip. This was done for each mesh pixel and summed to find the along strike and down dip resolution of the model (Figure 3.13). I found that I do indeed have the resolution to identify two distinct patches of slip. This is supported by the fact that the average station spacing (~25 km) is less than the size of the slip patches in the two-patch (low misfit) model. The remaining discussion focuses on the two-patch model.

Using the parameters from the preferred weighted inversion model, I inverted the dataset iteratively removing one GPS data point at a time to determine if the model output was more sensitive to any one station. The results of this test are presented in

Table 3.3. I find that while small variations in wrms and maximum displacement occur, the pattern of slip does not vary when any single station is removed, implying that the slip distribution results are robust and not dominated by the signal of any one station. The inversion results for this and similar sensitivity tests are presented in Appendix A.

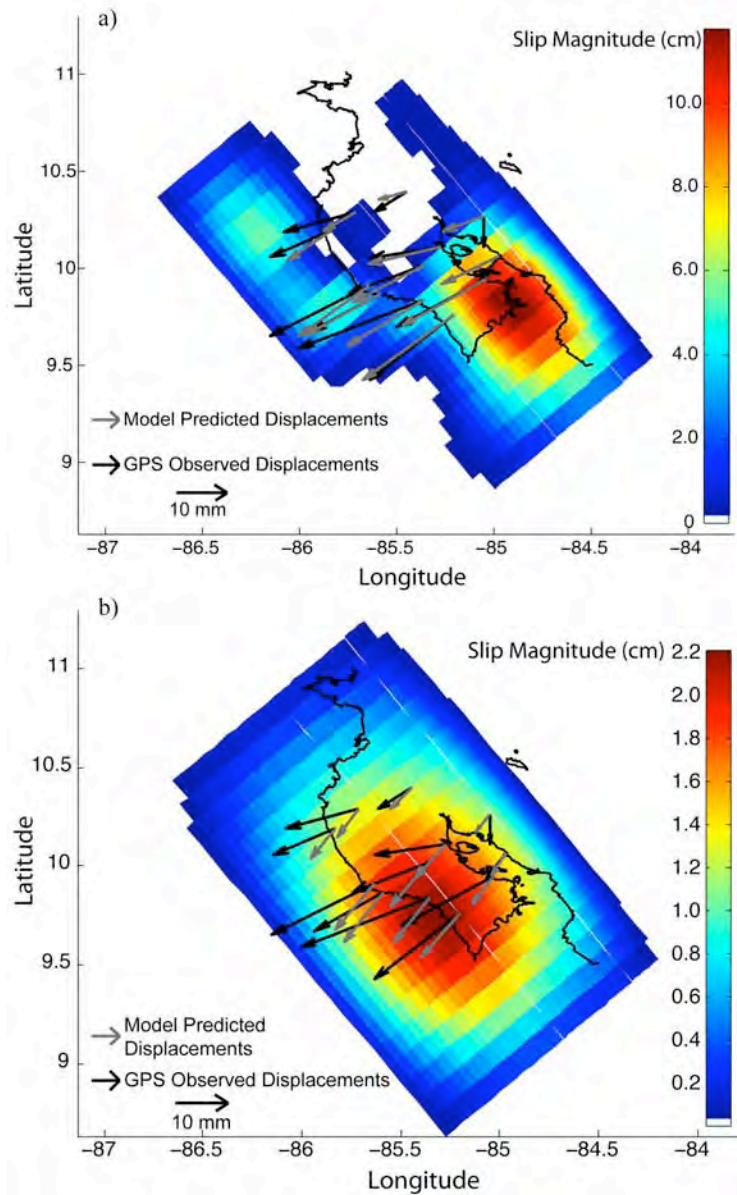


Figure 3.12. Predicted vs. observed offsets for end member models shown in Figure 3.11. a) Station-optimized timing parameters, weighted inversion, $wrms=4.5$ mm. b) Station-optimized timing parameters, $wrms=8.2$ mm. White areas within modeled fault plane indicate negligible or no slip.

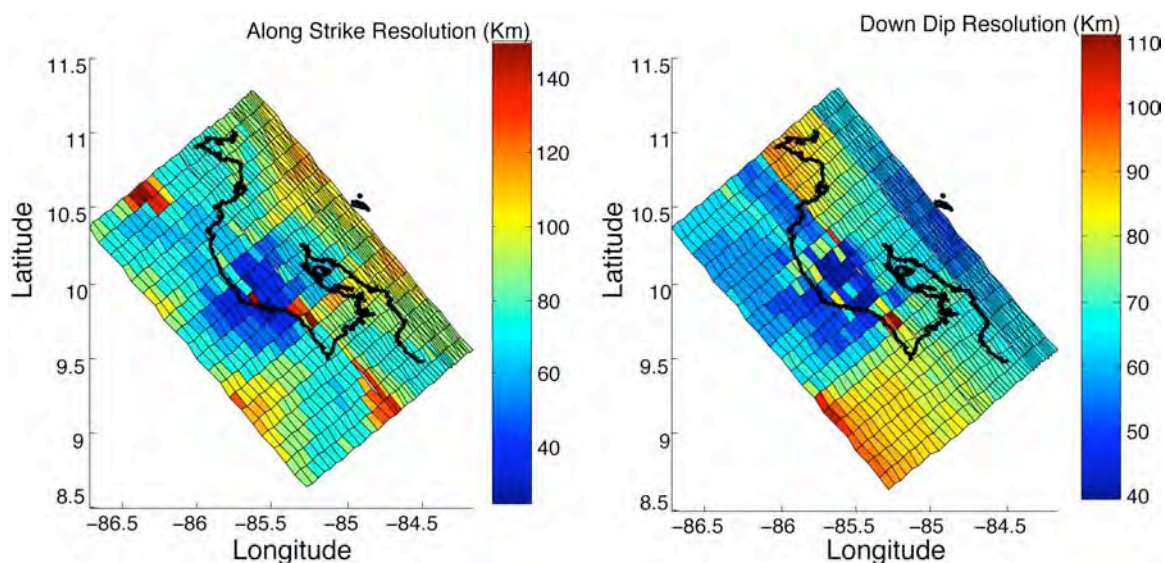


Figure 3.13 Along strike and down dip model resolution results, showing minimum resolvable patch size in km.

Table 3.3 Results of weighted inversion, iteratively eliminating one station.

WRMS (mm)	Moment (Nm)	Maximum Displacement (cm)	M_w	Station Removed
4.51	3.49E+19	11.78	7.0	All stations
4.75	3.66E+19	12.84	7.0	BON2
4.71	3.46E+19	11.84	7.0	ELVI
4.36	3.50E+19	11.93	7.0	GRZA
4.25	3.43E+19	11.75	7.0	HATI
4.65	3.38E+19	11.52	7.0	HUA2
4.62	3.56E+19	11.84	7.0	INDI
4.64	3.21E+19	10.82	6.9	LEPA
4.24	3.43E+19	12.10	7.0	LMNL
4.62	3.31E+19	11.66	6.9	PNEG
4.63	3.56E+19	11.58	7.0	PUJE
4.27	3.56E+19	11.87	7.0	PUMO
3.86	3.68E+19	12.25	7.0	QSEC

The significance of the up-dip patch in the lower misfit, low smoothing model (Figure 3.12a) is not clear; station density here is low. Since the occurrence of the 2007 event, reported here, an additional six stations have been installed (Figure 3.14), increasing the offshore resolution and providing a baseline station that is closer and has less station noise than MANA, the station currently used, in the case of another similar

future event. However, the occurrence of a shallow slip event in 2000 [Brown *et al.*, 2005; LaBonte *et al.*, 2009] and a pressure transient observed in ODP (ocean drilling program) boreholes offshore the Nicoya Peninsula coincident with the May 2007 event [M. Hesseemann, *personal communication*, 2009] suggests that the shallow slip patch may be real.

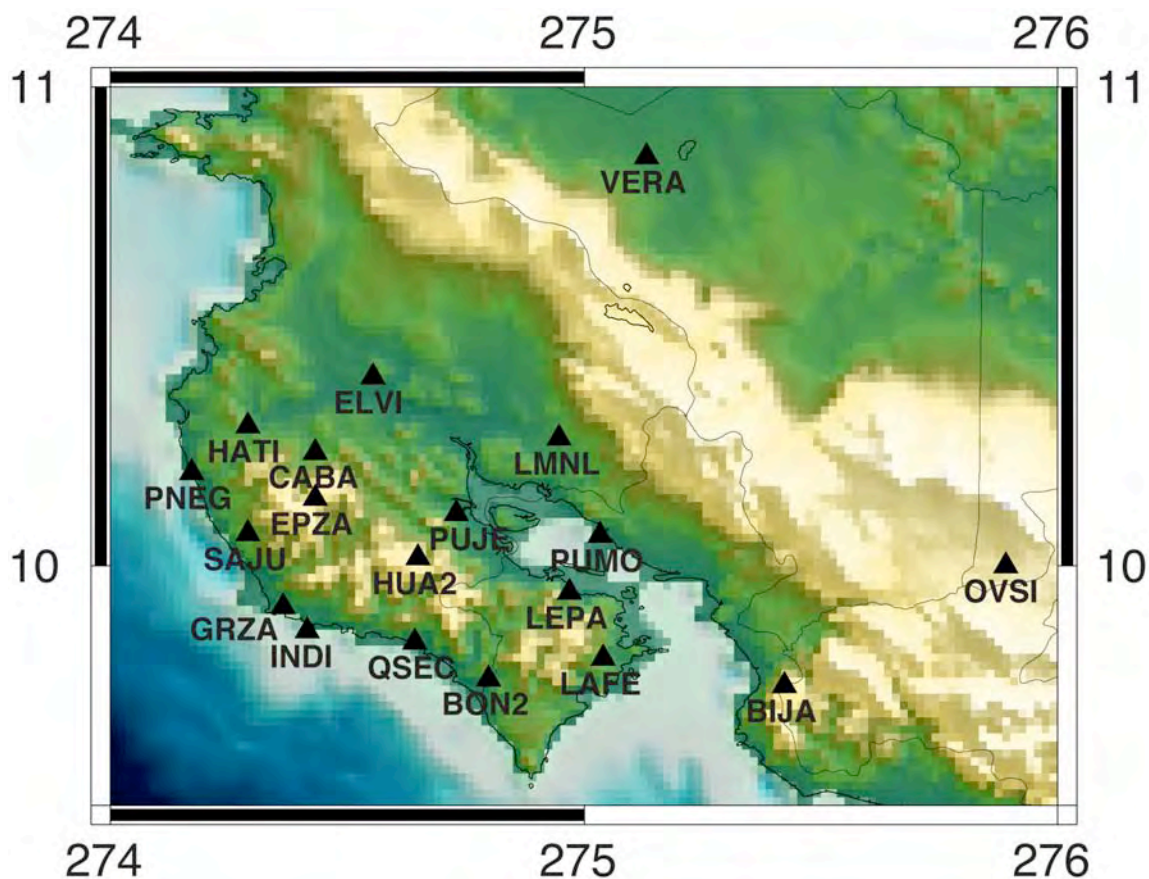


Figure 3.14. The updated Continuous GPS network configuration since the 2007 TSE.

3.6 Discussion

3.6.1 Previous Observations of Slow Slip Events

The occurrence of tremor and slip events has been previously suspected in this region based on correlated fluid flow and seismic tremor recorded on ocean bottom

instruments near the margin wedge in 2000 [*Brown et al.*, 2005] and on data from a sparse network of three permanent GPS stations in September 2003 [*Protti et al.*, 2004]. During the 1999-2000 CRSEIZE experiment, a correlation between episodic fluid flow in and out of the sea floor with seismic noise recorded on Ocean-Bottom Seismographs (OBS) was discovered. This phenomenon was observed on only 3 (out of a total of 14) OBS instruments at the base of the continental margin of Costa Rica. *Brown et al.* [2005] proposed that this resulted from slow slip on the plate interface in the vicinity of the OBS stations. More recently, *LaBonte et al.* [2009] used a 2-D fully coupled poroelastic finite-element model to show that the detailed patterns of the fluid flow time series could be matched by a propagating dislocation on the plate interface beneath the flow meters. Their best-fit model had slow-slip initiating at a depth of less than 4 km, propagating bilaterally at an average rate of ~ 0.5 km/day and lasting 20 days or more. This interpretation implies that stress on the shallowest portion of the plate interface is relieved episodically in slow slip, supporting the possible existence of shallow slow slip in the 2007 event (which is centered at ~ 6 km vertical depth). These results are significant in that they are the first to suggest that slow slip may occur at the up dip transition from stick-slip to stable sliding; prior locations of slow slip have been limited to the down dip frictional transition (e.g., [*Dragert et al.*, 2001; *Ozawa et al.*, 2004; *Beavan et al.*, 2007]).

The first three continuously recording GPS stations deployed on the Nicoya Peninsula (INDI, HUA2, PUJE), recorded a transient deformation event lasting approximately one month in September – October 2003. The transient displacements were nearly opposite in direction to plate convergence and strain accumulation on the

plate interface, and appeared to have propagated down dip. This event was interpreted as a slow slip event located primarily within the seismogenic zone [Protti *et al.*, 2004]. The data were too limited to resolve details of the slip distribution, but were consistent with a simple dislocation model having an average slip of about 2 cm occurring on the plate interface beneath the stations (depth range of 10-35 km). Pressure gauges in ODP boreholes approximately 60 km offshore of the Nicoya Peninsula recorded two transient events in 2003 [Davis and Villinger, 2006]. The second pressure transient occurred about 3 weeks after initiation of the geodetically recorded slow slip event. Davis and Villinger, [2006] suggested that this pressure transient was caused by slow slip propagated up-dip to the trench, delayed but accompanying the onshore propagation recorded by the land GPS stations. This implies that like the 2007 slow slip event, the 2003 event also experienced shallow slip in the region of the up-dip frictional transition. Assuming that the spring 2000 and fall 2003 events are similar to the 2007 slow slip event described here, a slow slip recurrence interval of 42-44 months is obtained.

3.6.2 2007 Event Slow Slip Distribution

The preferred model for the 2007 event has a large slip patch with its maximum displacement at the down dip edge of the microseismicity pattern (~30 km depth), which has been interpreted as the frictional transition from stick-slip to stable sliding [Schwartz and Deshon, 2007]. This is consistent with most observations of slow slip made at subduction zones worldwide [Schwartz and Rokosky, 2007]. In contrast to most other subduction zones, I find a second smaller and much weaker patch of slip that locates at shallower depth (~6 km depth), up dip from the microseismicity. This slip patch likely

occurs at the up-dip frictional transition, however, its location adjacent to a geodetically determined locked region of the plate interface [Norabuena *et al.*, 2004] requires that the shallow transition zone vary along strike. Consistent with global observations, slow slip in the Costa Rica subduction zone appears to occur in complimentary locations to strongly locked regions.

Although my geodetic estimates for event timing are noisy, there is some evidence that the TSE begins near GRZA and INDI and radiates outward. This is consistent with the start date estimates for all of the GPS stations with the exception of LEPA. Station LEPA is exceptional in that it shows the longest event duration in the GPS data and is also located near the area of maximum slip.

The separation of the slow slip distribution into an up-dip northern patch and a down dip southern patch (Figure 3.12a) may be caused by the subduction of genetically different crust beneath each patch. The Cocos Plate became a separate entity 22.7 Ma with the breakup of the Farallon Plate [Barckhausen *et al.*, 2001]. New oceanic crust continued to be formed by means of sea floor spreading at two spreading centers. The East Pacific Rise (EPR) to the west is a fast spreading center and thus produces smooth oceanic crust [Hey, 1977]. The Cocos-Nazca spreading center (CNS) to the south began as a fast spreading center, producing smooth oceanic crust (CNS-1). At 19 Ma there was a ridge jump, transferring a wedge of crust from the Nazca Plate to the Cocos Plate and rotating the spreading center 22° to the East. This jump also transitioned the spreading center to a slower spreading rate, thus creating crust with a rougher bathymetry (CNS-2) [Barckhausen *et al.*, 2001; Meschede *et al.*, 1998]. The boundary between the northern

up-dip patch and the southern down dip patch closely corresponds to the boundary between EPR and CNS-1 crust (Figure 3.1), which intersects the coast near station INDI.

The age of the down going CNS-1 crust (21-23 Ma [Hey, 1977; Barckhausen *et al.*, 2001] is younger than the down going EPR crust (24-25 Ma [Barckhausen *et al.*, 2001]), thus the heat flow of the CNS-1 crust would also be expected to be higher than that of the EPR crust. It has been demonstrated that not only is the heat flow of the CNS-1 crust higher at 105 mW/m^2 , but also that the modeled isotherms in the over-riding plate above this region in southern Nicoya, have a steeper gradient than those in the northern Nicoya Peninsula where the EPR crustal heat flow values are only 20 mW/m^2 [Langseth and Silver, 1996; Fisher *et al.*, 2003; Spinelli and Saffer, 2004; Spinelli *et al.*, 2006]. Fisher *et al.* [2003] and Hutnak *et al.* [2007] attribute lower heat flow in the EPR crust to higher incidence of hydrothermal cooling through seamounts and other outcrops seaward of the trench, which are more common on EPR generated crust than CNS-1 crust which has no identified seamounts. Although it is not clear how the different origins and therefore material properties of the two oceanic crusts influence the location of slow slip, the coincidence of a structural boundary with the transition in slip patch location suggests that it does.

The inversion of the surface displacement data for the depth and pattern of slip on the plate interface shows peak slip at a depth of $\sim 30 \text{ km}$, where estimated temperatures are $\sim 250^\circ - 300^\circ\text{C}$ [Harris and Wang, 2002; Spinelli and Saffer, 2004]. This location is down-dip of the main seismogenic zone, near the upper plate crust-mantle boundary (continental Moho). Based on the metamorphic phase diagrams of [Peacock *et al.*, 2005; Peacock, 2009], reactions involving low-grade metamorphic rocks (e.g. lawsonite-

blueschist facies) are predicted as the slab moves through this temperature and pressure range, presumably releasing H₂O and other fluids in devolatilization reactions. These processes may influence or contribute to the tremor and/or slip; e.g. this changes the pore fluid pressure and normal stress on the plate interface (see discussion in [Schwartz and Deshon, 2007; Peacock, 2009]). While the significance of the northern up dip slip patch is still unknown, this may also be the result of low temperature (~150° - 200°C) metamorphic dewatering reactions, perhaps involving zeolite [Peacock *et al.*, 2005].

For all of the tested models, slip extends to the boundaries of the network. Thus, slip beyond the network boundaries may have occurred, undetected by the network, and my models should be considered minimum estimates of moment and extent of rupture. Planned increases in station coverage will enhance resolution of future events, but may not completely eliminate this bias.

3.6.3 Correlation of Slow Slip and Tremor

In general, the GPS stations closer to the coast experience slip earlier than the landward stations (Table 3.2a). While the timing of the earliest slip initiation at the coastal stations is in good agreement with tremor commencement, both around May 17 (Julian Day 137), the earliest tremor events and the LFEs embedded within them locate farther inland than these coastal stations. In other words, slip and tremor are temporally well correlated but not spatially well correlated. This is even more evident when comparing the tremor and LFE locations with the distribution of slow slip from the preferred inversion model (Figure 3.9). The conspicuous absence of any tremor or LFE sources beneath the southeast portion of the peninsula, where slip attains its maximum, is

partly due to the sparse seismic station coverage there (ACHA was not installed yet and LEPA experienced timing problems). The southern most stations, LEPA and PNCB, have lower signal to noise ratios due to their proximity to cultural and coastal noise. A lower signal to noise ratio at these stations compared to those in the northwest might obscure small tremor episodes. At this time I can not rule out the possibility that tremor events are similarly robust in the southeast region of the study area; however, since tremor sources located in the northwest portion of the peninsula are frequently recorded at the southern stations (Figure 3.8b) tremor sources originating in the southeast are likely of smaller magnitude than those in the northwest.

The tremor time series (Figure 3.3) shows three distinct pulses each lasting between 4-6 days with intervening quiet periods of approximately 20 days. The temporal resolution of the tremor is greater than the slow slip and if tremor and slip are temporally linked, the tremor time series suggests the possibility that slow slip proceeded in three distinct phases. The first phase, occurring between May 17th and 22nd (JD 137-142), is associated with the most energetic tremor, averaging over 3 hours of tremor per day. The later two phases (June 13-17 or JD164-168 and July 7-9 or JD188-190) consist of tremor averaging less than 1 hour of tremor per day. The absence of a close spatial association between slow slip and LFEs within tremor has been reported for ETS in both northern Cascadia [*Brown et al.*, 2009] and SW Japan [*Shelly et al.*, 2007a]. If tremor and slow slip are manifestations of the same process, the existence of tremor outside regions of slow slip maxima likely reflects areas experiencing smaller amounts of slip that are below the detection threshold of the GPS.

LFEs within tremor in Costa Rica locate on or near the plate interface in the depth range of 30-45 km, corresponding to the down dip frictional stability transition, and near the intersection of the continental Moho and the down going slab [Brown *et al.*, 2009]. This is also true of tremor at the Cascadia and SW Japan subduction zones; however, at these locations LFEs also correlate with areas of elevated V_p/V_s that are interpreted as regions of high fluid pressure at or near the plate interface, perhaps from dehydration reactions [Shelly *et al.*, 2006; Audet *et al.*, 2009]. At the Cascadia and SW Japan subduction zones, tremor occurs where the plate boundary interface attains a temperature of 450-550° C [Hyndman and Wang, 1995; Hacker *et al.*, 2003], the temperature at which fluids are released into the overlying crust from the basalt to eclogite reaction. In Costa Rica, tremor occurs at comparable depth but at much lower temperature between 200-250° C [Hacker *et al.*, 2003] suggesting that if fluids are required for tremor generation, lower grade metamorphic dehydration reactions must be involved.

3.6.4 Strain Accumulation and Seismic Hazard

Norabuena *et al.* [2004] used geodetic data from 15 campaign GPS sites to invert for the locking pattern on the plate interface under the Nicoya Peninsula. These authors used campaign GPS to estimate an interseismic velocity field, and a back slip model [Savage, 1983] to define a locked patch centered at 14 ± 2 km depth, locked at ~65% of the convergence rate. Since campaign GPS data lack the temporal resolution of CGPS and hence misses slow slip events, it is possible that this locked patch is (or was) fully locked, e.g. the inferred interseismic velocities determined by campaign GPS

underestimate the true interseismic velocity. The new CGPS network eliminates this temporal aliasing.

A comparison between the interseismic velocity field found in this study and *Norabuena et al.* [2004] is shown in Figure 3.15. The two velocity fields are similar, except that the magnitude (rate) tends to be higher for the continuous network data. Comparing the average velocity at two coastal stations from each network (GRZA and INDI from this study and SAMA and INDI from *Norabuena et al.*, [2004]) the campaign measurements appear to underestimate the interseismic velocity by about 12.7 mm/yr, or about 33%. Thus, the patch locked at 60% of the convergence rate found by *Norabuena et al.*, [2004] at 14km depth likely represented a fully locked patch.

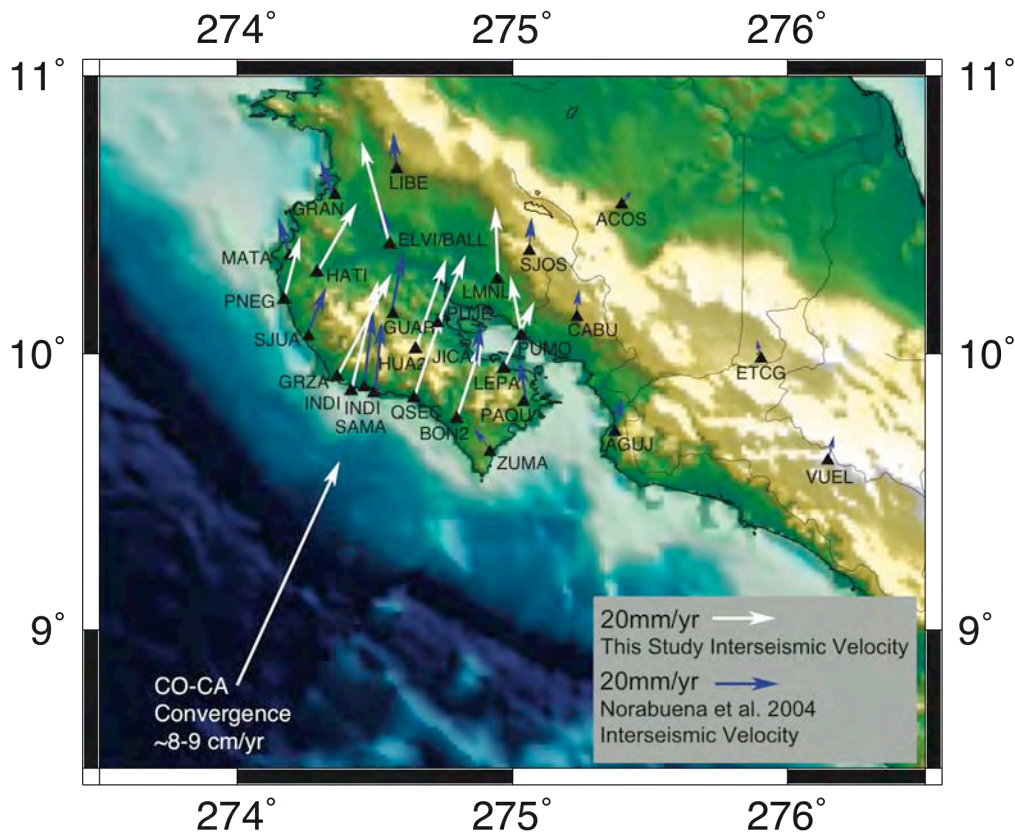


Figure 3.15. Interseismic velocity fields from this study (white vectors) and from *Norabuena et al.* [2004] (blue vectors).

Given the 42-44 month recurrence interval described above, and the observation window defined by the campaign measurements of *Norabuena et al.* [2004] (February 1994 to February 2000) it is possible that there were as many as two TSEs during the time frame encompassed by the campaign data. This could account for the entirety of the 12.7 mm/yr deficit in the interseismic velocity estimated by the campaign measurements.

A comparison of the preferred model for slip distribution found by this study beneath the Nicoya Peninsula, to the locking pattern found in the regional study of *LaFemina et al.*, [2009] shows that the areas of maximum slip are adjacent to areas of maximum locking (Figure 3.16). Conversely, areas of high slip are coincident with regions of lower locking. This is particularly true of model 3 from *LaFemina et al.*, [2009] in which there are no model constraints on locking from the Northern boundary of the Nicoya Peninsula to the southern model boundary.

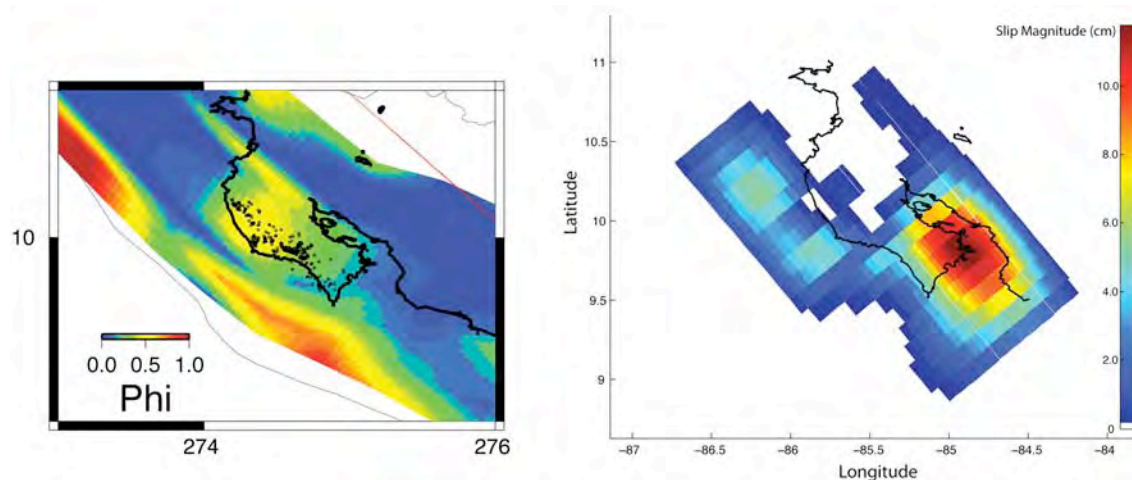


Figure 3.16. Interseismic locking pattern from *LaFemina et al.*, [2009] model 3 (left) compared to the inversion results from the preferred model of this study (right).

There have been three $M_w \geq 7$ earthquakes in the vicinity of the Nicoya Peninsula in the last 50 years [*Protti et al.*, 1995]. The magnitude and therefore rupture area of the 1950 event ($M_w = 7.7$) was significantly larger than that of the 1978 ($M_w=6.9$) and 1990

earthquakes ($M_w = 7.0$). The recurrence interval for a large 1950 type events is believed to be about 50 years based on the previous two large events occurring in 1852 and 1900 [Protti *et al.*, 1995]. Norabuena *et al.* [2004] speculated that a future 1950 type Nicoya earthquake might be smaller than its 3 predecessors due to the occurrence of the 1978 event, the presence of abundant microseismicity and the apparent lack of locking in much of the 1950 rupture area. However, Protti *et al.* [2001] show that the 1978 earthquake only released 15% of the potential slip accumulated prior to the event and therefore its potential contribution to the reduction of the size of the next Nicoya, 1950-style event is small. Based on the geometry of the rupture patterns of the earthquakes as well as the locked patch found by Norabuena *et al.* [2004] and the slipped patch found in this study (Figure 3.17), it seems likely that the location of these TSE patches will impact the geometry of future earthquake ruptures. However, a more comprehensive study will have to be completed to confirm this idea. In particular, better spatial constraints on the size and geometry of the TSEs, and better constraints on the frequency of these events will be required.

3.7 Conclusions

I have presented the first comprehensive study providing both geodetic and seismic evidence for the existence of tremor and slip events on the Cocos-Caribbean subduction zone segment of the Middle America Trench. I have found as follows:

1. A slow slip event, accompanied by seismic tremor was captured on continuous GPS and seismic networks on the Nicoya Peninsula, Costa Rica beginning in May 2007.

2. The best fitting preferred model for slip distribution of this tremor and slip event consists of 2 patches of slip, with a maximum of 11.8 cm of slip centered at ~30 km depth, near the down dip transition from stick-slip to stable sliding. A second patch of slip, with a maximum of ~5 cm of slip, locates up dip from the microseismicity and likely occurs at the up dip frictional transition.
3. Slow slip and tremor are temporally well correlated but lack a close spatial association.
4. In Costa Rica, slow slip and tremor occur in regions on the plate interface where thermal models predict temperatures at least 200° cooler than in Cascadia and SW Japan, suggesting that temperature is not a controlling factor for slow slip or tremor generation. However, if fluids sourced from dehydration reactions are required for tremor generation lower grade metamorphic reactions (e.g. involving lawsonite blueschist) must be important.

Further study and understanding of these events may help to explain why the slip deficit from the 1950 Nicoya earthquake has not yet been recovered.

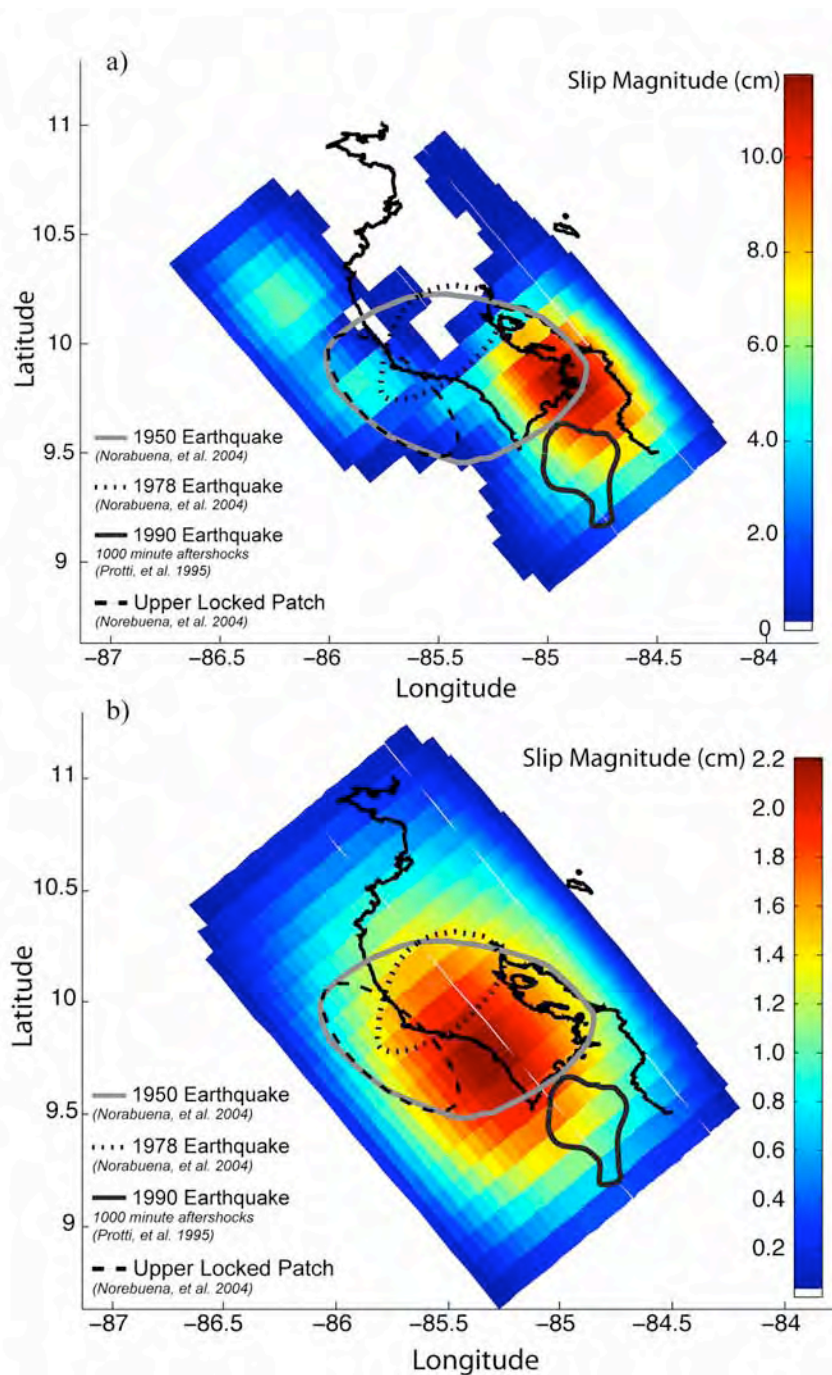


Figure 3.17. Comparison of the preferred slip mode for the 2007 event, rupture area of the 1950 $M_w=7.7$ earthquake (grey ellipse), the 1978 $M_w=7.0$ earthquake (black dotted ellipse) and the 1990 $M_w=7.0$ earthquake as defined by the 1000 minute aftershocks of Protti et al. [1995] (black ellipse) and locked patch previously identified by Norabuena et al. [2004] (black dashed ellipse). a) Station-optimized timing parameters, weighted inversion, $wrms=4.5$ mm. b) Station-optimized timing parameters, weighted inversion, $wrms=8.2$ mm.

CHAPTER 4

Improved Interseismic Velocity Field and Locking Pattern Studies for the Nicoya Peninsula, Costa Rica

4.1 Overview

A simple conceptual model for the earthquake cycle stipulates that strain accumulates during the interseismic period at a constant rate. Eventually, when a critical level is reached, frictional resistance is overcome, and strain is released by an earthquake. Observations over the last few decades have led to modification of this simple model, including the discovery of slow slip events [*Dragert et al.*, 2001; *Kostoglodov et al.*, 2003; *LaFemina et al.*, 2009; *Larson et al.*, 2004; *Melbourne et al.*, 2005]. The interseismic portion of the earthquake cycle is the period of time between large earthquakes, where strain accumulates on a frictionally coupled, or “locked”, fault plane. It is possible for the fault plane to be fully locked, whereby none of the driving plate rate translates to slip. However, it is also possible for the fault plane to be partially locked, whereby some fraction of the convergence rate accumulates as strain, while the remainder releases as slip. The surface displacement rate or velocity field is directly related to the percentage of locking on a fault plane. A spatially and temporally dense surface velocity field can determine the locking pattern on the fault plane.

The surface velocity field can be measured using a GPS network, like the one deployed on the Nicoya Peninsula (Figure 4.1). The interseismic velocity field is calculated using position time series observations measured by this network. Constrained inversions of these data are then used to infer the amount of locking on the subduction interface.

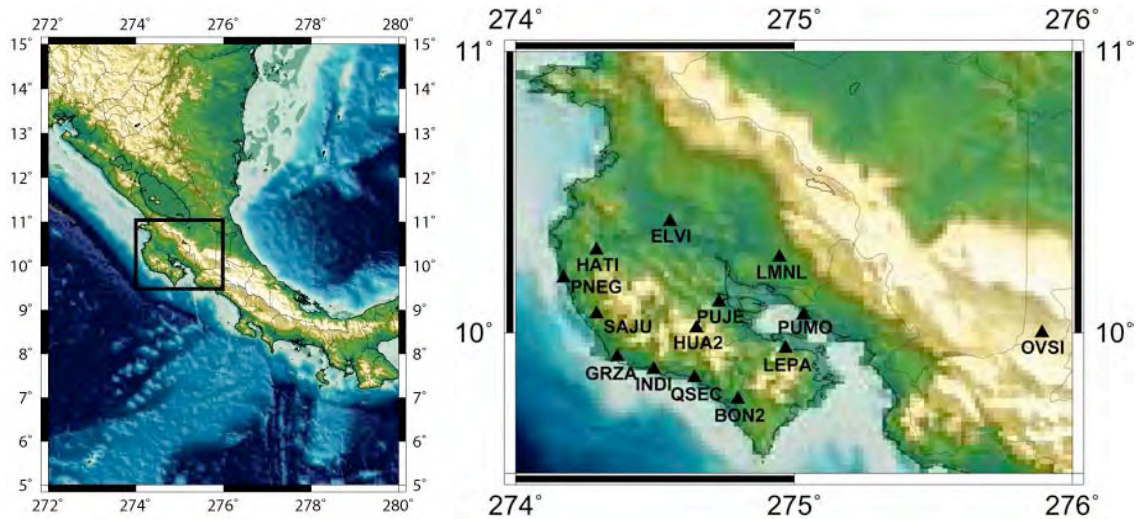


Figure 4.1. Map of Central America with an inset of the Nicoya Peninsula and the Continuous GPS network.

There have been several studies investigating the pattern of coupling on the plate interface beneath the Nicoya Peninsula. *Lundgren et al.* [1999] estimated, from inversion of GPS data, that there was heterogeneous locking beneath the Nicoya peninsula, reaching a maximum of 80% locking in the central and southeast region of the peninsula. *Norabuena et al.* [2004] used geodetic data from 15 campaign GPS sites to invert for the locking pattern on the plate interface beneath the Nicoya Peninsula. These authors defined locked patches centered at 14 ± 2 km depth, locked at $\sim 65\%$ of the convergence rate, and at 39 ± 6 km, locked at $\sim 50\%$ of the convergence rate. The two patches straddle the up-dip and down-dip limits of the seismogenic zone presented by *DeShon et al.* [2006].

LaFemina et al. [2009] present a study that models a GPS velocity field from El Salvador to Northern Panama. They use continuous and campaign GPS measurements to invert for coupling. *LaFemina et al.* [2009] present four versions of models, varying coupling constraints and block boundaries. All four models indicate spatially

heterogeneous coupling beneath, and off shore of, the Nicoya Peninsula, with the highest coupling values concentrated in central Nicoya, and averaging approximately 50% coupled.

Due to data limitations, none of the GPS studies described above account for the presence of slow slip, or Episodic Tremor and Slip events, such as the one described in Chapter 3, which may periodically and/or aseismically change the amount and pattern of strain. The measurements in these earlier studies would, in effect, average over this signal and should therefore be considered minimum estimates of coupling.

The occurrence of slow slip events within a time series of campaign geodetic data can affect the estimates of interseismic velocity. This chapter presents a revised interseismic velocity field that avoids the temporal aliasing of previous studies, by properly accounting for slow slip events. I also present inversions for locking on the fault plane using this revised velocity field.

4.2 Geologic Background

The Pacific coast of Costa Rica lies along the Middle America Trench, where subduction occurs between the Cocos and Caribbean plates. Due to its complex tectonic history, characteristics of Cocos-Caribbean subduction are highly variable along the subduction plate boundary. For example, the Cocos and Caribbean plates are undergoing high but varying rates and obliquity of convergence, ranging from orthogonal convergence at 9.1 cm/year in southern Costa Rica, to 25° counter-clockwise convergence at 7.6 cm/yr off shore Nicaragua. At the latitude of the Nicoya Peninsula convergence rates are ~8.5 cm/yr, oriented at 10° counter-clockwise from the trench

normal [DeMets, 2001]. Oblique subduction has been cited as a contributing factor to the complex tectonics observed in Costa Rica, including along the Nicoya Peninsula [LaFemina *et al.*, 2009; Sak *et al.*, 2009].

In addition, two types of sea floor are being subducted beneath the peninsula. Subducting oceanic crust is formed at two spreading centers. The East Pacific Rise (EPR) to the west (Figure 1.2), a fast spreading center, has produced smooth oceanic crust [Hey, 1977]. The Cocos-Nazca spreading center (CNS) to the south (Figure 1.2) began as a fast spreading center, producing smooth oceanic crust (CNS-1). At 19 Ma the CNS ridge jumped, transferring the CNS-1 crust from the Nazca Plate to the Cocos Plate and rotating the spreading center 22° to the East. This jump transitioned the spreading center to a slower spreading rate, creating crust with higher topographic relief (CNS-2) [Meschede *et al.*, 1998]. The Cocos-Nazca spreading center continues to undergo small southward jumps, forcing counterclockwise rotation of the Cocos Plate [Barckhausen *et al.*, 2001]. This series of ridge jumps and topographic variation of the oceanic crust impacts Cocos-Caribbean subduction in several ways, including creation of frictional asperities on the slab interface, variable heat flow and temperature profiles of the down going slab, and variable subduction fluid migration.

CNS-2 crust to the south, is ~40% covered with seamounts, including the Quepos Plateau and the Fisher Seamount, which transitions to a smooth down going slab beneath the Nicoya Peninsula further North [von Huene *et al.*, 1995; Hinz *et al.*, 1996]. The delineation between rough and smooth ocean bottom topography corresponds to the boundary between CNS-1 crust and CNS-2 crust, which is overprinted by Galapagos hot spot volcanism. The CNS-1/CNS-2 boundary intersects the Central American isthmus

near the southern tip of the Nicoya Peninsula and is demarcated by the location of the Fisher Seamount [*Hinz et al.*, 1996; *Von Huene et al.*, 2000; *Barckhausen et al.*, 2001].

The morphology of the down going slab impacts the upper plate tectonics [*Gardner et al.*, 1992; *Fisher et al.*, 1998; *Von Huene et al.*, 2000; *Gardner et al.*, 2001; *Fisher et al.*, 2004; *Sak et al.*, 2004] and may also impact the nature of earthquake rupture along the margin [*Bilek et al.*, 2003].

There is an appreciable change in the slab dip, age and thermal structure, also related the genetic history of the Cocos Plate. The dip variability beneath Nicaragua and Costa Rica can be shown by seismically illuminating the Wadati-Benioff zone [*Protti et al.*, 1995a] and by imaging depth to top of basement [*Protti et al.*, 1995a; *Von Huene et al.*, 2000]. The dip of the Wadati-Benioff zone shallows from north to south, with a distinct bend at the Nicaragua-Costa Rican boarder, from 84° to 60°. There is also evidence of a steep bend, the Quesada Sharp Contortion, inboard of the Southern tip of the Nicoya Peninsula at a depth >70km; the tear is revealed by offset surface projection of the slab depth contours by ~15 km [*Protti et al.*, 1995a]. This tear lies very close to, if not on, the extension of the demarcation between CNS-1 and CNS-2 crust and the rough-smooth bathymetry boundary. This offset in the down going slab may be related to the age and or smoothness of the slab [*Protti et al.*, 1995a]. CNS-2 crust to the SE is younger (18-19 Ma), more buoyant, and has a rougher topography than the CNS-1 crust to the NW (21-23 Ma) [*Hey*, 1977; *Von Huene et al.*, 2000; *Barckhausen et al.*, 2001]. There is no evidence of the Wadati-Benioff zone beneath the Osa Peninsula below 50 km [*Protti et al.*, 1995a; *Husen et al.*, 2002]. The age of the down going slab is between 15 and 16 Ma [*Barckhausen et al.*, 2001], most likely related to Cocos Ridge collision.

Oceanic crust cools as it ages and moves away from the ridge crest, resulting in a heat flow distribution that is proportional to the square root of the age of the crust. It follows, that if the age of the down going CNS-1 crust (21-23 Ma [Barckhausen *et al.*, 2001]) is younger than the down going EPR crust (24-25 Ma [Hey, 1977; Barckhausen *et al.*, 2001]), the heat flow of the CNS-1 crust is expected to be higher than that of the EPR crust. Spinelli *et al.* [2006] demonstrate that not only is the heat flow of the CNS-1 crust higher, averaging about 105 mW/m^2 , but also that the modeled isotherms in the overriding plate in southern Nicoya have a steeper gradient than those in the northern Nicoya Peninsula, where the EPR crustal heat flow values are only 20 mW/m^2 . Hutnak *et al.* [2007] attributes lower heat flow in the EPR crust to higher incidence of hydrothermal cooling through seamounts and other outcrops seaward of the trench. Seamounts are more common on EPR generated crust than CNS-1 crust, which has no identified seamounts.

4.3 Previous Work on Temporal and Spatial Variability

While the simplest model for the earthquake cycle postulates uniform ruptures that repeat at regular intervals, it has long been known that there can be considerable spatial and temporal complexity. For example, the Parkfield segment of the San Andreas Fault has been cited as one example of a more periodic fault segment, having a recurrence interval of 22 years for M5-6 earthquakes [Bakun and McEvilly, 1984]. Bakun and McEvilly [1984] also predicted that there was a 95% chance of a M5-6 earthquake occurring on the Parkfield segment by 1993, however one did not occur until September 2004. This 2004 earthquake also nucleated in a different location from the

two prior 1934 and 1966 earthquakes. *Murray and Segall* [2005] attribute this loci shift to transient slip unloading the area of the 1934 and 1966 earthquakes, and loading and triggering the 2004 quake.

For decades there have been studies analyzing earthquake statistics that focus on identifying seismic gaps and determining the slip deficit (related to the magnitude of the next earthquake) and which portion of a fault zone will rupture next. It is possible to statistically determine the likelihood of rupture, and the minimum or maximum magnitude of the rupture given certain assumptions. For example, *Nishenko* [1991] gives earthquake statistics and identifies areas with seismic gaps, for plate boundaries of the Pacific rim. They present statistical probability for a rupture of a certain magnitude, on a certain segment of plate boundary, within the next 5, 10 and 20 years. Estimates are based on:

- 1) *Historic and instrumental record of large and great earthquake recurrence.*
- 2) *Paleoseismic evidence of recurrence from radiometric dating of Holocene features produced by earthquakes.*
- 3) *Direct calculations of recurrence time from the size of the most recent characteristic event and the long-term rates of plate motion assuming the validity of the time-predictable model for earthquake recurrence.*
- 4) *Application of a log-normal distribution for the recurrence times of large and great earthquakes [Nishenko, 1991].*

As an example, *Nishenko* [1991] identified the Nicoya Peninsula as a seismic gap and predicts that it has a 98% chance of rupturing with a magnitude 7.3 earthquake by the year 2009. This was published in 1991 and to date no large earthquake has occurred along the Nicoya segment of the plate boundary. This illustrates the point that while it is possible to apply statistics to the earthquake cycle, the accuracy of even a 20-year prediction is not reliable. Much more than our current understanding would be required to achieve refined prediction precision within days or weeks and 10's of kilometers.

The assumptions inherent in the statistical technique include that all of the energy is released elastically in sequential earthquakes. This is a limiting assumption. There is a spectrum of energy release on a fault, ranging from purely episodic stick slip to continuous aseismic creep. There are then deviations from these end members, including interseismic microseismicity, and transient aseismic slip. Tremor and/or low frequency earthquakes sometimes accompany transient slip events. The existence of these tremor and slip events shows that there is indeed deviation from the first order understanding of tectonic energy release. In order to fully understand the effect of these events, they must be monitored through more than one earthquake cycle to determine their temporal pattern.

Slip deficit studies do not take into account spatial variability of the asperities that have been identified as a potential cause for the nucleation of earthquakes. A common theme in all earthquake prediction models is the existence of alternating strong and weak spots that persist throughout the earthquake cycle. These weak spots slip aseismically though out the interseismic period, loading the stronger areas (asperities). The earthquake results when these strong areas reach a critical stress state and rupture. In order to properly predict the location of the next earthquake, the location and behavior of these patches would have to be fully understood.

An understanding of the location and behavior of asperities begins with an understanding of why they might exist in any given location. In general the location of these asperities may be determined by temperature and pressure controlled metamorphic phase changes in the down going slab [*Peacock and Wang, 1999; Peacock et al., 2002; Peacock, 2003; Peacock et al., 2005*] or in dewatering of the sediments on top of the

down going slab [*Saffer et al.*, 2000; *Saffer*, 2003; 2007; *Spinelli and Saffer*, 2004].

These reactions can release volatiles (H_2O and CO_2) that increase pore fluid pressure, and dictate the critical stress condition that can result in asperity rupture.

Another explanation for the location of asperities is often topography of the down going slab. In areas where topography is variable, the asperities are located around areas of higher topography where coupling and friction would be high, while the weaker areas are located around areas of lower topography where coupling and friction would be low. This implies, that in order to accurately predict where an earthquake might occur, beyond simply where the last earthquake was, an understanding of the subduction zone isotherms and down going slab morphology is essential.

Temporal variability of these asperities is also important to understand and may not be consistent between faults or even between different segments of the same fault. *Hirose and Hirahara* [2002] present a suite of numerical models that show that the relative dimensions of an asperity may have a great deal to do with whether the entire asperity ruptures or only part of the asperity ruptures. In addition, *Schwartz* [1999] demonstrates that the pattern of rupture from one earthquake to the next on the same portion of a fault zone can vary greatly. This was shown in the Aleutian Islands, Kuril Islands, Solomon Islands earthquakes, and northern Honshu Japan. In contrast *Zweck et al.* [2002] show that the locked portion of the plate boundary beneath the Kodiak Islands in Alaska corresponds directly to the rupture region of the 1964 earthquake. They suggest that this implies that asperities in this region repeat from one earthquake cycle to the next. This suggests that these concepts cannot be categorically applied to different regions of the world, but rather, need to be understood for each region independently.

Hence, it is important to study the nuances of a particular fault segment with a network that collects both spatially and temporally dense data, such as the ones deployed on the Nicoya Peninsula, Costa Rica.

4.4 Improved Surface Velocity Fields

Previously published interseismic velocity fields do not account for the occurrence of slow slip events (chapter 3). If such an event occurred during the observation period, the surface velocity estimates will be less than the actual velocity. The amount of interseismic locking will also be underestimated. Having identified the slow slip event in 2007, it is now possible to estimate a more accurate interseismic velocity field that accounts for these events. There are several possible ways to estimate this velocity field: fitting a straight line to position estimates defined in either the International GNSS Service Reference Frame (IGS), or the baseline estimation (relative to station MANA), and using the hyperbolic tangent model for interseismic velocity estimation described in Chapter 3. Each of these will be discussed in further detail below. In the first two approaches, knowledge of the occurrence of the slow slip event is used to define a time period when the position data are unaffected by the Tremor and Slip Event. In the last approach the slow slip event parameters and the interseismic velocity are estimated simultaneously.

4.4.1 IGS Straight Line Interseismic Estimation

The first approach for estimating the interseismic velocity field was done using time series relative to the IGSb-00 reference frame. A straight line was fit to a window of

the time series found to be between slow slip events. The resulting velocities are subsequently rotated to a stable Caribbean Plate reference frame. The advantages of this method are its simplicity and that no assumptions are made regarding the consistency of velocity before and after the slow slip event.

Upon inspection of the GPS time series a potential slow slip was identified in late 2008 at the three northern most stations (PNEG, HATI, and ELVI). The event was confirmed by tremor activity in August of 2008 (*S. Schwartz personal communication*). Thus, the window of time for the straight line fit was conservatively restricted to prior to the potential event in 2008 and after the event in 2007 (chapter 3). Restricting the time series to the period between two slow slip events allows for examination of the assumption that the interseismic velocity remains constant before and after an event. This provides a time series of more than a year for each station, except SAJU. The velocity estimates at SAJU are restricted to 2 months (from when the station came online until the potential 2008 event), which is reflected in the larger uncertainties at that station. The uncertainties for the resulting north and east velocities were determined using the methods described in *Dixon et al.* [2000] and *Mao et al.* [1999]. To determine the uncertainty, the Weighted Root Mean Squared (WRMS) of the fit of the straight line to both the north and east component of motion is applied using the following series of formulas.

$$\sigma_w(N) = 0.613[WRMS(N)] + 0.259 \quad (4.1)$$

$$\sigma_w(E) = 0.767[WRMS(E)] - 0.182 \quad (4.2)$$

$$\sigma_f(N) = 1.139[WRMS(N)] + 0.117 \quad (4.3)$$

$$\sigma_f(E) = 1.041[WRMS(E)] - 0.342 \quad (4.4)$$

where σ_w is the white noise, assumed to be time independent, σ_f is the flicker noise, a type of time correlated noise whose power varies as the inverse of the frequency. These values are then used in the formula for the overall rate uncertainty:

$$\sigma_r^2 \equiv \frac{12\sigma_w^2}{gT^3} + \frac{a\sigma_f^2}{g^bT^2} + \frac{\sigma_{rw}^2}{gT} \quad (4.5)$$

where g is the number of observations per year, T is the length of the time series in years, a and b are empirical constants, equal to 1.78 and 0.22 respectively, and σ_{rw} is the random walk noise. The value of random walk noise is assumed to be zero, because all of the monuments and instruments are approximately 5 years old or better and very well stabilized to the ground (usually in bed rock).

Once the velocities and uncertainties are determined for the ITRF velocities between mid 2007 and late 2008, the entire velocity field was rotated to a stable Caribbean Plate reference frame using the 9-site geodetic Euler vector calculated for Lopez *et al.* [2006]. The resulting velocities are reported in Table 4.1 and shown in map view in Figure 4.2.

Table 4.1. Velocity field from ITRF velocity straight line fit rotated to stable Caribbean plate reference frame.

Site	Lat	Lon	North Velocity	East Velocity	σ_N	σ_E
BON2	9.7644	-85.2025	17.10	10.50	2.08	3.6
ELVI	10.3944	-85.4458	24.06	0.49	2.52	6.63
GRZA	9.9153	-85.6356	32.54	16.04	1.60	2.91
HATI	10.2919	-85.7097	17.27	2.16	1.86	3.08
HUA2	10.0175	-85.3517	17.75	8.83	1.88	3.30
INDI	9.8644	-85.5853	27.13	9.97	1.92	3.14
LEPA	9.9453	-85.0311	14.90	5.27	2.02	3.77
LMNL	10.2675	-85.0531	14.03	2.18	2.13	3.63
PNEG	10.1953	-85.8289	16.88	6.15	1.80	3.27
PUJE	10.1100	-85.2700	17.64	8.95	1.92	3.54
PUMO	10.0644	-84.9667	13.73	7.43	1.88	3.47
QSEC	9.8402	-85.3572	21.68	4.33	2.01	3.60
SAJU	10.0671	-85.7106	13.43	2.26	5.11	7.81

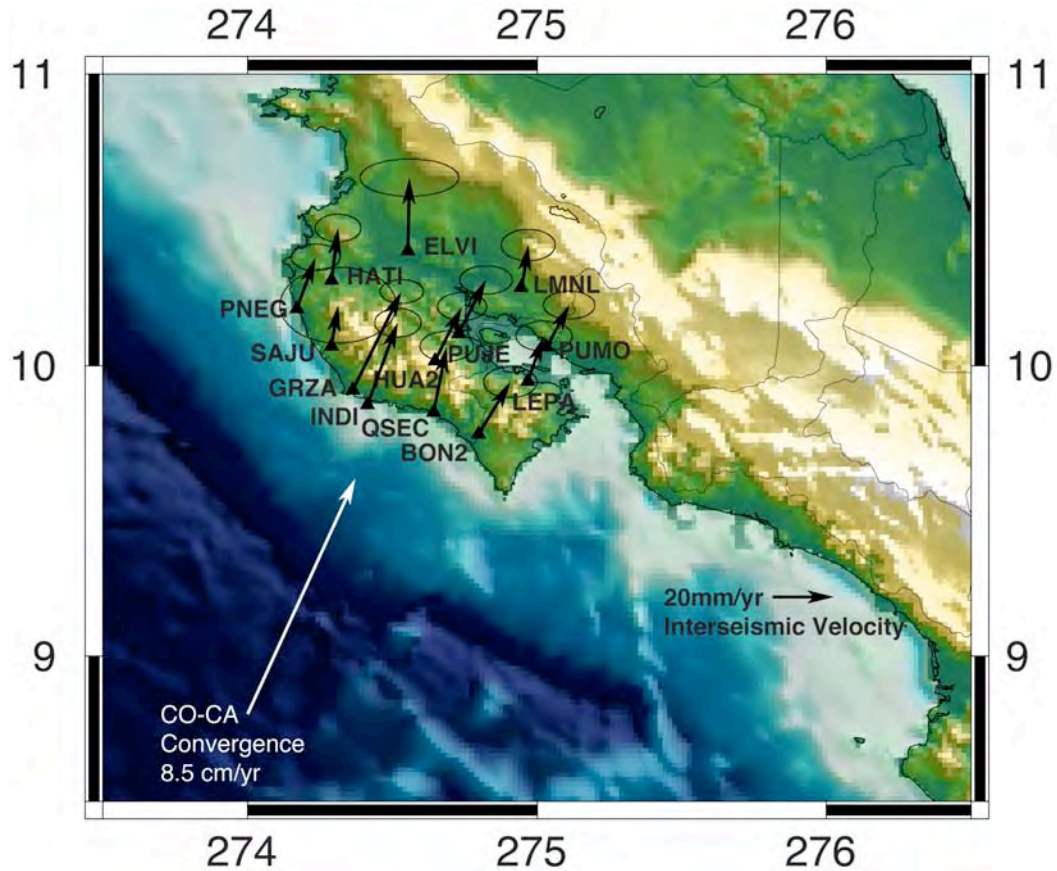


Figure 4.2. Interseismic velocity field estimated from IGSb-00 time series and a simple straight line fit for the time period between slow slip events. Error ellipses indicate 95% confidence intervals.

4.4.2 Baseline Straight Line Interseismic Estimation

Another approach to estimating the interseismic velocities between slow slip events involves using a baseline time series relative to GPS station MANA in Managua, Nicaragua, approximately 250 km north of Nicoya, Costa Rica. As in the previous approach, a straight line is fit to the time window between slow slip events. The advantage of this method is that calculating a baseline removes any common mode errors that may exist, allowing more accurate identification of slow slip events that may perturb

the interseismic velocity estimate. The disadvantage of this method is that, in this case, the baseline station (MANA) induces some noise into the time series. This disadvantage will likely be remedied by the recent installation of a new back arc GPS station (VERA) in July 2009.

For consistency, the time window used to estimate the interseismic velocity at each station is the same as that used for the ITRF based time series (from the end of the 2007 event to before the potential 2008 slow slip event). The uncertainties were calculated as described above in equations 4.1 through 4.5. Once the velocities were found relative to station MANA, the velocity field was rotated to a stable Caribbean Plate reference frame. To do this, the motion of MANA relative to the Caribbean Plate was found using the *Lopez et al.* [2006] pole reported above, and removing that motion uniformly from each station in the Nicoya network. The resulting velocities relative to a stable Caribbean Plate are presented in Table 4.2 and Figure 4.3 below.

Table 4.2. Velocity field from baseline to MANA time series using a straight line fit. Rotated to stable Caribbean plate reference frame.

Site	Lat	Lon	North Velocity	East Velocity	σ_N	σ_E
BON2	9.7644	-85.2025	18.37	12.33	2.00	6.82
ELVI	10.3944	-85.4458	25.81	8.10	3.33	11.19
GRZA	9.9153	-85.6356	31.44	19.02	1.90	6.11
HATI	10.2919	-85.7097	18.27	3.00	2.02	6.12
HUA2	10.0175	-85.3517	18.46	9.62	1.86	6.69
INDI	9.8644	-85.5853	27.62	10.77	1.91	5.97
LEPA	9.9453	-85.0311	17.76	6.57	4.22	7.53
LMNL	10.2675	-85.0531	15.58	4.33	2.06	6.91
PNEG	10.1953	-85.8289	16.80	8.41	1.94	5.85
PUJE	10.1100	-85.2700	18.14	12.62	1.70	6.52
PUMO	10.0644	-84.9667	15.22	7.63	1.86	6.49
QSEC	9.8402	-85.3572	22.40	5.17	2.19	6.20
SAJU	10.0671	-85.7106				

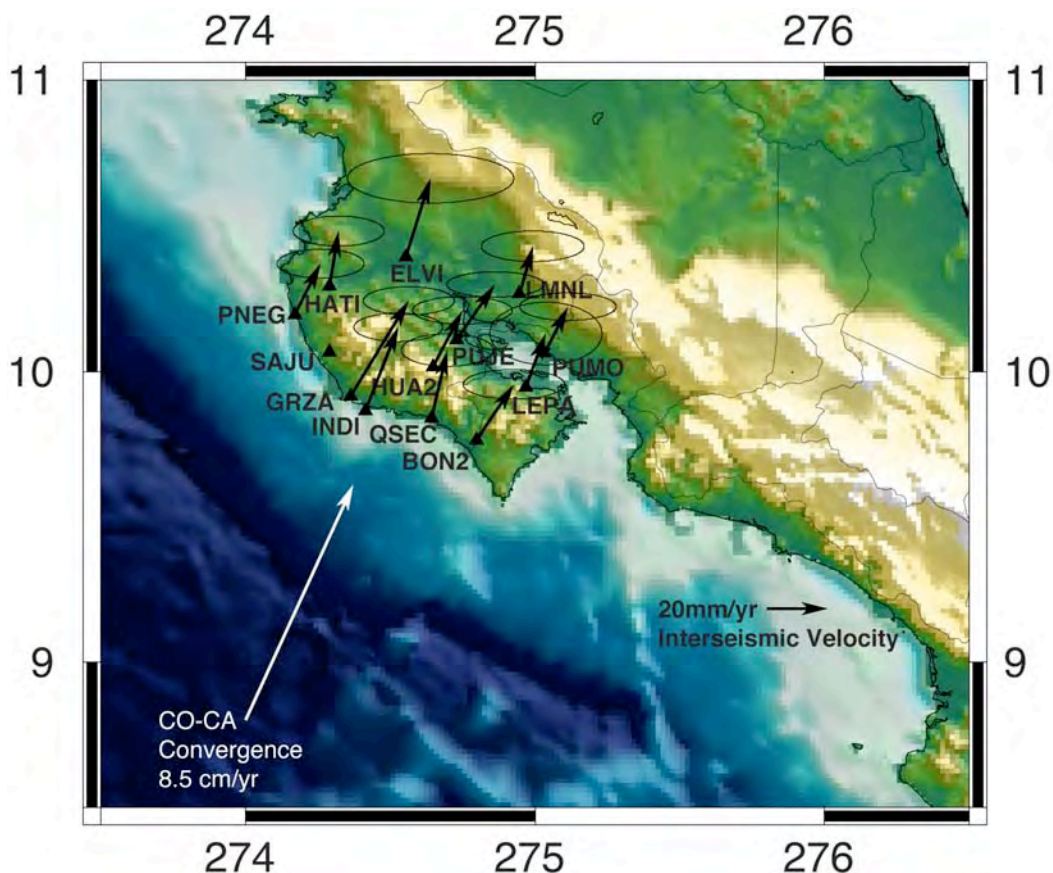


Figure 4.3. Interseismic velocity field estimated from MANA baseline time series and a simple straight line fit for the time period between slow slip events. Error ellipses indicate 95% confidence intervals.

4.4.3 Baseline Hyperbolic Tangent Interseismic Estimation

One disadvantage of the previous two methods is that the available time series to define the site velocity is short (~ 1 yr). Since GPS velocities are strongly dependent on total observation time, longer time series are preferable. The hyperbolic tangent model for slow slip events (Chapter 3) allows for velocity estimates from longer time series, spanning and directly accounting for the slow slip event. Baseline time series relative to GPS station MANA in Managua, Nicaragua are used. The event is characterized by fitting the hyperbolic tangent function of *Larson et al.* [2004] to the position time series:

$$X(t) = x_0 + Vt + \frac{U}{2} \left[\tanh \frac{t-T}{\tau} - 1 \right] \quad (4.6)$$

This five-parameter model includes the initial position (x_0), the background site velocity (V), assumed to be constant before and after the event, the event offset (U), the midpoint time of the event (T), and duration half width (τ). The timing parameters are constrained for both the north and east components to the values determined in *Outerbridge et al.* [2010], and the best fitting value for V is determined by non-linear least squares techniques. Since the *Outerbridge et al.* [2010] study was completed, more post event data has been collected, better constraining the velocity parameter. The time frame used to determine the interseismic velocity is from January 1, 2006 to August 7, 2008. These limits were established to eliminate the influence from coseismic and post seismic response of the October 9, 2004, M_w 6.9 Earthquake near the coast of Nicaragua (N 11.25, E -87.02) and the potential slow slip event beneath the Nicoya Peninsula in 2008. Thus, the only slow slip event in the data set is the 2007 event. The advantages of this method are that the length of the time series for some stations exceeds three years and common mode errors are (theoretically) reduced through the baseline calculation. The disadvantages of this method are that there is in fact more noise in the data than IGSb-00 time series, (reflecting problems with the MANA station), and this method assumes that the interseismic strain accumulation is constant before and after the slow slip event. This will be addressed below.

As before, the velocity field was rotated to be relative to a stable Caribbean Plate reference frame by removing the motion of MANA relative to the Caribbean Plate from each station in both the north and east component. The velocities estimated by this method for each station are reported below in Table 4.3 relative to a stable Caribbean

Plate and shown in Figure 4.4. The uncertainties for these velocities are calculated as described above.

Table 4.3. Velocity field from baseline to MANA time series using hyperbolic tangent fit. Rotated to stable Caribbean plate reference frame.

Site	Lat	Lon	North Velocity	East Velocity	σ_N	σ_E
BON2	9.7644	-85.2025	22.38	13.24	0.95	2.83
ELVI	10.3944	-85.4458	24.84	10.21	3.19	10.5
GRZA	9.9153	-85.6356	30.21	20.04	1.14	3.54
HATI	10.2919	-85.7097	16.04	4.66	1.11	2.98
HUA2	10.0175	-85.3517	20.23	14.30	0.84	2.58
INDI	9.8644	-85.5853	27.75	16.42	0.87	2.65
LEPA	9.9453	-85.0311	17.73	8.93	1.48	3.05
LMNL	10.2675	-85.0531	16.56	0.31	1.71	5.82
PNEG	10.1953	-85.8289	16.24	7.90	0.90	2.68
PUJE	10.1100	-85.2700	17.05	13.97	0.82	2.65
PUMO	10.0644	-84.9667	15.05	9.04	1.68	5.67
QSEC	9.8402	-85.3572	23.54	15.17	0.98	2.91
SAJU	10.0671	-85.7106				

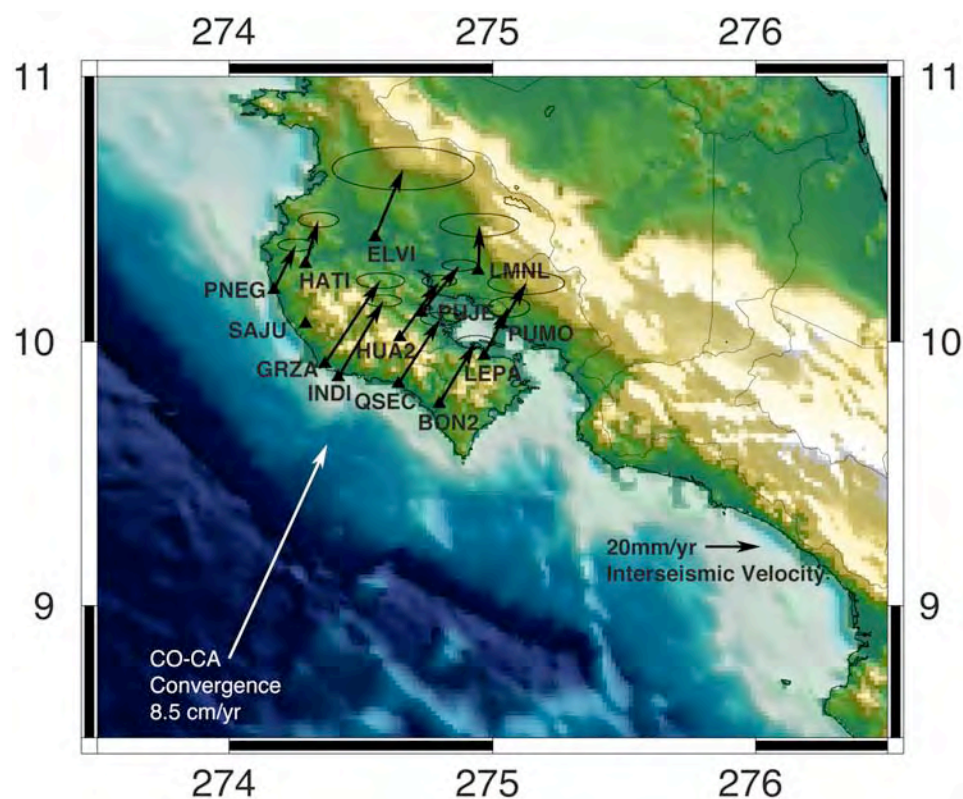


Figure 4.4. Interseismic velocity field estimated from MANA baseline time series and a hyperbolic tangent fit. Error ellipses indicate 95% confidence intervals.

The results of each method of velocity field estimation are very similar (Figure 4.5). The biggest differences are in the most inland stations where the time series are shortest. This is reflected in the larger uncertainties for these stations.

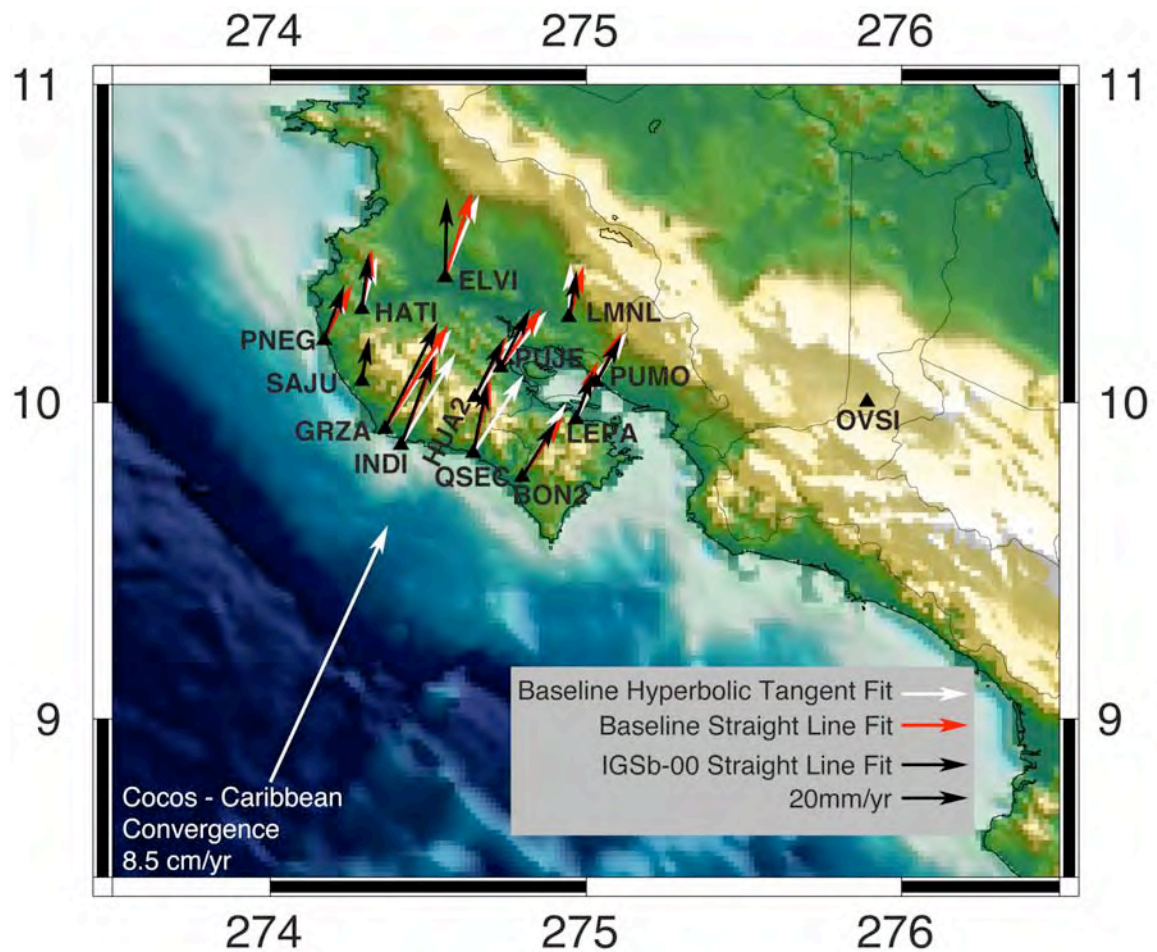


Figure 4.5. Interseismic velocity field estimated from all three methods; MANA baseline time series and a hyperbolic tangent fit (white), MANA baseline time series and a straight line fit (red), and IGSb-00 time series and a straight line fit (black).

4.5 Locking Pattern Results

A linear inversion [Funning *et al.*, 2005] based on the formulation of Okada [1985] is used to estimate the magnitude and distribution of locking on the fault plane,

using the surface velocities listed in Tables 4.1, 4.2 and 4.3. The inversion code creates Green's functions using a model for slip on a rectangular dislocation in an elastic half space.

As in Chapter 3, the plate interface is modeled as three adjoining rectangular dislocation planes using the geometry described in *Norabuena et al.* [2004] (Figure 3.10). From the trench to 15 km depth, the interface dips at 10° ; from 15 km to 38 km depth, the interface dips at 25° ; and from 38 km to 60 km, the interface dips at 43° . The strike of the fault plane is defined by the average orientation of the trench offshore, 320° . The length of each fault segment extends a total of 250 km centered on the Nicoya Peninsula to minimize possible edge effects. In order to represent variable, distributed slip on a large fault plane, the dislocations were meshed in 20 equal divisions along-strike and 15 equal divisions down-dip.

I constrained slip direction in the model to be an average of the azimuths of interseismic velocity vectors from the network data (280°). The variance from convergence direction is due to fore-arc sliver transport, as described previously. To avoid geologically unreasonable slip, Laplacian smoothing is imposed, and locking cannot exceed 100% of the plate rate (8.5 cm/yr). The data are inverted using a fast non-negative least squares algorithm [*Bro and De Jong, 1997; Funning et al., 2005*]. Best fitting inversion results for each velocity field (Figure 4.6) are determined by minimizing the WRMS, without achieving greater than 100% locking.

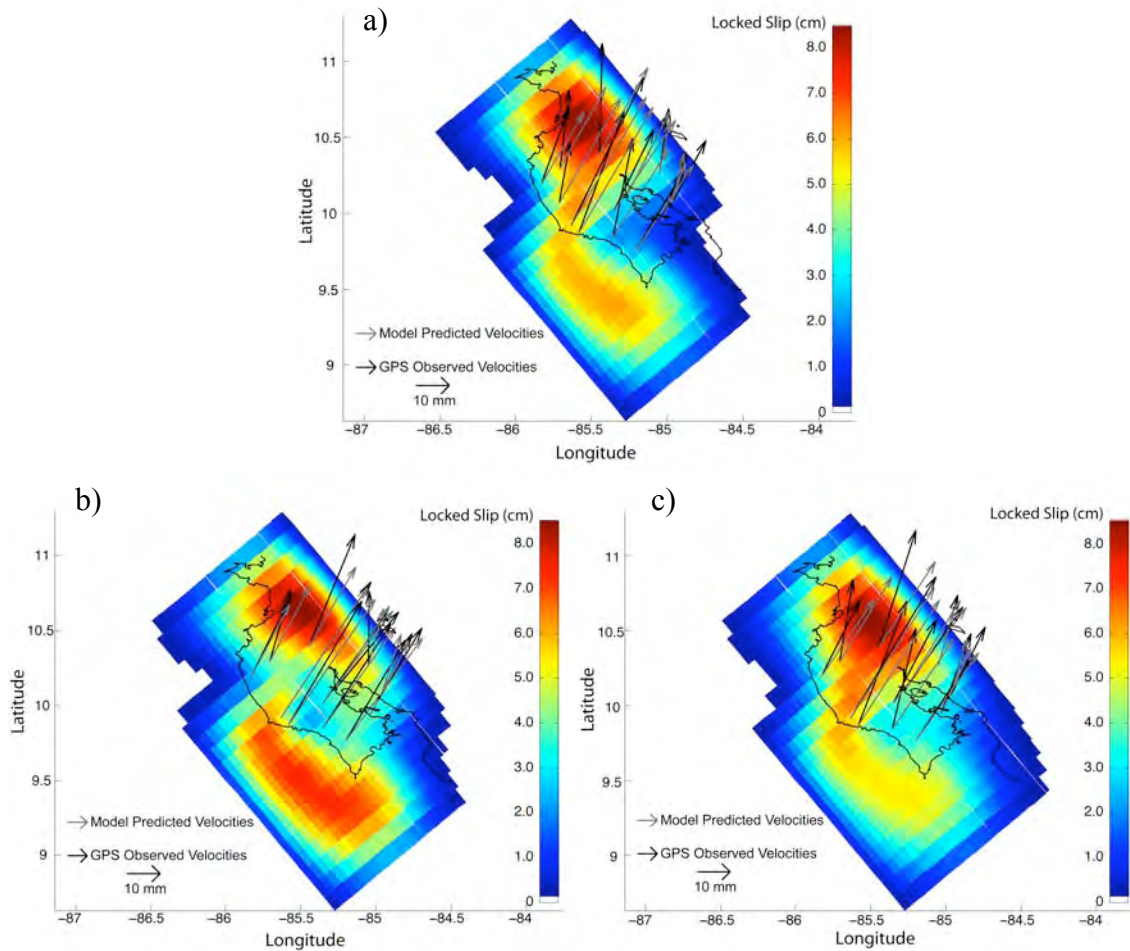


Figure 4.6. a) Best fitting inversion results for the ITRF based straight line fit velocity field ($w_{rms} = 5.89$ mm). b) Best fitting inversion results for the baseline based hyperbolic tangent fit velocity field ($w_{rms} = 2.58$ mm). c) Best fitting inversion results for the baseline based straight line fit velocity field ($w_{rms} = 4.94$ mm).

To confirm that the data can resolve the patterns of locking found by the inversions, a resolution test was completed following the procedures of *Funning* [2005] and *Biggs et al.* [2006] and outlined in section 3.5. The results of this resolution test are presented in Figure 4.7 and show that the model can easily resolve 100x100 km patches in the areas where the inversions indicate locking. The patches of locking found are roughly 100 km long down-dip and 150 km long along strike, suggesting that the data can resolve 2 separate patches of locking.

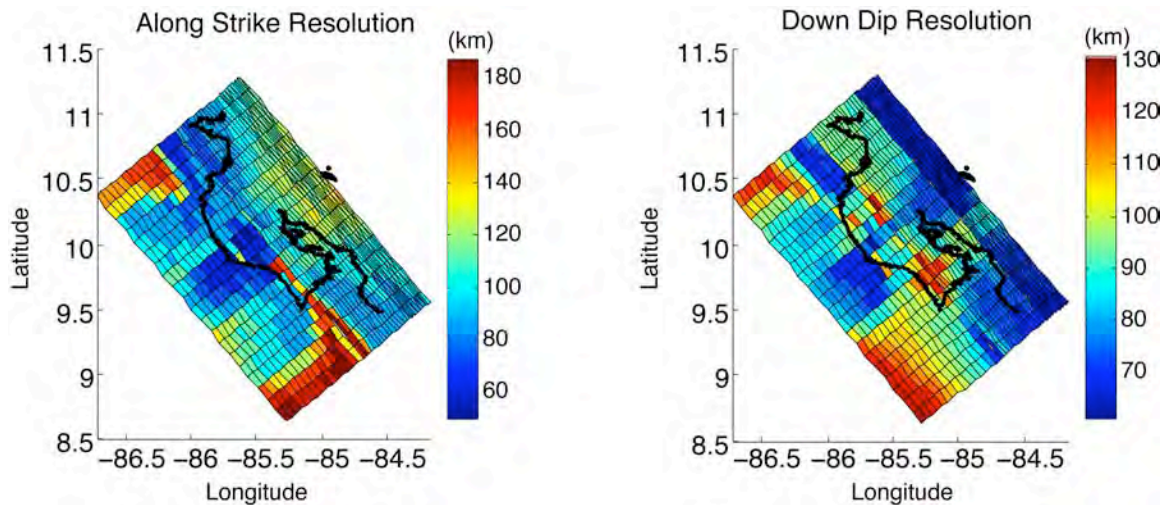


Figure 4.7. Along strike and down dip model resolution results, showing minimum resolvable patch size in km.

4.6 Discussion

4.6.1 Comparison to Other Interseismic Locking Studies

There have been several studies that have looked at the pattern of interseismic locking on the subduction interface beneath the Nicoya Peninsula, Costa Rica, including *Lundgren et al.* [1999], *Norabuena et al.* [2004], and *LaFemina et al.* [2009]. Since the studies of *LaFemina et al.* [2009] and *Norabuena et al.* [2004] both include the data presented in *Lundgren et al.* [1999], this portion of the discussion will be restricted to a comparison of this study to *LaFemina et al.* [2009] and *Norabuena et al.* [2004]. Both the *LaFemina* and *Norabuena* studies use interseismic velocity fields that do not account for, but could contain, slow slip events. Therefore, these studies may underestimate the interseismic velocity as well as the amount of locking on the fault plane, perhaps effecting estimation of size, location and timing of the next earthquake. There are three main results that can be compared from these three studies; the magnitude of locking, the spatial patterns of locking and, since these three studies cover different time spans of data, the temporal variability in locking.

Comparing the locations and magnitude of maximum locking, our inversion results consistently show two separate patches of locking, with varying degrees of locking. The location of the deeper patch intersects the location of the patch of 50% locking identified by model 3 of *LaFemina et al.* [2009]. In contrast to the *LaFemina et al.* [2009] study, the deeper, maximum locked patch found in this study is deeper, further north and consistently found to be 100% locked. As shown by *Outerbridge et al.* [accepted] and described in section 3.6.4 (Figure 3.15), Nicoya interseismic velocity fields that do not account for slow slip events can underestimate the true velocities by up to $\sim 1/3$. This could account for the lower percent of locking reported by both *LaFemina et al.* [2009] and *Norabuena et al.* [2004].

The up-dip patch of locking in my study is in approximately the same location as the shallow patch found by *Norabuena et al.* [2004] to be 65% locked. In contrast, inversion of the velocity fields in this study estimate locking for this up-dip patch in a range from ~ 65 -82% locked. Another difference between the interseismic locking distribution found by this study and that of *Norabuena et al.* [2004], is that in this study, the maximum locking is located on the deeper portion of the fault plane, whereas in the *Norabuena et al.* [2004] study, the greatest locking was found up-dip. This difference could reflect better data quality and temporal resolution in this study, or could be evidence of changing strain conditions.

Due to the differences inherent in comparing inversion results across different studies (data sets, fault and block geometries, inversion codes, boundary conditions, etc.), I took the velocity fields reported by *LaFemina et al.* [2009] *Norabuena et al.* [2004] and inverted them according to the inversion scheme and boundary conditions, described

above, with the exception that the data from the LaFemina study was modeled using a 300° slip constraint to be consistent with the velocity field from that study's data suite. In doing so, I also eliminated the vertical measurements of *LaFemina et al.* [2009] for consistency with this study and the *Norabuena et al.* [2004] study. *Norabuena et al.* [2004] report that the vertical measurements in their velocity field are too noisy to be of value. Some of the vertical measurements in this study are also quite noisy. In many cases the vertical motion is zero within uncertainty, indicating that the vertical measurements would not supply any additional information to the inversion. To remedy this situation in the future, a new baseline station, VERA, was installed in July 2009 in the back arc in Costa Rica. This will hopefully reduce the noise significantly. The results obtained by the inversion of the *LaFemina et al.* [2009] and *Norabuena et al.*, [2004] velocity fields (Figure 4.8) are virtually identical to those found by the respective studies both in magnitude and spatial distribution of locking (the maximum locking found in either case by this study is $\sim 53\%$).

Figure 4.8 also shows the IGSb-00 straight-line fit inversion and MANA baseline hyperbolic tangent inversion results as well as the time frame of the data sets covered by each study. Looking at the temporal comparison of the studies, the *Norabuena et al.* [2004] study covers the earliest time frame. The *LaFemina et al.* [2009] study uses all of the data from the *Norabuena et al.* [2004] study as well as additional data, increasing GPS coverage both spatially and temporally. The data set used in the current study uses new data, independent of the previous studies; however some of our permanent stations are located on or very near some of the campaign station sites used by the previous two studies. The different temporal windows covered by the various data sets, therefore

allows an assessment of possible strain migration. The locus of strain accumulation appears to migrate from up-dip and to the South to down-dip and to the North over time, as does the area of maximum locking. This suggests that strain accumulation patterns in this region are not consistent throughout a seismic cycle and can change on the decadal time scale.

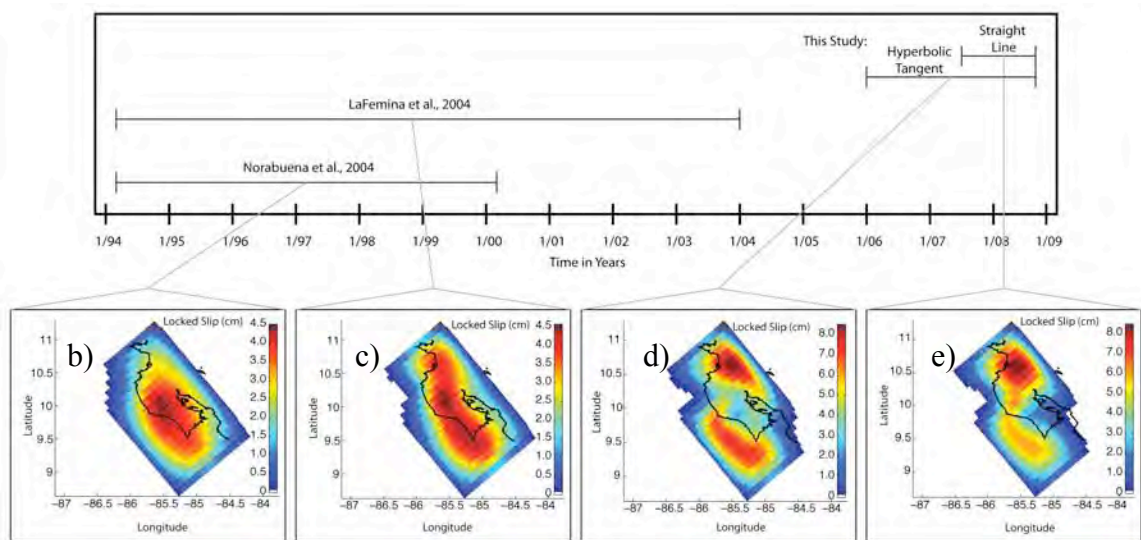


Figure 4.8. Comparison of the model consistent inversions from (b) Norabuena et al. [2004] (c) LaFemina et al. [2009] model 3 (d) this study MANA baseline hyperbolic tangent fit inversion results (e) this study IGSb-00 straight line fit inversion results. This comparison indicates the pattern of migrating area of maximum slip through time.

There are two disparate factors, which must be explored in order to substantiate that the strain accumulation patterns and magnitudes are indeed variable in time. The first of these factors is the difference in the number and distribution of GPS stations used in each of the three studies being compared. In order to test whether the strain accumulation pattern results of the LaFemina et al. [2009] study and the Norabuena et al. [2004] were biased by the increased number of stations relative to this study, I down sampled both the LaFemina et al. [2009] and Norabuena et al. [2004] data sets to match

the GPS network used in this study both in the locations and number of stations. These sensitivity tests were run using the same smoothing parameters and inversion characteristics as the best fitting model shown in Figure 4.8. The results of the test show that the strain accumulation patterns derived from a down sampled data set are the same as those from the original study both in magnitude and pattern of strain accumulation (Appendix B).

The second factor to be explored is that both the *LaFemina et al.* [2009] and *Norabuena et al.* [2004] studies use data which may be effected by slow slip events. It was suggested in section 3.6.4 that the magnitude of locking found in the *LaFemina et al.* [2009] and *Norabuena et al.* [2004] studies is underestimated due to the fact that they use data sets which do not account for the occurrence of slow slip events. This is further supported by the result from this study that there are areas beneath the Nicoya Peninsula that are fully locked. To test this supposition, I inflated the magnitude of the velocities in the *LaFemina et al.* [2009] and *Norabuena et al.* [2004] velocity fields by 33%, following the findings in section 3.6.4. The sensitivity tests were all run using the same smoothing parameters and inversion characteristics as the best fitting model shown in Figure 4.8. I also deflated the velocities used in this study for the ITRF based straight-line fit velocity field to test if 50% locking was achieved (in line with the ~50% locking results of but the LaFemina and Norabuena studies). The results of these sensitivity tests (Appendix B) show that the inflated velocities from both the Norabuena and Lafemina studies yield the same pattern of locking as the original velocity fields, re-inverted here (Figure 4.8), but with a maximum of ~70% locking. The results from deflating the ITRF based straight-line fit velocity field, reveal the same pattern of strain accumulation as the

higher velocity field, but with ~70% locking (Appendix B). These results imply that either, greater than a 33% deficit exists between the velocity fields in this study, and those that do not account for slow slip events (either because more slow slip events have occurred than have been estimated, or because there is more effect on the velocity fields per slow slip event than estimated) or, that there are indeed times where the fault plane is fully locked and times when that same area of the fault plane is partially locked. These results and sensitivity tests seem to support the idea that both the pattern and magnitude of strain accumulation on the fault plane beneath the Nicoya Peninsula is variable in time.

4.6.2 Comparison to Recent Earthquakes

The pattern of strain accumulation found in this study is also distinctly different from the pattern of recent (last 50 years) earthquake ruptures. There have been three $M_w \geq 7$ earthquakes in the vicinity of the Nicoya Peninsula in the last 50 years [Protti *et al.*, 1995b]. The magnitude and therefore rupture area of the 1950 event ($M_w = 7.7$) was significantly larger than that of the 1978 ($M_w = 6.9$) and 1990 earthquakes ($M_w = 7.0$). The recurrence interval for a large 1950 type events is believed to be about 50 years based on the previous two large events occurring in 1852 and 1900 [Protti *et al.*, 1995b] and assuming a periodic earthquake model. Norabuena *et al.* [2004] speculated that a future 1950 type Nicoya earthquake might be smaller than its 3 predecessors due to the occurrence of the 1978 event, the presence of abundant microseismicity and the apparent lack of locking in much of the 1950 rupture area. However, Protti *et al.* [2001] show that the 1978 earthquake only released 15% of the potential slip accumulated prior to the event and therefore its potential contribution to the reduction of the size of the next

Nicoya, 1950-style event is small. A comparison of the geometry of the rupture patterns of the most recent earthquakes as well as the locking pattern in this study (Figure 4.9) seems to suggest that, while the areas currently accumulating strain do intersect recent earthquake ruptures, the locus of maximum strain accumulation is offset considerably from these ruptures. Longer-term observations will help draw conclusions about the persistence of the strain accumulation patterns in relationship to the ultimate rupture pattern of the next earthquake.

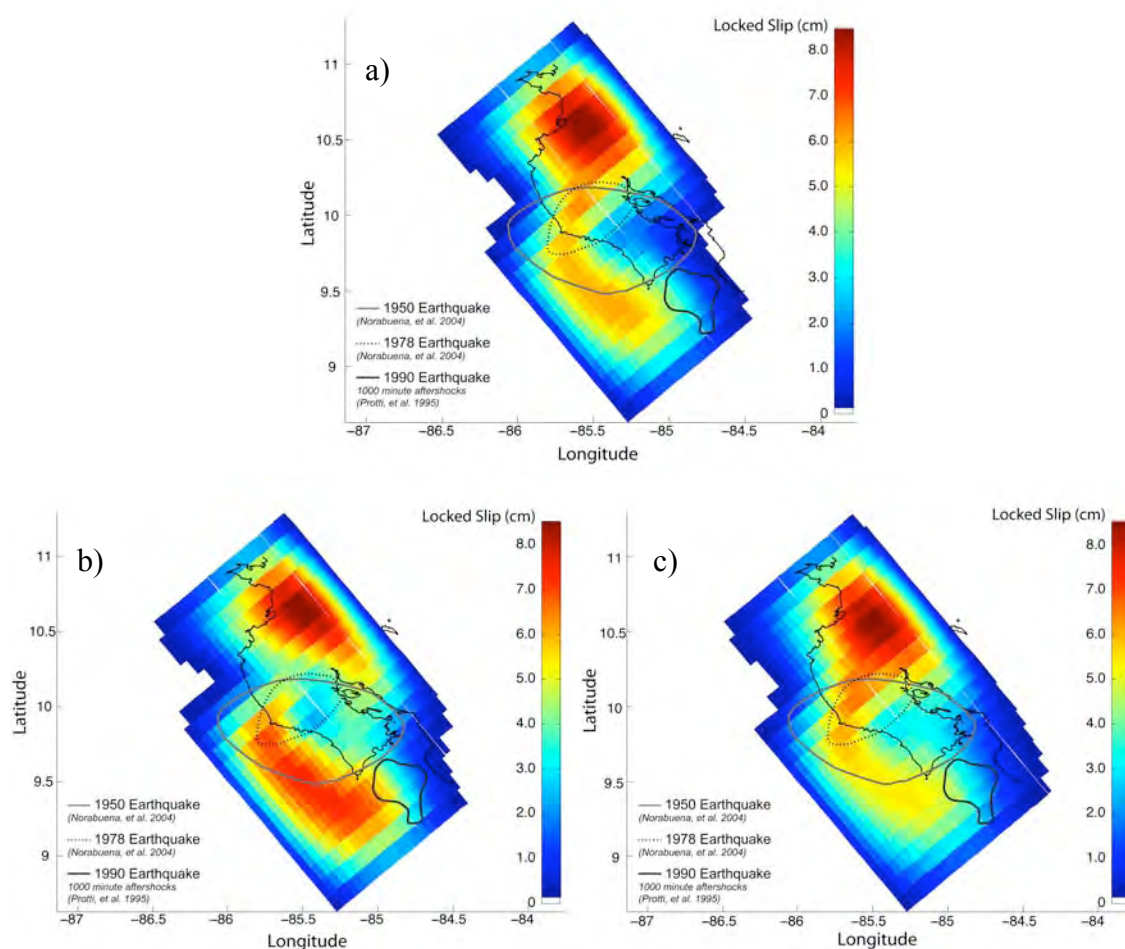


Figure 4.9. Best fitting inversion results overlain by earthquakes occurring in the Nicoya region since 1950. a) Best fitting inversion results for the ITRF based straight line fit velocity field ($w_{rms} = 5.89$ mm). b) Best fitting inversion results for the baseline based hyperbolic tangent fit velocity field ($w_{rms} = 2.58$ mm). c) Best fitting inversion results for the baseline based straight line fit velocity field ($w_{rms} = 4.94$ mm).

4.6.3 Comparison to Slow Slip Distribution

We can also compare the pattern of interseismic locking to the distribution of slip found during the 2007 slow slip event (chapter 3), as shown in Figure 4.10.

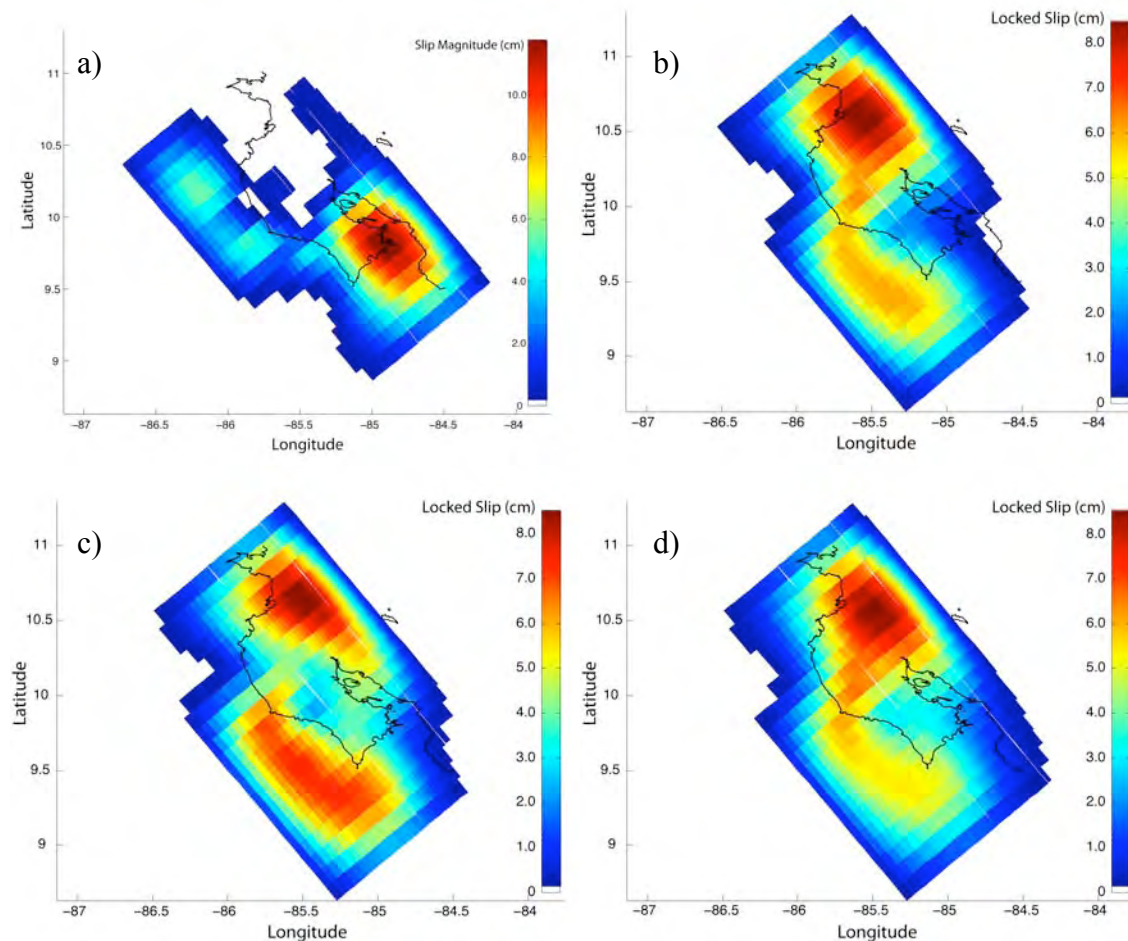


Figure 4.10. Comparison of slow slip distribution of Outerbridge et al. [2010] and chapter 3 to the interseismic locking distribution found in this study. a) Slow slip distribution from Outerbridge et al., [2010] and chapter 3. b) Interseismic locking distribution from the velocity field determined by a straight line fit to ITRF time series. c) Interseismic locking distribution from the velocity field determined by a hyperbolic tangent fit to baseline time series. d) Interseismic locking distribution from the velocity field determined by a straight line fit to baseline time series.

The most notable aspect of this comparison is that the patterns are anti-correlated: areas found to be locked in the interseismic period show little to no slip during the slow slip event, while areas found to have the largest slip during the slow slip event show

lower strain accumulation during the interseismic period. While the significance of this is not yet certain, the patterns of slip and locking found by this study may suggest that there is after slip from the 2007 slow slip event or some spatially variable physical constraint, that prevents the down-dip SE and up-dip NW portions of the fault plane from accumulating a large portion of strain during the interseismic period.

4.7 Conclusions

Here I have presented several versions of a revised velocity field for the Nicoya Peninsula, Costa Rica, which accounts for the occurrence of a slow slip event that occurred in 2007 as well as the associated best fitting inversion results. I have also presented the first comparison study, which suggests that locking patterns and magnitudes beneath the Nicoya Peninsula may be variable both spatially and temporally. I have found:

1. All three versions of velocity fields estimated here (ITRF based straight line fit, baseline based hyperbolic tangent fit, and baseline based straight line fit) produce a best fitting model where the maximum locking reaches 100% (~8.5 cm/yr) and is located on the northeast end of the modeled fault plane at a depth of 25-30km.
2. Each of the inversion results from this study show an up-dip patch of locking located on the southwest end of the modeled fault plane. The magnitude of locking on this patch ranges from ~68-82%. This range may reflect the different time frames captured by the velocity fields.

3. In contrast to the *LaFemina et al.* [2009] study, the deeper, maximum locked patch found in this study is deeper, further north and consistently found to be 100% locked. As shown by *Outerbridge et al.* [accepted] and described in section 3.6.4 (Figure 3.15), Nicoya interseismic velocity fields that do not account for slow slip events can underestimate the true velocities by up to $\sim 1/3$. This could account for the lower percent of locking reported by both *LaFemina et al.* [2009] and *Norabuena et al.* [2004].
4. The up-dip locked patch in this study, found to be 65-82% locked, is in approximately the same location as the shallow patch found by *Norabuena et al.* [2004] to be 65% locked. While the up-dip patch in this study finds locking in the same range as the *Norabuena et al.* [2004] study, it does not find that this is the area of maximum locking. This contrast between maximum locking of 65% in the *Norabuena et al.* [2004] study and 100% maximum locking in this study, and the location of maximum locking being on the shallow portion of the fault plane in the *Norabuena et al.* [2004] study and the deeper portion of the fault plane in this study, could reflect better data quality and temporal resolution in this study, or could be evidence of changing strain conditions.
5. The locus of strain accumulation appears to migrate from up-dip and to the South to down-dip and to the North over time, as does the area of maximum locking. This suggests that strain accumulation patterns in this

region are not consistent throughout a seismic cycle and can change on the decadal time scale.

6. While the areas currently accumulating strain do intersect recent earthquake ruptures, the locus of maximum strain accumulation is offset considerably from these ruptures. Longer-term observations will help draw conclusions about the persistence of the strain accumulation patterns in relationship to the ultimate rupture pattern of the next earthquake.
7. The patterns of slip and locking found by this study may suggest that there is after slip from the 2007 slow slip event that prevents the down-dip SE and up-dip NW portions of the fault plane from accumulating a large portion of strain during the interseismic period.




These results imply that either a slip deficit exists between the velocity fields in this study, and those that do not account for slow slip events (either because more slow slip events have occurred than have been estimated, or because there is more effect on the velocity fields per slow slip event than estimated) or, that there are indeed times where the fault plane is fully locked and times when that same area of the fault plane is partially locked. These results and sensitivity tests seem to support the idea that both the pattern and magnitude of strain accumulation on the fault plane beneath the Nicoya Peninsula is variable in time.




Appendix A

This appendix will present additional information and explanation pertaining to Chapter 3.

A.1 CGPS Network

The CGPS network on the Nicoya Peninsula was installed in phases beginning in 2002 and continuing in 2005, 2006, 2007, 2008 and 2009. As mentioned briefly in section 3.3 there is some variation in the monumentation between sites. The biggest changes were instituted in 2006 when the installation protocols were changed to be congruent with Plate Boundary Observatory (PBO) standards. Below are pictures of each CGPS station along with a detailed description in the order in which they were installed.

		
<p><i>Figure A.1 INDI is a concrete pillar monument, with a 30 cm diameter extending to a depth of 5 meters. The antenna sits on a spike mount above a stainless steel pin. INDI is equipped with a Trimble 5700 receiver and a Zephyr Geodetic^(TM) antenna with ground plane.</i></p>	<p><i>Figure A.2 HUA2 has a 4 m deep, rebar-cored cement pillar, with side braces located in weathered ophiolite. The antenna is attached to the pillar by a threaded bolt that is embedded in the cement pillar. HUA2 is equipped with a Trimble 5700 receiver and a Zephyr Geodetic^(TM) antenna with ground plane.</i></p>	<p><i>Figure A.3a PUJE has a stainless steel pin set in bedrock. Above the pin is a spike mount with a long center pole on which the antenna sits. PUJE is equipped with a Trimble 5700 receiver and a Zephyr Geodetic^(TM) antenna with ground plane.</i></p>

		
<p><i>Figure A.3b PUJE was updated in July 2009 to PBO specifications. The center pole was drilled into the original stainless steel pin. PUJE is now equipped with a Trimble NetRS receiver and a Choke Ring antenna with ray dome.</i></p>	<p><i>Figure A.4 BON2 has a rebar-cored cement pillar where the antenna is attached to the pillar by a threaded bolt that is embedded in the cement pillar. BON2 is equipped with a Trimble 5700 receiver and a Zephyr Geodetic^(TM) antenna with ground plane.</i></p>	<p><i>Figure A.5a PNEG has a rebar-cored cement pillar where the antenna is attached to the pillar by a threaded bolt that is embedded in the cement pillar. PNEG is equipped with a Trimble 5700 receiver and a Zephyr Geodetic^(TM) antenna with ground plane.</i></p>




		
<p><i>Figure A.5b PNEG had to be relocated in August 2009 and is now built to PBO specifications. PNEG is now equipped with a Trimble Choke Ring antenna with ray dome and a Trimble NetRS receiver. A tie was performed for station continuity.</i></p>	<p><i>Figure A.6 LEPA is built to the specifications of PBO. It is a deep-drilled monument where each bracing leg reaches depths of 10-12 m to maximize coupling. LEPA is equipped with a Trimble Choke Ring antenna with ray dome and a Trimble NetRS receiver.</i></p>	<p><i>Figure A.7 QSEC is built to the specifications of PBO. It is a deep-drilled monument where each bracing leg reaches depths of 10-12 m to maximize coupling. QSEC is equipped with a Trimble Choke Ring antenna with ray dome and a Trimble NetRS receiver.</i></p>









Figure A.8 GRZA is built to the specifications of PBO. It is a short-drilled monument where each bracing leg reaches depths of ~1.5 m to maximize coupling. GRZA is equipped with a Trimble Choke Ring antenna with ray dome and a Trimble NetRS receiver.






Figure A.9 HATI is built to the specifications of PBO. It is a short-drilled monument where each bracing leg reaches depths of ~1.5 m to maximize coupling. GRZA is equipped with a Trimble Choke Ring antenna with ray dome and a Trimble NetRS receiver.



Figure A.10 PUMO is built to the specifications of PBO. It is a short-drilled monument where each bracing leg reaches depths of ~1.5 m to maximize coupling. PUMO is equipped with a Trimble Choke Ring antenna with ray dome and a Trimble NetRS receiver.

		
<p><i>Figure A.11 LMNL is built to the specifications of PBO. It is a short-drilled monument where each bracing leg reaches depths of ~1.5 m to maximize coupling. LMNL is equipped with a Trimble Choke Ring antenna with ray dome and a Trimble NetRS receiver.</i></p>	<p><i>Figure A.12 ELVI is built to the specifications of PBO. It is a short-drilled monument where each bracing leg reaches depths of ~1.5 m into weathered ophiolite. ELVI is equipped with a Trimble Choke Ring antenna with ray dome and a Trimble NetRS receiver.</i></p>	<p><i>Figure A.13 SAJU is built to the specifications of PBO. It is a short-drilled monument where each bracing leg reaches depths of ~1.5 m to maximize coupling. SAJU is equipped with a Trimble Choke Ring antenna with ray dome and a Trimble NetRS receiver.</i></p>
		
<p><i>Figure A.14 VERA is built to PBO specifications. It's a short-drilled monument where each bracing leg reaches depths of ~1.5m to maximize coupling. VERA is equipped with a Trimble Choke Ring antenna with ray dome and a Trimble NetRS receiver. Also shown is the equipment enclosure, which houses the receiver, batteries, solar panels and communications.</i></p>	<p><i>Figure A.15 CABA is built to PBO specifications. It's a short-drilled monument where each bracing leg reaches depths of ~1.5m to maximize coupling. CABA is equipped with a Trimble Choke Ring antenna with ray dome and a Trimble NetRS receiver. Also shown is the equipment enclosure, which houses the receiver, batteries, solar panels and communications.</i></p>	<p><i>Figure A.16 EPZA is built to PBO specifications. It's a short-drilled monument where each bracing leg reaches depths of ~1.5m to maximize coupling. EPZA is equipped with a Trimble Choke Ring antenna with ray dome and a Trimble NetRS receiver. Also shown is the equipment enclosure, which houses the receiver, batteries, solar panels and communications.</i></p>

		
<p><i>Figure A.17 LAFE is built to the specifications of PBO. It is a short-drilled monument where each bracing leg reaches depths of ~1.5 m to maximize coupling. CABA is equipped with a Trimble Choke Ring antenna with ray dome and a Trimble NetRS receiver. Also shown is the equipment enclosure, which houses the receiver, batteries, solar panels and communications.</i></p>	<p><i>Figure A.18 BIJA is built to the specifications of PBO. It is a short-drilled monument where each bracing leg reaches depths of ~1.5 m to maximize coupling. CABA is equipped with a Trimble Choke Ring antenna with ray dome and a Trimble NetRS receiver. Also shown is the equipment enclosure, which houses the receiver, batteries, solar panels and communications.</i></p>	<p><i>Figure A.19 Representative picture of the interior of the communications box at all GPS stations. Box contains GPS receiver, 2 batteries, power board, solar panels attached to the exterior and communications equipment.</i></p>

A.2 Station Optimization vs. Network Optimization

A.2.1 Displacement Fields

As described in Chapter 3, two approaches were employed to determine the displacement field during the May 2007 slow slip event. In the first approach, best fit estimates for all parameters are obtained, requiring only the timing parameters (T and τ) are the same for both (N, E) horizontal components at each station. This allows timing parameters to vary between stations, e.g. to investigate possible migration of slip. The combined chi squared misfits of the north and east components were minimized to

identify the best fitting parameters. These will be referred to as station-optimized fits (Figure A.20a). In the second approach, I fixed the timing parameters, T and τ , to average values based on 7 stations where the event is well defined and the signal to noise ratio is high (2007 day of year 160 and 20 days respectively). These fits will be referred to as network-optimized fits (Figure A.20b). Displacement estimates from the two approaches are very similar. A comparison reveals that the biggest differences in the displacement values found by the two fits are in the more inland stations. This makes sense since these are the stations with the least resolution of the fault plane (greatest distance to the fault plane) and the highest uncertainty. This should not affect the inversion results since the inversions are weighted.

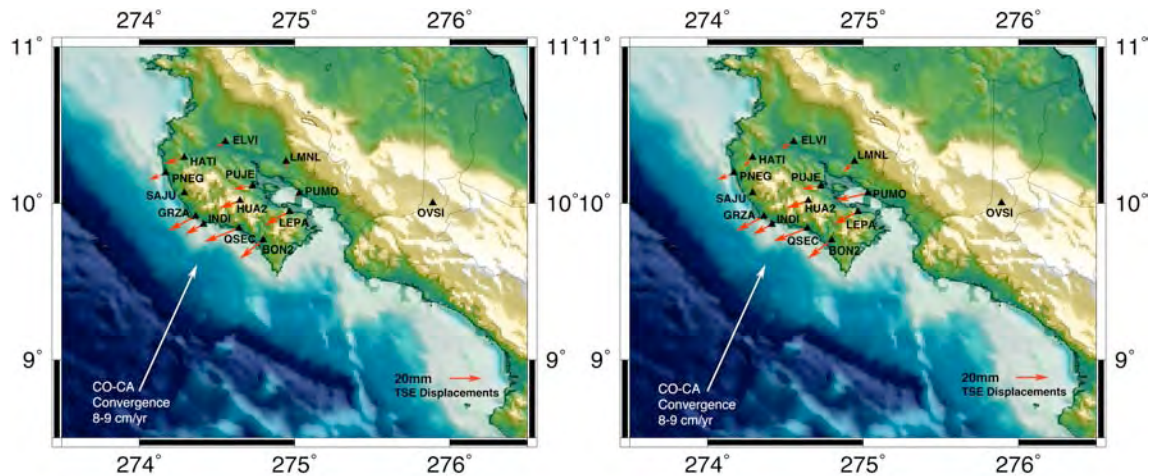


Figure A.20 A comparison between the displacement fields found by a) the station-optimized and b) network-optimized methods. As you can see there is very little difference between the two.

A.2.2 Inversions

As described in chapter 3, many inversions were performed, varying different parameters to ensure that my model results were not sensitive to simplifying assumptions.

A summary of all models run is presented in Table A.1.

Table A.1. A summary of all models, run to ensure that my models were not sensitive to simplifying assumptions.

Model Fit	Data Weight	Smoothing	Rake	Misfit (mm)	Max Slip (cm)	M_0 (Nm)	M_w^*	Inversion Figure
Station	Unweighted	2100	220°	3.00	9.16	3.26E+19	7.0	A.21a
Station	Unweighted	13400	220°	6.00	2.10	1.25E+19	6.7	A.21b
Network	Unweighted	2250	220°	3.00	13.71	3.94E+19	7.0	A.21c
Network	Unweighted	10000	220°	6.00	3.05	1.73E+19	6.8	A.21d
Station	Unweighted	1900	238°	2.52	6.66	2.69E+19	6.9	A.22a
Station	Unweighted	13400	238°	4.84	2.29	1.37E+19	6.7	A.22b
Network	Unweighted	1700	244°	2.71	10.16	4.61E+19	7.1	A.22c
Network	Unweighted	10000	244°	4.39	3.28	1.93E+19	6.8	A.22d
Station	Weighted	1600000	220°	4.51	11.78	3.49E+19	7.0	A.23a
Station	Weighted	1.0×10^8	220°	8.18	2.21	1.25E+19	6.7	A.23b
Network	Weighted	1600000	220°	4.21	12.43	3.69E+19	7.0	A.23c
Network	Weighted	1.0×10^8	220°	9.48	2.20	1.28E+19	6.7	A.23d
Station	Weighted	1200000	238°	3.81	7.45	3.48E+19	7.0	A.24a
Station	Weighted	1.0×10^8	238°	6.79	2.68	1.61E+19	6.7	A.24b
Network	Weighted	750000	244°	3.71	11.41	3.98E+19	7.0	A.24c
Network	Weighted	1.0×10^8	244°	6.14	2.83	1.71E+19	6.8	A.24d
*Equivalent Magnitude								

Inversions were completed for both the station-optimized and network-optimized displacement fields. A direct comparison between analogous station-optimized (Figures A.21a and b, Figures A.22a and b, Figures A.23a and b, Figures A.24a and b) and network-optimized (Figures A.21c and d, Figures A.22c and d, Figures A.23c and d, Figures A.24c and d) models shows that the pattern of slip remains the same and the biggest differences are in the magnitudes of slip.

I compare the results from both weighted and unweighted data to ensure that the results were not biased by error estimates, since a rigorous analysis of the offset uncertainties has not been done. Results of the weighted and unweighted inversions are remarkably similar. I inverted the weighted offsets presented in Table 3.2a (Figures A.23a and b, A.24a and b) and Table 3.2b (Figures A.23c and d, A.24c and d).

Unweighted offsets are those presented in Tables 3.2a and 3.2b, without utilizing the

uncertainties (Figures A.21 and A.22). A comparison of corresponding weighted to unweighted inversion results are virtually identical, showing that results were not biased by error estimates.

I constrained slip direction in the model, testing several values. I first constrained the slip direction to be 10° counter-clockwise of trench normal (220°), similar to convergence direction (Figure A.21). This constraint is supported by the a priori knowledge of the convergence direction [DeMets, 2001] and by the general knowledge that strain release events are generally anti-parallel to convergence direction. I also tested values of 238° and 244° , representing the average azimuth of the station-optimized fits and network-optimized fits respectively (Figure A.22). Results of all three were very similar. The most significant difference is the location and magnitude of the updip slip patch, in the two-patch model. In the azimuth based rake models, the location of the updip patch is shifted southeast and has more slip attributed to it. This shift is reproduced in models run with weighted data as well, looking at a rake fixed based on convergence direction (Figure A.23) and average azimuth of slip (Figure A.24).

The preferred rake orientation was chosen consistent with convergence direction. The higher uncertainty levels of the timing parameters may bias the displacement estimates. In addition, despite the fact that the slip direction of thrust earthquakes has been shown to be $\sim 10^\circ$ clockwise of the convergence direction [DeMets, 2001], these are complimented by right lateral strike slip earthquakes. Together, the strike slip and thrust motions account for release of strain from the oblique subduction of the Cocos Plate beneath the Caribbean Plate. Thus far, no complimentary strike slip directed slow slip

events have been recorded. Therefore, all oblique motion strain release may be accounted for by an oblique thrusting slow slip event.

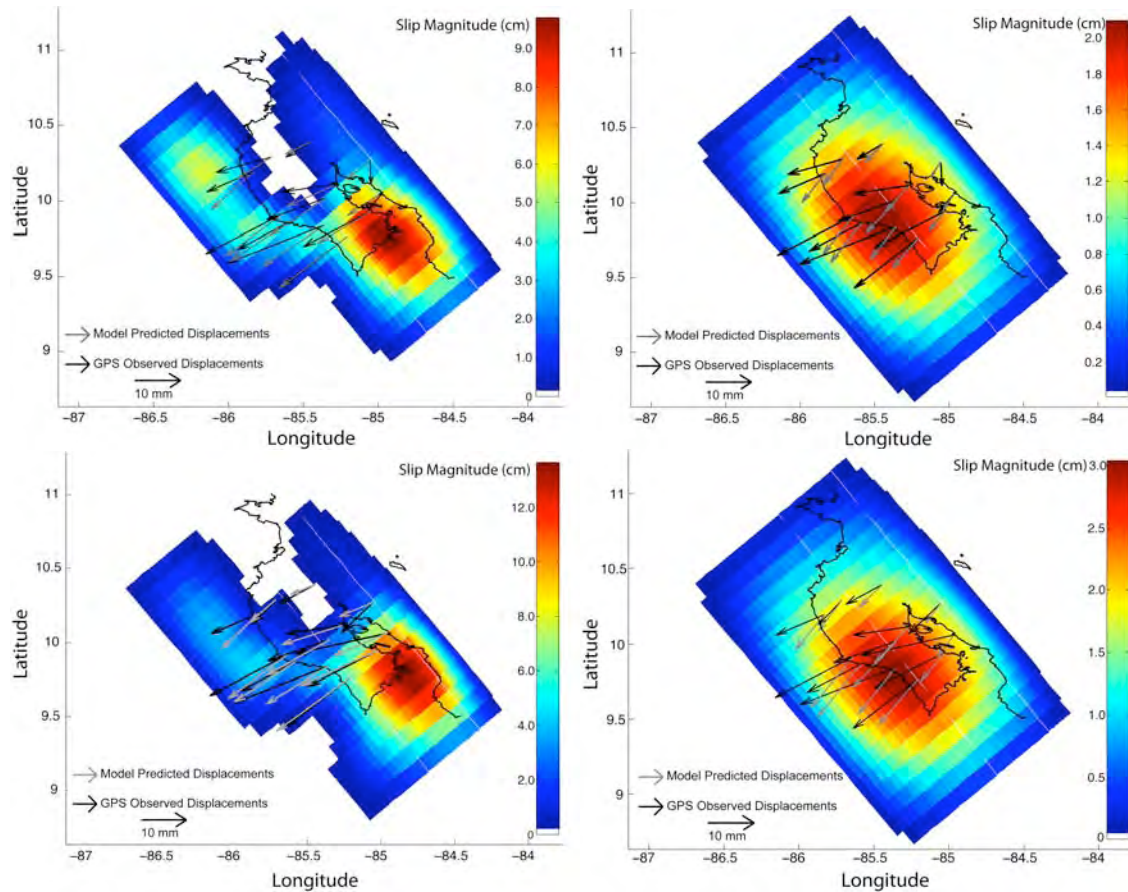


Figure A.21. Predicted vs. observed offsets for unweighted data with the rake fixed at 220. a) Station optimized timing parameters, $rms=3$. b) Station optimized timing parameters, $rms=6$ c) Network optimized timing parameters, $rms=3$. d) Network optimized timing parameters, $rms=6$.

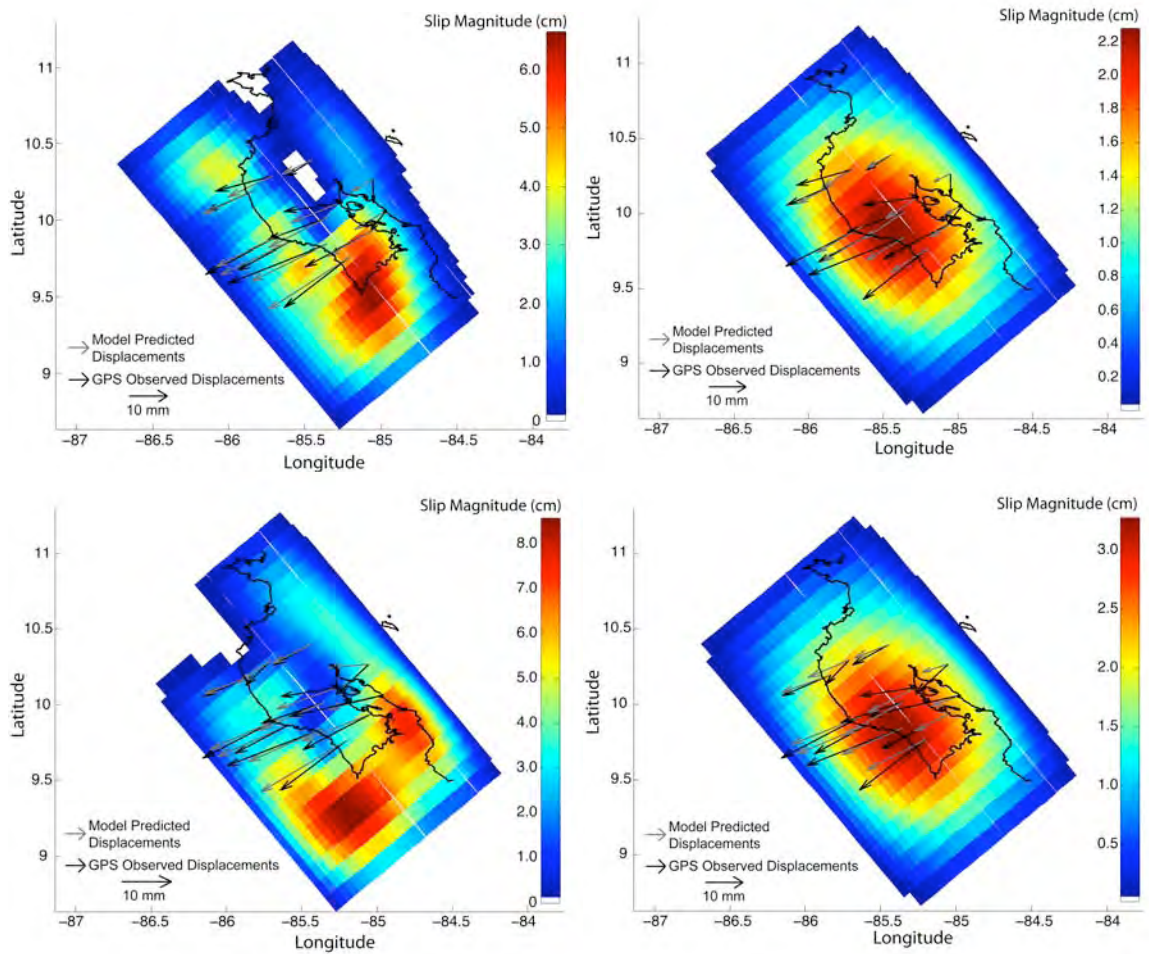


Figure A.22. Predicted vs. observed offsets for unweighted data varying the rake based on the average azimuth of event slip. a) Station optimized timing parameters, rms=2.5. b) Station optimized timing parameters, rms=4.8 c) Network optimized timing parameters, rms=2.7. d) Network optimized timing parameters, rms=4.4.

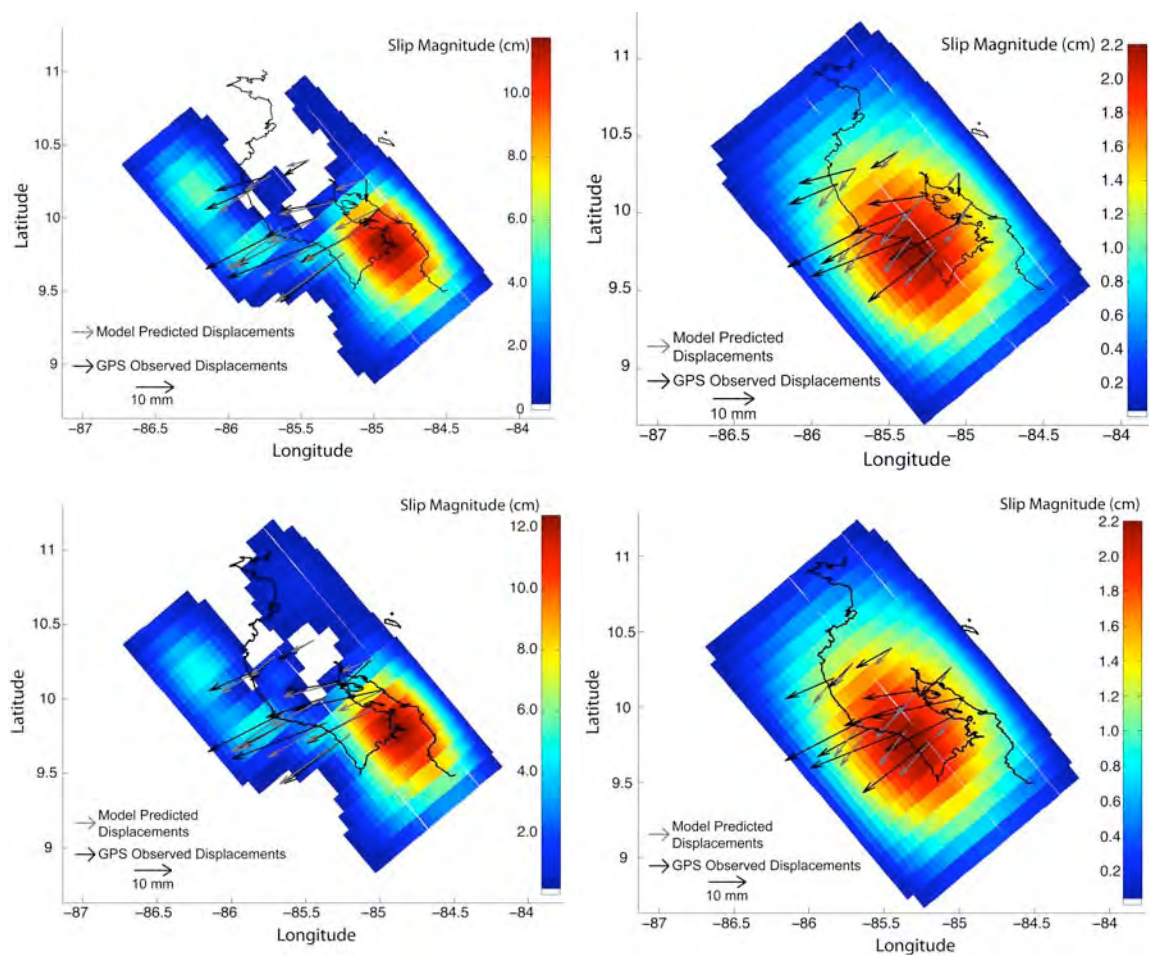


Figure A.23. Predicted vs. observed offsets for weighted data with a fixed rake of 220° , consistent with the convergence direction [DeMets, 2001]. a) Station optimized timing parameters, $wrms=4.5$ mm. b) Station optimized timing parameters, $wrms=8.2$ mm. c) Network optimized timing parameters, $wrms=4.2$ mm. d) Network optimized timing parameters, $wrms=9.5$ mm.

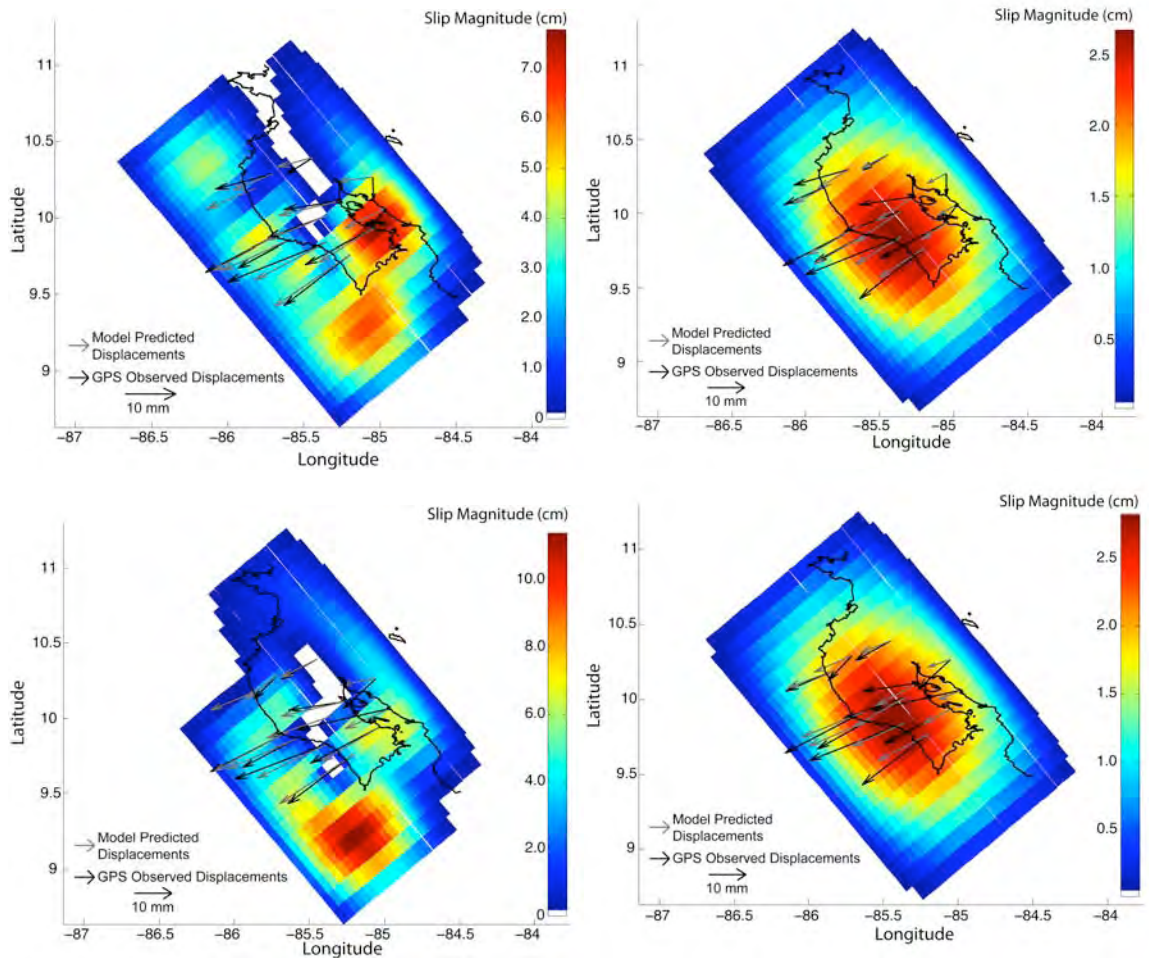


Figure A.24. Predicted vs. observed offsets for weighted data with rake based on the average azimuth of slip. a) Station optimized timing parameters, $wrms=3.2$ mm. b) Station optimized timing parameters, $wrms=6.8$ mm. c) Network optimized timing parameters, $wrms=3.7$ mm. d) Network optimized timing parameters, $wrms=6.1$ mm.

A.3 Sensitivity Tests

In addition to using variations in model parameters to test assumptions, I also performed sensitivity tests to determine if the model output was more sensitive to any one station. This was done using the parameters from the preferred weighted inversion model and inverting the dataset iteratively, removing one GPS data point at a time (Table A.2). This test shows that the inversion results are not sensitive to the surface displacement estimate at any one station. Additionally, the inland stations, which have the largest

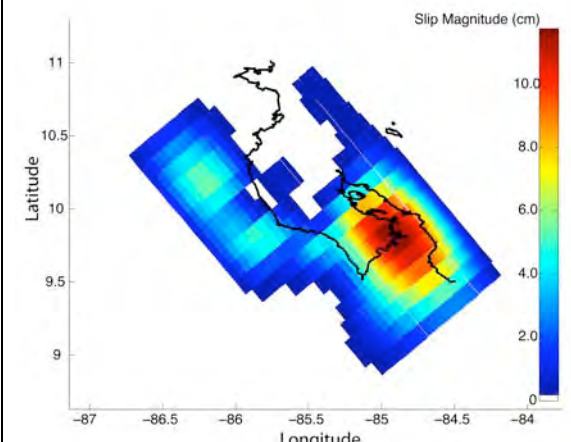
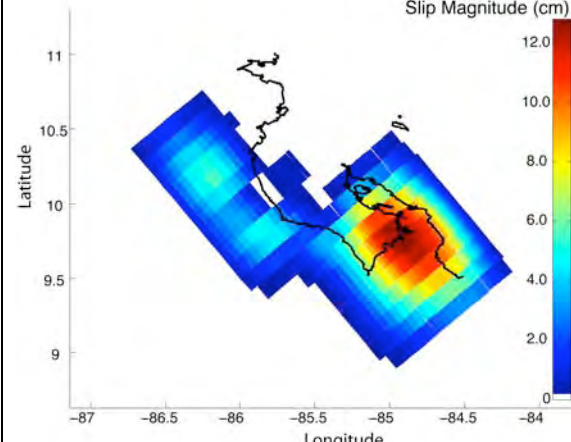
uncertainties, were both eliminated from the data set and set to zero in the inversion. Neither the zero motion of, nor the removal of, the inland stations, changes the slip distribution significantly. The biggest difference in model results when the motion from these stations is removed is the magnitude of maximum slip. This intuitively makes sense since weighted inversions were performed for the preferred model and the relatively high level of uncertainty for the inland stations was accounted for by the inversion code.

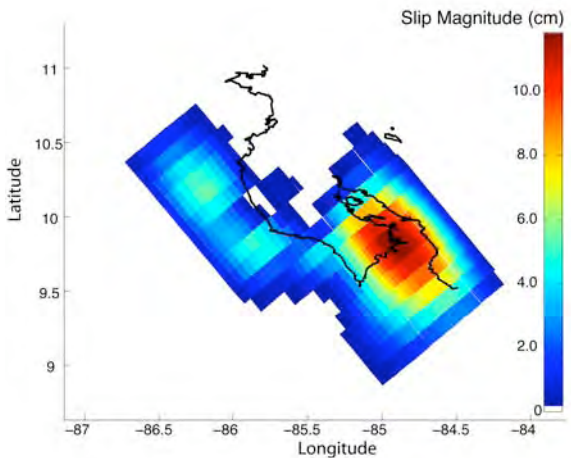
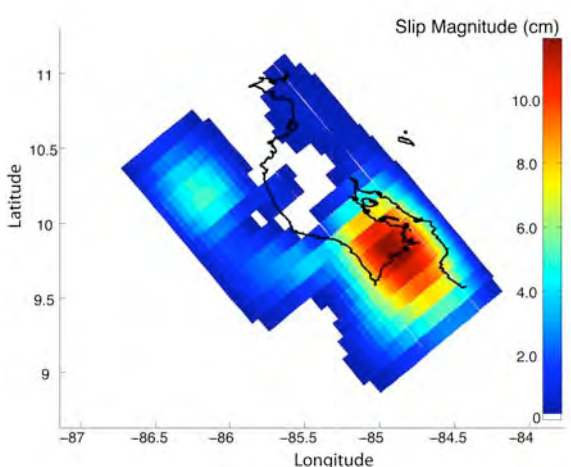
This result is also consistent with the sensitivity test that I performed, removing one station at a time and rerunning the inversion using the preferred model parameters. The pattern of the slip distribution did not change measurably when any one station was removed. The result of this investigation seem to indicate that the event slip distribution is not sensitive to one station in particular, nor to the stations with the smallest surface displacements and largest uncertainty (the three inland stations).

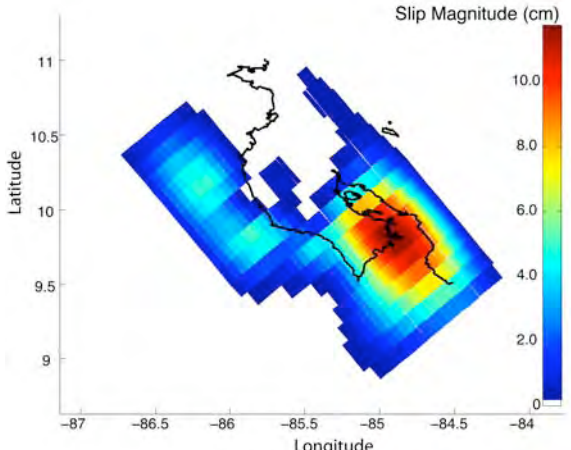
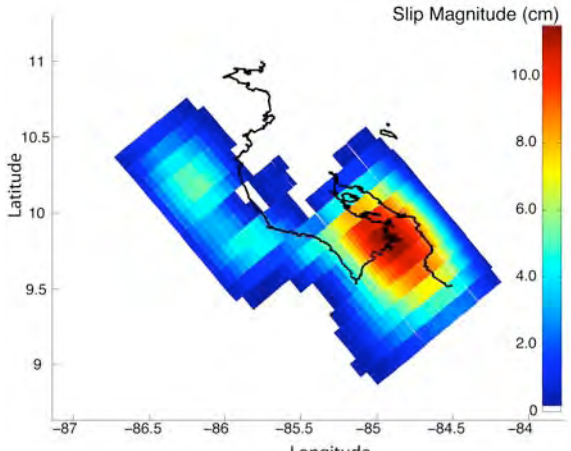
In all models, the slip distribution extends to the limits of the modeled fault plane. To test if the slip distribution changes when considering a larger modeled area all parameters from the preferred model were preserved except the length of the fault, this includes meshing size. Therefore, along strike mesh is 36 pixels, 12.5 km long, to maintain the 12.5 km along strike pixel size of the preferred model. In addition, the modeling program used, *slipinv* [Funning, 2005], defines the fault geometry from a central point extending outward, therefore, the model was extend 100 km further in both directions making it a total of 450 km long. As shown in Table A.2, increasing the fault geometry smears the slip distribution of the deeper patch, along strike. However, the reason this geometry was not employed for the preferred model geometry is because we have no CGPS data in this region to provide testable constraint on any motion that may

be found here. Evidence for this is illustrated by the along strike resolution reaching 130 km and the down dip resolution reaches 120 km at the far edges of the larger modeled fault plane. In other words, at the far edges of the fault plane only features 130 km x 120 km in size are discernable. Therefore there is no way to determine if the pattern of slip observed towards the edges of the extended fault plane is real.

Table A.2 Table of sensitivity tests done on weighted, station optimized data set using preferred model parameters (smoothing 1600000, rake 220°)

Sensitivity Test	WRMS (mm)	M_0 (Nm)	Equivalent M_w	Maximum Slip (cm)	Inversion Slip Distribution
Preferred Model	4.51 mm	3.49E+19	7.0	11.78 cm	 <p>The map shows the slip magnitude distribution for the preferred model. The x-axis is Longitude (ranging from -87 to -84) and the y-axis is Latitude (ranging from 9 to 11). A color scale on the right indicates slip magnitude in centimeters, ranging from 0 (blue) to 10.0 (red). The highest slip magnitudes (red/orange) are concentrated in the central-eastern part of the fault system, with values reaching up to 10.0 cm.</p>
Removing BON2	4.75 mm	3.66E+19	7.0	12.84 cm	 <p>The map shows the slip magnitude distribution for the 'Removing BON2' model. The axes and color scale are the same as in the preferred model map. However, the color scale on the right now ranges from 0 (blue) to 12.0 (red). The highest slip magnitudes (red) are concentrated in the same central-eastern region, with values reaching up to 12.0 cm, indicating a larger maximum slip compared to the preferred model.</p>

Removing ELVI	4.71 mm	3.46E+19	7.0	11.84 cm	
Removing GRZA	4.36 mm	3.50E+19	7.0	11.93 cm	

Removing HATI	4.25 mm	3.43E+19	7.0	11.75 cm	
Removing HUA2	4.65 mm	3.38E+19	7.0	11.52 cm	

Removing INDI	4.62 mm	3.56E+19	7.0	11.84 cm	
Removing LEPA	4.64 mm	3.21E+19	6.9	10.82 cm	

Removing LMNL	4.24 mm	3.43E+19	7.0	12.10 cm	
Removing PNEG	4.62 mm	3.31E+19	6.9	11.66 cm	

Removing PUJE	4.63 mm	3.56E+19	7.0	11.58 cm	
Removing PUMO	4.27 mm	3.56E+19	7.0	11.87 cm	

Removing QSEC	3.86 mm	3.86E+19	7.0	12.25 cm	
Removing Inland Stations	4.08 mm	3.46E+19	7.0	12.36 cm	

Setting Inland Stations to Zero	5.28 mm	3.28E+19	6.9	12.86 cm	
Elongated Fault	4.52 mm	6.00E+19	7.1	11.26 cm	

Appendix B

This appendix will present additional information and explanation pertaining to Chapter 4.

B.1 Results of Comparison Velocity Field Down Sampling

Two factors were explored to substantiate that the strain accumulation patterns and magnitudes are indeed variable in time. The first of these factors is the difference in the number and distribution of GPS stations used in each of the three studies being compared. In order to test whether the strain accumulation pattern results of the *LaFemina et al.* [2009] study and the *Norabuena et al.* [2004] were biased by the increased number of stations relative to this study, I down sampled both the *LaFemina et al.* [2009] and *Norabuena et al.* [2004] data sets to match the GPS network used in this study both in the locations and number of stations. These sensitivity tests were run using the same smoothing parameters and inversion characteristics as the best fitting models shown in Figure 4.8, including maintaining consistency of the comparison models to this study's best fitting models. The results of the test show that the strain accumulation patterns derived from a down sampled data set are very similar to those from the original data set both in magnitude and pattern of strain accumulation (Figures B.1 and B.2).

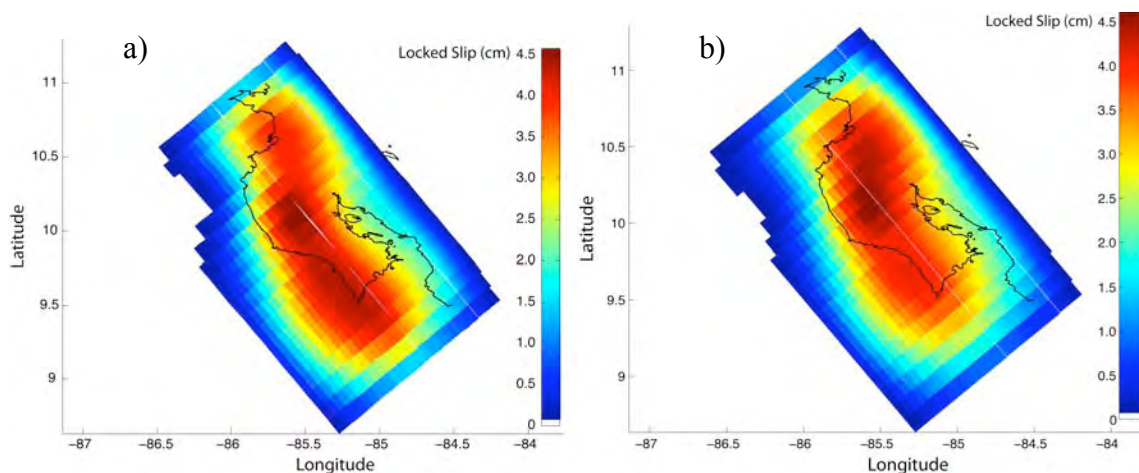


Figure B.1 (a) Strain accumulation pattern using the original data set from LaFemina et al. [2009] and according to the inversion scheme and boundary conditions to be consistent with this study. (b) Strain accumulation pattern using the down sampled data set from LaFemina et al. [2009] for consistency with the results from this study in boundary conditions, inversion scheme and sample density. These results show that there is no bias from the sampling density of LaFemina et al. [2009], indicating that the potential temporal variability may indeed be real.

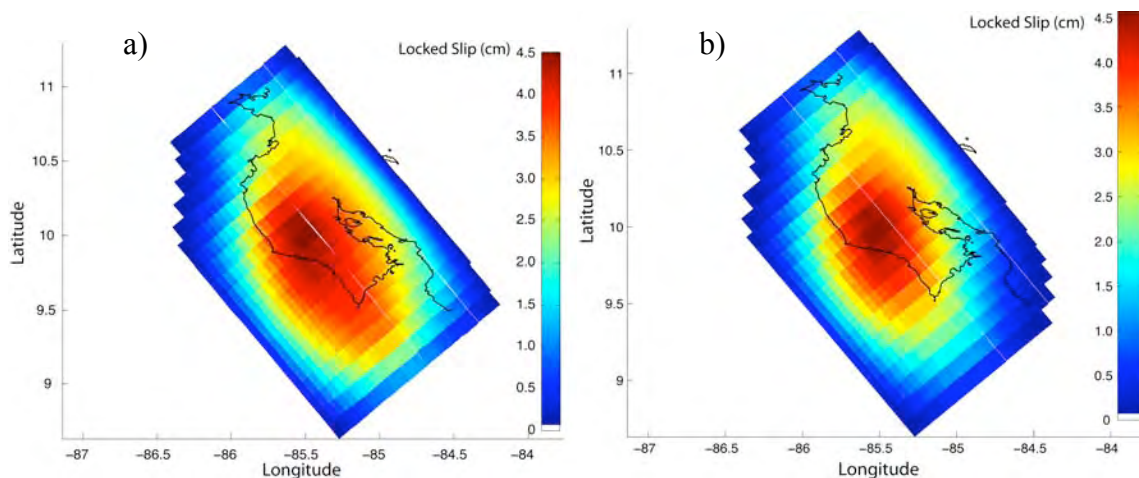


Figure B.2 (a) Strain accumulation pattern using the original data set from Norabuena et al. [2004] and according to the inversion scheme and boundary conditions to be consistent with this study. (b) Strain accumulation pattern using the down sampled data set from Norabuena et al. [2004] for consistency with the results from this study in boundary conditions, inversion scheme and sample density. These results show that there is very little bias from the sampling density of Norabuena et al. [2004], indicating that the potential temporal variability may indeed be real.

B.2 Results of Velocity Field Magnitude Adjustments

The second factor to be explored is that both the *LaFemina et al.* [2009] and *Norabuena et al.* [2004] studies use data which may be effected by slow slip events. It was suggested in section 3.6.4 that the magnitude of locking found in the *LaFemina et al.* [2009] and *Norabuena et al.* [2004] studies is underestimated due to the fact that they use data sets which do not account for the occurrence of slow slip events. This is further supported by the result from this study that there are areas beneath the Nicoya Peninsula that are fully locked. To test this supposition, I inflated the magnitude of the velocities in the *LaFemina et al.* [2009] and *Norabuena et al.* [2004] velocity fields by 33%, following the findings in section 3.6.4. The sensitivity tests were all run using the same smoothing parameters and inversion characteristics as the best fitting model shown in Figure 4.8. I also deflated the velocities used in this study for the ITRF based straight-line fit velocity field to test if 50% locking was achieved (in line with the ~50% locking results of but the LaFemina and Norabuena studies). The results of these sensitivity tests (Appendix B) show that the inflated velocities from both the Norabuena and Lafemina studies yield the same pattern of locking as the original velocity fields, re-inverted here (Figure 4.8), but with a maximum of ~70% locking. The results from deflating the ITRF based straight-line fit velocity field, reveal the same pattern of strain accumulation as the higher velocity field, but with ~70% locking (Figure B.5). These results imply that either, greater than a 33% deficit exists between the velocity fields in this study, and those that do not account for slow slip events (either because more slow slip events have occurred than have been estimated, or because there is more effect on the velocity fields per slow slip event than estimated) or, that there are indeed times where the fault plane is

fully locked and times when that same area of the fault plane is partially locked. These results and sensitivity tests seem to support the idea that both the pattern and magnitude of strain accumulation on the fault plane beneath the Nicoya Peninsula is variable in time.

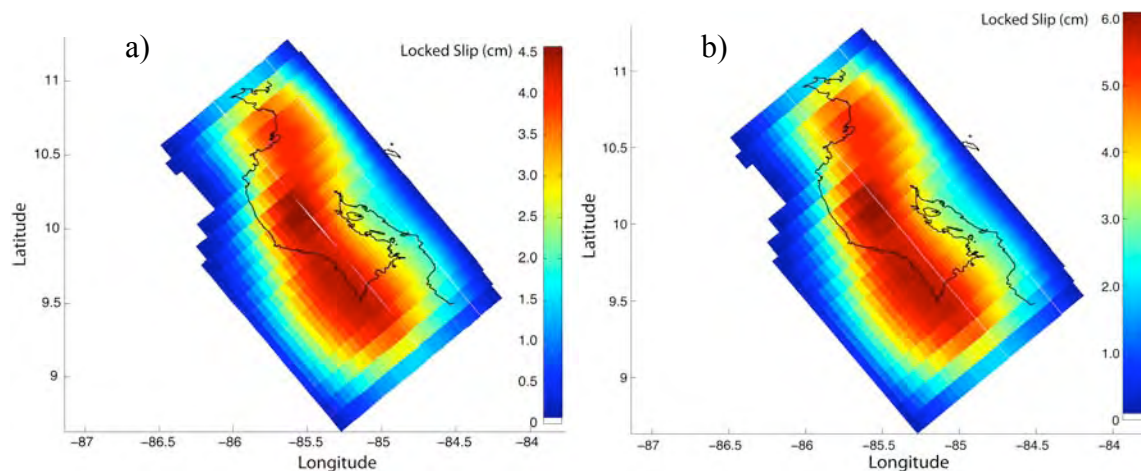


Figure B.3 (a) Strain accumulation pattern using the original velocity field from LaFemina et al. [2009] and according to the inversion scheme and boundary conditions to be consistent with this study. (b) Strain accumulation pattern using the velocity field from LaFemina et al. [2009] inflated by 33%. These results show that the magnitude of locking is affected by this change, but not the pattern, indicating that the potential temporal variability may indeed be real.

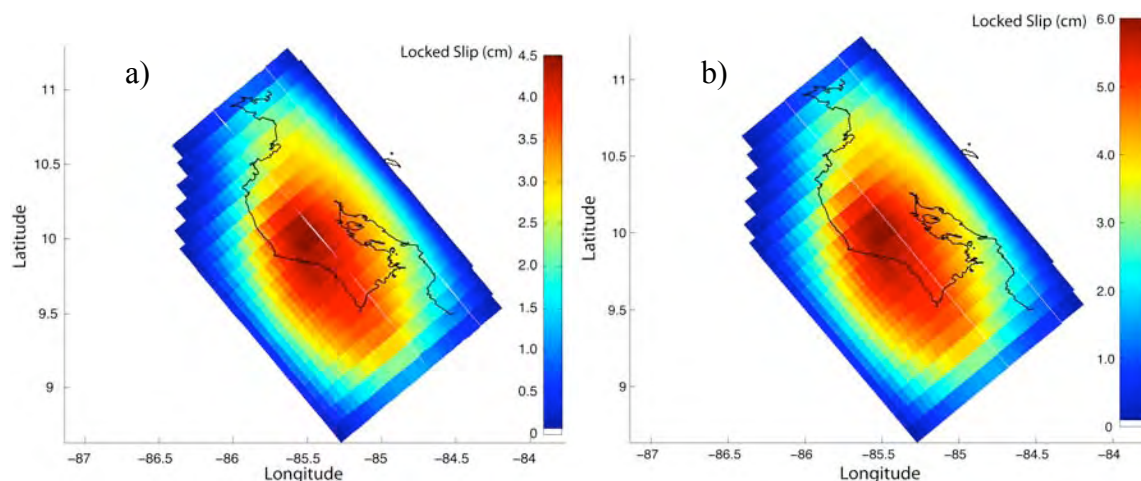


Figure B.4 (a) Strain accumulation pattern using the original velocity field from Norabuena et al. [2004] and according to the inversion scheme and boundary conditions to be consistent with this study. (b) Strain accumulation pattern using the velocity field from Norabuena et al. [2004] inflated by 33%. These results show that the magnitude of locking is affected by this change, but not the pattern, indicating that the potential temporal variability may indeed be real.

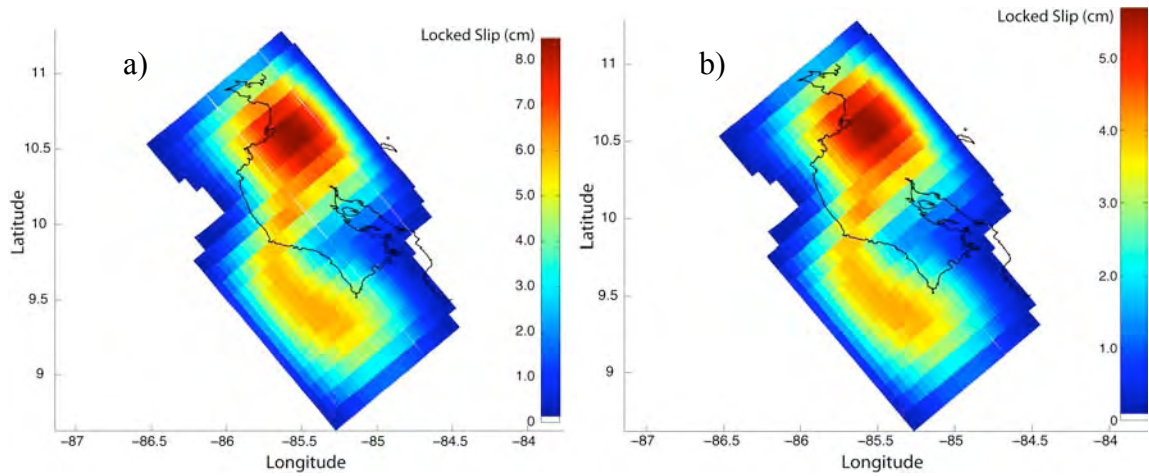


Figure B.5 (a) Strain accumulation pattern using the ITRF Straight Line fit velocity field. (b) Strain accumulation pattern using the ITRF Straight Line fit velocity field, deflated by 33%. These results show that the magnitude of locking is affected by this change, but not the pattern, indicating that the potential temporal variability may indeed be real.

References

- Argus, D., and R. Gordon (1991), No Net Rotation Model of current plate velocities incorporating plate motion model NUVEL-1, *Geophysical Research Letters*, 18(11), 2039-2042.
- Bakun, W. H., and T. V. McEvilly (1984), Recurrence models and Parkfield, California, earthquakes, *Journal of Geophysical Research*, 89(B5), 3051-3058.
- Barckhausen, U., et al. (2001), Revised tectonic boundaries in the Cocos Plate off Costa Rica: Implications for the segmentation of the convergent margin and for plate tectonics models, *Journal of Geophysical Research*, 106(B9), 19,207-219,220.
- Beck, M. E. (1998), On the mechanism of crustal block rotations in the central Andes, *Tectonophysics*, 299, 75-92.
- Biggs, J., et al. (2006), Fault identification for buried strike-slip earthquakes using InSAR: The 1994 and 2004 Al Hoceima, Morocco earthquakes, *Geophysical Journal International*, 166, 1347-1362.
- Biggs, J. (2007), InSAR observations of the Earthquake Cycle on the Denali Fault, Alaska, 214 pp, University of Oxford, Oxford.
- Bilek, S., et al. (2003), Control of seafloor roughness on earthquake rupture behavior, *Geology*, 31(5), 455-458.
- Blewitt, G. (1989), Carrier phase ambiguity resolution for the Global Positioning System applied to geodetic baselines up to 2000 km, *Journal of Geophysical Research*, 94(B8), 10187-10203.
- Blewitt, G. (1990), An automatic editing algorithm for GPS data, *Geophysical Research Letters*, 17(3), 199-202.
- Blewitt, G., and C. Kreemer (2007), Mega-network GPS solutions: Producing a consistent, global-scale, and high-resolution view of plate tectonic stability, rotation, and deformation., *EOS Trans. AGU*, 88(52), Fall Meet. Suppl., Abstract G21B-0501.
- Blewitt, G. (2008), Fixed point theorems of GPS carrier phase ambiguity resolution and their application to massive network processing: Ambizap, *Journal of Geophysical Research*, 113(B12410).
- Bro, R., and S. De Jong (1997), A fast non-negativity-constrained least squares algorithm, *Journal of Chemometrics*, 11(5), 393-401.

- Brown, J. R., et al. (2008), An autocorrelation method to detect low frequency earthquakes within tremor, *Geophysical Research Letters*, 35, L16305.
- Brown, J. R., et al. (2009), Deep Low Frequency Earthquakes in tremor localized to the plate interface in multiple subduction zones, *Geophysical Research Letters*, *submitted*.
- Brown, K., et al. (2005), Correlated transient fluid pulsing and seismic tremor in the Costa Rica subduction zone, *Earth and Planetary Science Letters*, 238, 189-203.
- Brudzinski, M., and R. M. Allen (2007), Segmentation in episodic tremor and slip all along Cascadia, *Geology*, 35(10), 907-910.
- Brudzinski, M., et al. (2007), Slow slip transients along the Oaxaca subduction segment from 1993 to 2007, *Geophys. J. Int.*, 171, 523-538.
- Cerny, V. (1985), Thermodynamical approach to the traveling salesman problem: An efficient simulation algorithm I, *Journal of Optimization Theory and Applications*, 45(1), 41-51.
- Corti, G., et al. (2005), Active strike-slip faulting in El Salvador, Central America, *Geology*, 33, 989-992.
- DeMets, C., et al. (1994), Effect of recent revisions to the geomagnetic reversal time scale on estimates of current plate motions, *Geophysical Research Letters*, 21(20), 2191-2194.
- DeMets, C. (2001), A new estimate for present-day Cocos-Caribbean plate motion: Implications for slip along the Central American volcanic arc, *Geophysical Research Letters*, 28(21), 4043-4046
- DeShon, H. R., et al. (2003), Seismic zone structure of the southern Middle America Trench, Costa Rica, *Journal of Geophysical Research*, 108(B10), 2491.
- DeShon, H. R., et al. (2006), Seismogenic zone structure beneath the Nicoya Peninsula, Costa Rica, from three-dimensional local earthquake P- and S-wave tomography, *Geophys. J. Int.*, 164, 104-124.
- Dixon, T. H. (1991), An introduction to the global positioning system and some geologic applications, *Reviews of Geophysics*, 29(2), 249-276.
- Dixon, T. H. (1993), GPS measurements of relative motion of the Cocos and Caribbean Plates and strain accumulation across the Middle America Trench, *Geophysical Research Letters*, 20(20), 2167-2170.

- Dixon, T. H., et al. (2000), Present-day motion of the Sierra Nevada Block and some tectonic implications for the Basin and Range Province, North American Cordillera, *Tectonics*, 19, (1), 1-24.
- Dmowska, R., et al. (1996), Seismicity and deformation at convergent margins due to heterogeneous coupling, *Journal of Geophysical Research*, 101(B2), 3015-3029.
- Douglas, A., et al. (2005), Slow slip on the northern Hikurangi subduction interface, New Zealand, *Geophysical Research Letters*, 32(L16305), doi:10.1029/2005GL023607.
- Dragert, H., et al. (2001), A silent slip event on the deeper Cascadia subduction interface, *Science*, 292(5521), 1525-1528.
- Dragert, H. (2007), Mediating plate convergence, *Science*, 315, 471-472.
- Fisher, D. M., et al. (1998), Effect of subducting sea-floor roughness on fore-arc kinematics, Pacific coast, Costa Rica, *Geology*, 26(5), 467-470.
- Fisher, D. M., et al. (2004), Active thrusting in the inner fore arc of an erosive convergent margin, Pacific coast, Costa Rica, *Tectonics*, 23.
- Fitch, T. J. (1972), Plate convergence, transcurrent faults and internal deformation adjacent to Southeast Asia and the Western Pacific, *Journal of Geophysical Research*, 77(23), 4432-4460.
- Franco, S. I., et al. (2005), Propagation of the 2001-2002 silent earthquake and interplate coupling in the Oaxaca subduction zone, Mexico, *Earth Planets Space*, 54, 973-985.
- Funning, G. J. (2005), Source parameters of large shallow earthquakes in the Alpine-Himalayan belt from InSAR and waveform modelling, 303 pp, University of Oxford, Oxford.
- Funning, G. J., et al. (2005), The 1998 Aiquile, Bolivia earthquake: A seismically active fault revealed with InSAR, *Earth and Planetary Science Letters*, 232(1-2), 39-49.
- Gardner, T. W., et al. (1992), Quaternary uplift astride the aseismic Cocos Ridge, Pacific coast Costa Rica, *Geologic Society of America Bulletin*, 104, 219-232.
- Gardner, T. W., et al. (2001), Holocene forearc block rotation in response to seamount subduction on, southeastern Peninsula de Nicoya, Costa Rica, *Geology*, 29(2), 151-154.

- Guzman-Speziale, M. (2001), Active seismic deformation in the grabens of northern Central America and its relationship to the relative motion of the North American-Caribbean plate boundary, *Tectonics*, 337, 39-51.
- Hey, R. (1977), Tectonic evolution of the Cocos-Nazca spreading center, *Geologic Society of America Bulletin*, 1977, 1404-1420.
- Hinz, K., et al. (1996), Tectonic structure of the convergent Pacific margin offshore Costa Rica from multichannel seismic reflection data, *Tectonics*, 15, 54-66.
- Hirose, H., et al. (1999), A slow thrust slip event following the two 1996 Hyuganada earthquakes beneath the Bungo Channel, southwest Japan, *Geophysical Research Letters*, 26, 3237-3240.
- Hirose, H., and K. Hirahara (2002), A model for complex slip behavior on a large asperity at subduction zones, *Geophysical Research Letters*, 29(22).
- Hirose, H., and K. Obara (2005), Repeating short- and long-term slow slip events with deep tremor activity around the Bungo channel region, southwest Japan, *Earth Planets and Space*, 57(10), 961-972.
- Hirose, H., and K. Obara (2006), Short-term slow slip and correlated tremor episodes in the Tokai region, central Japan, *Geophysical Research Letters*, 33(L17311).
- Husen, S., et al. (2002), Tomographic evidence for a subducted seamount beneath the Gulf of Nicoya, Costa Rica: The cause of the 1990 Mw = 7.0 Gulf of Nicoya earthquake, *Geophysical Research Letters*, 29(8), 1238.
- Hutnak, M., et al. (2007), The thermal state of 18-24 Ma upper lithosphere subducting below the Nicoya Peninsula, Northern Costa Rica margin, in *The Seismogenic Zone of Subduction Thrust Faults*, edited by T. Dixon and J. C. Moore, pp. 86-122, Columbia University Press, New York.
- Igarashi, T., et al. (2003), Repeating earthquakes and interplate aseismic slip in the northeastern Japan subduction zone, *Journal of Geophysical Research*, 108(B5), 2249, doi:2210.1029/2002JB001920,.
- Ihmle, P. F. (1996), Monte Carlo slip inversion in the frequency-domain: Application to the 1992 Nicaragua slow earthquake, *Geophysical Research Letters*, 23, 913-916.
- Iinuma, T., et al. (2004), Inter-plate coupling in the Nicoya Peninsula, Costa Rica, as deduced from a trans-peninsula GPS experiment, *Earth and Planetary Science Letters*, 223(203-212).
- Ito, Y., et al. (2007), Slow earthquakes coincident with episodic tremors and slow slip events, *Science*, 315, 503-506.

- Jarrard, R. D. (1986), Terrane motion by strike-slip faulting of forearc slivers, *Geology*, *14*(9), 780-783.
- Ji, C., et al. (2002), Source description of the 1999 Hector Mine, California, Earthquake, Part I: Wavelet domain Inversion theory and resolution analysis, *Bulletin of the Seismological Society of America*, *92*(4), 1192-1207.
- Jonsson, S., et al. (2002), Fault slip distribution of the 1999 Mw 7.1 Hector Mine, California, Earthquake, estimated from satellite radar and GPS Measurements *Bulletin of the Seismological Society of America*, *92*(4), 1377-1389.
- Kanamori, H., and M. Kikuchi (1993), The 1992 Nicaragua earthquake: A slow tsunami earthquake associated with subducted sediments, *Nature*, *361*, 714-716.
- Kaneko, S. (1966), Transcurrent displacement along the median line, south-western Japan, *N. Z. J. Geology and Geophysics*, *2*, 45-59.
- Kao, H., et al. (2005), A wide depth distribution of seismic tremors along the northern Cascadia margin, *Nature*, *436*, 841-844.
- Kato, N. (2003), A possible model for large preseismic slip on a deeper extension of a seismic rupture plane, *Earth and Planetary Science Letters*, *216*, 17-25.
- Kirkpatrick, S., et al. (1983), Optimization by simulated annealing, *Science*, *220*, 671-680.
- Klein, F. W. (2007), User's guide to HYPOINVERSE-2000, a FORTRAN program to solve for earthquake locations and magnitudes, *version 1.1(US)*, 2-171.
- Kostoglodov, V., et al. (2003), A large silent earthquake in the Guerrero seismic gap, Mexico, *Geophysical Research Letters*, *30*(15), 1807-1810.
- LaBonte, A. L., et al. (2009), Hydrologic detection and finite element modeling of a slow slip event in the Costa Rica prism toe, *Journal of Geophysical Research*, *114*(B00A02).
- LaFemina, P., et al. (2009), Fore-arc motion and Cocos Ridge collision in Central America, *Geochemistry Geophysics Geosystems*, *10*(Q05S14).
- LaFemina, P. C., et al. (2002), Bookshelf faulting in Nicaragua, *Geology*, *30*, 751-754.
- Larson, K. M., et al. (2004), Crustal deformation measurements in Guerrero, Mexico, *Journal of Geophysical Research*, *109*(B04409, doi:10.1029/2003JB002843).

- Larson, K. M., et al. (2007), The 2006 aseismic slow slip event in Guerrero, Mexico: New results from GPS, *Geophysical Research Letters*, 34, L13309.
- Lopez, A. M., et al. (2006), Is there a northern Lesser Antilles forearc block?, *Geophysical Research Letters*, 33(L07313).
- Lowry, A. R., et al. (2001), Transient fault slip in Guerrero, southern Mexico, *Geophysical Research Letters*, 28(19), 3753-3756.
- Lundgren, P., et al. (1999), Seismic cycle and plate margin deformation in Costa Rica: GPS observations from 1994 to 1997, *Journal of Geophysical Research*, 104(B12), 28915-28926.
- Mann, P., and J. Corrigan (1990), Model for Neogene deformation in Panama, *Geology*, 18, 558-562.
- Mao, A., et al. (1999), Noise in GPS coordinate time series, *Journal of Geophysical Research*, 104(B2), 2797-2816.
- Marshall, J. S., et al. (2000), Central Costa Rica deform belt: Kinematics of diffuse faulting across the western Panama block, *Tectonics*, 19(3), 468-492.
- Marshall, J. S. (2007), The geomorphology and physiographic provinces of Central America, in *Central America: Geology, Resources and Hazards*, edited by J. Brundschuh and G. E. Alvarado, p. Chapter 3, Taylor & Francis, London.
- McCaffrey, R. (1992), Oblique plate convergence, slip vectors, and forearc deformation, *Journal of Geophysical Research*, 97, 8905-8915.
- McCaffrey, R. (1996), Estimates of modern arc-parallel strain rates in forearcs, *Geology*, 24, 27-30.
- McCaffrey, R., et al. (2000), Strain partitioning during oblique plate convergence in northern Sumatra: Geodetic and seismologic constraints and numerical modeling, *Journal of Geophysical Research*, 105(B12), 28363-28376.
- McCaffrey, R., et al. (2000), Rotation and plate locking at the southern Cascadia subduction zone, *Geophysical Research Letters*, 27(19), 3117-3120.
- McCaffrey, R. (2002), *Crustal Block Rotations and Plate Coupling*, 101-122 pp.
- McCaffrey, R. (2006), DEFNODE User's manual, 2006.08.28.
- McCaffrey, R., et al. (2008), Slow slip and frictional transition at low temperatures at the Hikurangi subduction zone, *Nature geoscience*, 1, 316-320.

- McClausland, W., et al. (2005), Temporal and spatial occurrence of deep non-volcanic tremor: From Washington to northern California, *Geophysical Research Letters*, 32, L24311.
- Melbourne, T. I., et al. (2005), Extent and duration of the 2003 Cascadia slow earthquake, *Geophysical Research Letters*, 32, L04301.
- Meschede, M., et al. (1998), Extinct spreading Cocos Ridge, *Terra Nova*, 10, 211-216.
- Miller, M. M., et al. (2002), Periodic slow earthquakes from the Cascadia Subduction Zone, *Science*, 295(5564), 2423-.
- Murray, J. R., and P. Segall (2005), Spatiotemporal evolution of a transient slip event on the San Andreas fault near Parkfield California, *Journal of Geophysical Research*, 110(B9).
- Newman, A. V., et al. (2002), Along-strike variability in the seismogenic zone below Nicoya Peninsula, Costa Rica, *Geophysical Research Letters*, 29(20), 38.31-38.34.
- Nishenko, S. P. (1991), Circum-Pacific seismic potential 1989-1999, *Pure and Applied Geophysics*, 135(2), 169-259.
- Norabuena, E., et al. (2004), Geodetic and Seismic Constraints on seismogenic zone processes in Costa Rica, *Journal of Geophysical Research*, 109(doi:10.1029/2003JB002931).
- Obara, K. (2002), Nonvolcanic deep tremor associated with subduction in southwest Japan, *Science*, 296(5573), 1679-1681.
- Obara, K., et al. (2004), Episodic slow slip events accompanied by non-volcanic tremors in southwest Japan subduction zone, *Geophysical Research Letters*, 31, L23602.
- Okada, A. (1971), Active faulting if the median tectonic line (in Japanese), *Kagaku*, 41, 666-669.
- Okada, Y. (1985), Surface deformation due to shear and tensile faults in a half-space, *Bull. Seimol. Soc. Am.*, 75, 1135-1154.
- Outerbridge, K. C., et al. (2010), A Tremor and Slip Event on the Cocos-Caribbean subduction zone as measured by a GPS and seismic network on the Nicoya Peninsula, Costa Rica, *Journal of Geophysical Research*, 115, B10408, doi:10.1029/2009JB006845.

- Ozawa, S., et al. (2001), Time-dependent inversion study of the slow thrust event in the Nankai trough subduction zone, southwestern Japan, *Journal of Geophysical Research*, 106(B1), 787-802.
- Ozawa, S., et al. (2002), Detection and monitoring of ongoing aseismic slip in the Tokai Region, Central Japan, *Science*, 298(5595), 1009-1012.
- Ozawa, S., et al. (2003), Characteristic silent earthquakes in the eastern part of the Boso peninsula, Central Japan, *Geophysical Research Letters*, 30(6), 1283.
- Ozawa, S., et al. (2004), Aseismic slip and low-frequency earthquakes in the Bungo channel, southwestern Japan, *Geophysical Research Letters*, 31(L07609).
- Ozawa, S., et al. (2007), Spatiotemporal evolution of aseismic interplate slip between 1996 and 1998 and between 2002 and 2004 in Bungo channel, southwest Japan, *Journal of Geophysical Research*, 112(B05409).
- Pacheco, J. F., and L. R. Sykes (1992), Seismic moment catalog of large shallow earthquakes 1900-1989, *Bulletin of the Seismological Society of America*, 82, 1306-1349.
- Parkinson, B. W., and J. J. J. Spilker (Eds.) (1996a), *Global Positioning System: Theory and Applications*, 793 pp., American Institute of Aeronautics and Astronautics Inc, Washington DC.
- Parkinson, B. W., and J. J. J. Spilker (Eds.) (1996b), *Global Positioning System: Theory and Applications*, 643 pp., American Institute of Aeronautics and Astronautics Inc, Washington DC.
- Peacock, S. M., and K. Wang (1999), Seismic consequences of warm versus cool subduction metamorphism: Examples from Southwest and Northeast Japan, *Science*, 286, 937-939.
- Peacock, S. M., et al. (2002), Thermal structure and metamorphism of subducting oceanic crust: Insight into Cascadia intraslab earthquakes, in *The Cascadia Subduction Zone and Related Subduction Systems-- Seismic Structure, Intraslab Earthquakes and Processes, and Earthquake Hazards*, edited by S. Kirby, et al., pp. 123-126, USGS, Menlo Park.
- Peacock, S. M. (2003), Thermal structure and metamorphic evolution of subducting slabs, in *Subduction Zone Factory TEI*, edited, pp. 7-22, American Geophysical Union, Washington D.C.
- Peacock, S. M., et al. (2005), Thermal Structure of the Costa Rica - Nicaragua subduction zone, *Physics of the Earth and Planetary Interiors*, 149, 187-200.

- Peacock, S. M. (2009), Thermal and metamorphic environment of subduction zone episodic tremor and slip, *Journal of Geophysical Research*, *In Press*.
- Piatanesi, A., et al. (1996), The slip distribution of the 1992 Nicaragua earthquake from tsunami run-up data, *Geophysical Research Letters*, *23*, 37-40.
- Protti, J. M., et al. (2004), A creep event on the shallow interface of the Nicoya Peninsula, Costa Rica seismogenic zone, *EOS Trans. AGU*, *85*(87), Fall Meet. Suppl., Abstract S41D-07.
- Protti, M., et al. (1995a), Correlation between age of subducting Cocos Plate and the geometry of the Wadati-Benioff zone under Nicaragua and Costa Rica, in *Geologic and Tectonic Development of the Caribbean Plate Boundary in Southern Central America*, edited by P. Mann, pp. 309-343, Geological Society of America Special Papers.
- Protti, M., et al. (1995b), The March 25, 1990 (Mw=7.0, ML=6.8), earthquake at the entrance of the Nicoya Gulf, Costa Rica: Its prior activity, foreshocks, aftershocks, and triggered seismicity, *Journal of Geophysical Research*, *100*(B10), 20,345 - 320,358.
- Rogers, G., and H. Dragert (2003), Episodic tremor and slip on the Cascadia Subduction Zone: The chatter of silent slip, *Science*, *300*(5627), 1942-1943.
- Rongved, L., and J. T. Frasier (1958), Displacement discontinuity in the elastic half-space, *Journal of Applied Mechanics*, *25*, 125-128.
- Saffer, D. M., et al. (2000), Inferred pore pressures at the Costa Rica subduction zone: implications for dewatering processes, *Earth and Planetary Science Letters*, *177*, 193-207.
- Saffer, D. M. (2003), Pore pressure development and progressive dewatering in underthrust sediments at the Costa Rican subduction margin: Comparison with northern Barbados and Nankai, *Journal of Geophysical Research*, *108*(B5), 2261.
- Saffer, D. M. (2007), Pore Pressure within Underthrust Sediment in Subduction Zones, in *The Seismogenic Zone of Subduction Thrust Faults*, edited by T. Dixon and J. C. Moore, pp. 171-209, Columbia University Press, New York.
- Sak, P. B., et al. (2004), Effects of subducting seafloor roughness on upper plate vertical tectonism: Osa Peninsula, Costa Rica, *Tectonics*, *23*, TC1017.
- Sak, P. B., et al. (2009), Rough crust subduction, forearc kinematics, and Quaternary uplift rates, Costa Rican segment of the Middle American Trench, *Geologic Society of America Bulletin*, *121*(7-8), 992-1012.

- Savage, J. C. (1983), A dislocation model of strain accumulation and release at a subduction zone, *Journal of Geophysical Research*, *88*, 4984-4996.
- Schwartz, S. Y. (1999), Noncharacteristic behavior and complex recurrence of large subduction zone earthquake, *Journal of Geophysical Research*, *104*(B10), 23111-23125.
- Schwartz, S. Y., and J. M. Rokosky (2007), Slow slip events and seismic tremor at circum-Pacific subduction zones, *Reviews of Geophysics*, *45*, RG3004.
- Sella, G. F., et al. (2002), REVEL: A model for recent plate velocities from space geodesy, *Journal of Geophysical Research*, *107*(B4), 2081-2112.
- Shelly, D. R., et al. (2006), Low-frequency earthquakes in Shikoku, Japan, and their relationship to episodic tremor and slip, *Nature*, *442*(7099), 188-191.
- Shelly, D. R., et al. (2007a), Complex evolution of transient slip derived from precise tremor locations in western Shikoku, Japan, *Geochemistry Geophysics Geosystems*, *8*(10), Q10014.
- Shelly, D. R., et al. (2007b), Non-volcanic tremor and low-frequency earthquake swarms, *Nature*, *446*, 305-307.
- Silver, E. A., et al. (1990), Implications of the north and south Panama thrust belts for the origin of the Panama orocline, *Tectonics*, *9*, 261-281.
- Sitchler, J. C., et al. (2007), Constraints on inner forearc deformation from balanced cross sections, Fila Costena thrust belt, Costa Rica, *Tectonics*, *26*, TC6012.
- Spinelli, G. A., and D. M. Saffer (2004), Along-strike variations in underthrust sediment dewatering on the Nicoya margin Costa Rica related to the updip limit of seismicity, *Geophysical Research Letters*, *31*, L04613.
- Spinelli, G. A., et al. (2006), Hydrogeologic responses to three dimensional temperature variability, Costa Rica subduction margin, *Journal of Geophysical Research*, *111*, B04403.
- Steketee, J. A. (1958), On Volterra's dislocations in a semi-infinite elastic medium, *Canadian Journal of Physics*, *36*(2), 192-205.
- Stein, S., and M. Wyss (2003), *An Introduction to Seismology, Earthquakes, and Earth Structure*, 498 pp., Blackwell Publishing Ltd, Oxford.
- Subarya, C., et al. (2006), Plate-boundary deformation associated with the great Sumatra-Andaman earthquake, *Nature*, *440*, 46-51.

- Szeliga, W., et al. (2008), GPS constraints on 34 slow slip events within the Cascadia subduction zone, 1997-2005, *Journal of Geophysical Research*, 113(B04404).
- Thatcher, W. (1990), Order and diversity in the modes of circum-Pacific earthquake recurrence, *Journal of Geophysical Research*, 95(B3), 2609-2623.
- Trenkamp, R., et al. (2002), Wide plate margin deformation, southern Central America and northwestern South America, CASA GPS observations, *Journal of South American Earth Sciences*, 15, 157-171.
- Turner, H. L. I., et al. (2007), Kinematics of Nicaraguan forearc from GPS geodesy, *Geophysical Research Letters*, 34, L02302.
- Von Huene, R., et al. (1995), Morphotectonics of the Pacific convergent margin of Costa Rica, in *Geologic and Tectonic Development of the Caribbean Plate Boundary in Southern Central America*, edited by P. Mann, pp. 291-308, Geological Society of America Special Papers.
- Von Huene, R., et al. (2000), Quaternary convergent margin tectonics of Costa Rica, segmentation of the Cocos Plate and Central American volcanism, *Tectonics*, 19(2), 314-334.
- Walther, C. H. E. (2003), The crustal structure of the Cocos ridge off Costa Rica, *Journal of Geophysical Research*, 108(B3), 2136.
- Wdowinski, S. (2009), GPS basics, edited by K. C. Outerbridge, Miami.
- Wech, A. G., and K. C. Creager (2008), Automated detection and location of Cascadia tremor, *Geophysical Research Letters*, 35, L20302.
- Yamanaka, Y., and M. Kikuchi (2004), Asperity map along the subduction zone in northeastern Japan inferred from regional seismic data, *Journal of Geophysical Research*, 109(B07307).
- Zumberge, J. F., et al. (1997), Precise point positioning from the efficient and robust analysis of GPS data from large networks, *Journal of Geophysical Research*, 102(B3), 5005-5017.
- Zweck, C., et al. (2002), Three-dimensional elastic dislocation modeling of the postseismic response to the 1964 Alaska earthquake, *Journal of Geophysical Research*, 107(B4).